Analytical Steps Towards the Observation of High-Spin Black Holes

Citation

Shi, Yichen. 2019. Analytical Steps Towards the Observation of High-Spin Black Holes. Doctoral dissertation, Harvard University, Graduate School of Arts & Sciences.

Analytical Steps Towards the Observation of High-Spin Black Holes

A DISSERTATION PRESENTED
BY
YICHEN SHI
TO
THE DEPARTMENT OF PHYSICS

IN PARTIAL FULFILLMENT OF THE REQUIREMENTS
FOR THE DEGREE OF
DOCTOR OF PHILOSOPHY
IN THE SUBJECT OF
PHYSICS

HARVARD UNIVERSITY
CAMBRIDGE, MASSACHUSETTS
FEBRUARY 2019

Dissertation advisor: Professor Andrew Strominger Yichen Shi

Analytical Steps Towards the Observation of High-Spin Black Holes

ABSTRACT

Ongoing astronomical efforts extract physical properties of a black hole from electromagnetic emissions in its vicinity. In this dissertation, we analytically study such emissions from the near-horizon region of high-spin black holes. Given the complexity of the Kerr metric, null geodesics in the spacetime of a rotating black hole are generally studied only numerically. Subsequent modelling involves extensive numerical work. In the case of a high-spin black hole, however, a simplification occurs when we zoom into its near-horizon region. This so-called Near-Horizon Extreme Kerr geometry has an $\mathsf{SL}(2,\mathbb{R}) \times \mathsf{U}(1)$ isometry. In particular, the time translation symmetry is enlarged to an $\mathsf{SL}(2,\mathbb{R})$ global conformal symmetry, which includes dilations and special-conformal transformations. Our analytical methods are based upon these enhanced symmetries. We first solve for the near-superradiant geodesics that extend from the near-horizon region to a distant observatory, expressing our results in terms of elementary functions. Next we compute the broadening of electromagnetic line emissions from the innermost part of an accretion disk. We obtain an analytic formula for the observed flux, which is independent of the disk model and therefore universal. Finally, we investigate the polarized near-horizon emissions and find patterns of whorls aligned with the black hole's spin.

Contents

致我的爸爸妈妈

Citations to Previously Published Work

- The following authors contributed to Chapter 2: Achilleas P. Porfyriadis and Andrew Strominger. The text has appeared in the following paper:

  [1] Achilleas P. Porfyriadis, Yichen Shi, and Andrew Strominger. "Photon Emission Near Extreme Kerr Black Holes." *Phys. Rev.*, D95(6):064009, 2017. [arXiv:1607.06028 [gr-qc]].

  I also acknowledge useful conversations with Samuel Gralla and Alexandru Lupsasca. Further, this research forms the basis for Chapter 0: A Story.

- The following authors contributed to Chapter 3: Alexandru Lupsasca and Achilleas P. Porfyriadis. The text has appeared in the following paper:

  [2] Alexandru Lupsasca, Achilleas P. Porfyriadis, and Yichen Shi. "Critical Emission from a High-Spin Black Hole." *Phys. Rev.*, D97(6):064017, 2018. [arXiv:1712.10182 [gr-qc]].

  I also acknowledge helpful comments from Andrew Strominger, data provided by Laura Brenneman, Thomas Dauser, and Michael Parker, as well as useful conversations with Geoffrey Compère, Sheperd Doeleman, Samuel Gralla, Michael D. Johnson, and Roberto Oliveri.

- The following authors contributed to Chapter 4: Delilah Gates, Daniel Kapec, Alexandru Lupsasca and Andrew Strominger. The text has appeared in the following paper:

  [3] Delilah Gates, Daniel Kapec, Alexandru Lupsasca, Yichen Shi, and Andrew Strominger. "Polarization Whorls from M87 at the Event Horizon Telescope." 2018. [arXiv:1809.09092 [hep-th]].

  I also acknowledge useful conversations with Geoffrey Compère, Sheperd Doeleman, Samuel Gralla, Michael D. Johnson, and Achilleas Porfyriadis.

Acknowledgments

My last four and a half years at Harvard have been the most intellectually stimulating years of my life. I must first thank my advisor, Andy Strominger, an inspirational physicist. Without him, nothing would have been possible.

I thank DG for being by my side, grounding me when I couldn't myself. His comments have been invaluable in the preparation of this dissertation. A big thank you to Qin Chen for our lifelong friendship, for always believing in me. I'm indebted to Carlo Bradac, Gavin Brennen, and Peter Bouwknegt, who had inspired and guided me through my undergraduate studies and beyond.

At Harvard, I deeply appreciate the support of Jacob Barandes. I'm also thankful to Lisa Cacciabaudo, Temple He, Julie Heller, Anne Herbert, Monica Kang, Lisa Lee, Junaid Nabi, Anjalika Nande, Mark Pantano, Monica Pate, Ana Raclariu, Elana Urbach, and Ioana Zelko. My sincere appreciation goes to my collaborators: Delilah Gates, Daniel Kapec, Alexandru Lupsasca, and Achilleas Porfyriadis.

I'm grateful to my Boston writing communities. In particular, useful feedback from my following writer friends helped me improve Chapter 0: Shannon Browne, Kenneth P. J. Dyer, Juliet Faithfull, Phillip Freeman, Eve LaPlante, David Schiffer, and Gregory Stanley.

Most importantly, I owe my parents for everything. I love you! ♡

0

A Story (for non-physicists)

Physicists, please proceed to Chapter 1.

0.1 PROLOGUE

When you look at me, what you see is not a woman with East Asian features. No, I have no problem with my gender or ethnicity. And no, I'm not out of my mind.

It is light that you see.

Beautiful fall day in New England. You stroll across Harvard Yard, listening to the rustling trees, glad your advisor is on her flight to Europe. You look up and see the bright sun. You look down and see a blanket of fallen leaves. A pretty clear connection. But you haven't paid attention to what you're actually seeing—light, the *photons*[*] exhausted from traveling 93 million miles to show you beautiful colors. Maybe it's time you did. But if you really want to marvel, stop and consider the journey of light from other stars. The distances are so large that it's easier to measure them using the *light-year*: how far light travels in a year. Nearly six trillion miles, in other words.

Starlight is so dim that it doesn't reveal dust bunnies in your room the way sunlight does, but physicists describe them in the same way. Feel free to stare at the sun or the stars. (Nah, physicists don't care about eye damage.) In all such cases, there is

- a point of emission, e.g., the Sun, the stars, or a lightbulb,
- a point of observation, e.g., you, me, or a telescope, and
- the voyagers: the photons.

If the photons don't make the trip from the point of emission to the point of observation, you don't see whatever you want to see. The photon is the hero of our tale.

And the heroine? The black hole.

What I have for you is the tale of a journey. The hero's treacherous journey where he travels for light-years to present the heroine to us, humans. Sit back, relax, but don't shut your eyes. We have a

---

[*] Photons are particles of light. When I say "light," I mean not only visible light, but the entire electromagnetic spectrum, including X-rays (high-energy photons) and radio waves (low-energy photons). X-ray telescopes see light in the X-ray part of the spectrum; radio telescopes see light in the radio-wave part.

lot of “seeing” to do.

Consider the stars residing in the vicinity of black holes. Stars, by definition, emit photons. So do we see their starlight the way we see sunlight? First take a step back. In the Milky Way alone, there are hundreds of billions of stars, many of them interesting. Why do we place emphasis on the stars near black holes? It’s not these stars themselves that are special, but their behavior. A black hole is black; its gravity is so strong that not even light escapes. We have no chance to see a black hole itself. Through certain behavior of stars (as well as other matter), however, we can infer the existence of a nearby massive object—the black hole—thus seeing it indirectly.

So, I say, how do photons from these stars get here?

They just come, you say. Isn’t it straightforward?

Nope. Not so straight, and not always forward. Answering how photons get here from the region near a black hole is the subject of my Ph.D.[1–3].

0.2 Curved spacetime: finding our heroine

In 1915, Albert Einstein formulated the general theory of relativity[4]. Through equations of great complexity, later known as the *Einstein field equations*, his theory provided a framework for describing the geometry of space and time. In general relativity, space and time are on equal footing—gravity curves space and slows time. So I’ll use the term *spacetime* to include both three-dimensional space and one-dimensional time.

Einstein’s idea that spacetime is curved by matter and radiation has revolutionized humanity’s un-

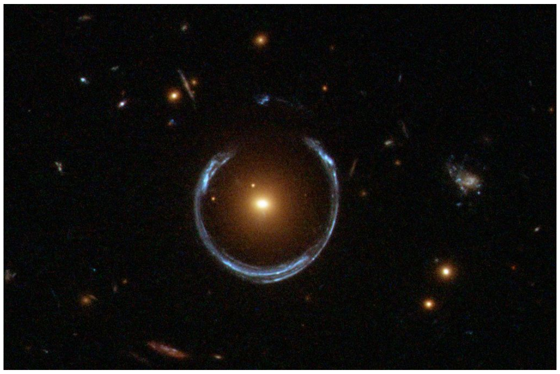

Figure 1: The gravitational lensing effect. The blue galaxy is hiding behind the red galaxy---we aren't ``supposed'' to see it. But the red galaxy curves spacetime. When photons from the blue galaxy pass the red galaxy, their paths bend, and they manage to reach us. The blue galaxy ends up appearing like a ring. Image taken by the Hubble Space Telescope. Image credit: ESA/NASA.

derstanding of the universe. It has survived multiple tests, from the observation of the gravitational lensing effect (see Figure 1)[5] to the recent detection of gravitational waves[6].

You curve spacetime. *I* curve spacetime. If we gain some weight, we curve spacetime a little more. The Sun curves spacetime. And a black hole, as massive as it is, curves spacetime very much. This is why photons emitted from the region near a black hole don't travel to us in straight lines. "Straight" is, in fact, a misleading word. If I live on Earth and you live near a black hole (sorry!), then my "straight" isn't quite your "straight."

Before we can discuss this in detail, we must properly invite our heroine to the stage and learn about her past. How did we find her? How did the idea of a black hole come about?

Einstein came up with an elegant theory; any solution of the Einstein field equations would be a spacetime. Yes, *a* spacetime. You may think that spacetime is an absolute concept, that we all live in the same spacetime. Indeed, your notion of spacetime—our universe with every galaxy, black hole, star, and human taken into account—is a solution of the Einstein field equations. But I doubt the mental power of a trillion Einsteins would be enough to write down that solution.

A solution that can be easily written down is the trivial solution of flat spacetime, a spacetime with nothing in it. In general, however, writing down solutions of the Einstein field equations is difficult. Extremely so. The good news is that black hole spacetimes[†] are mathematical solutions we can write down.

In December, 1915, German physicist Karl Schwarzschild wrote down an interesting solution of the Einstein field equations[7]. It is the spacetime of a *non-spinning*, (electrically) *uncharged* spherical object. The term "black hole" was never mentioned in his original paper, but Schwarzschild's work launched our modern exploration of black holes. His solution is now known as the Schwarzschild spacetime, and that non-spinning, uncharged object, the Schwarzschild black hole.

A few years later, Hans Reissner, Hermann Weyl, Gunnar Nordström, and George Jeffery wrote down a solution for the case of a *non-spinning*, *charged* spherical object[8–11]. We now refer to it as the Reissner-Nordström spacetime. To the real world, however, the Reissner-Nordström black hole is irrelevant: Positive and negative charges cancel each other. Any positively charged black hole would quickly attract negatively charged particles in the universe and become uncharged.

Is any black hole relevant to our universe? After the wave of theoretical work in mid to late 1910s, things quietened. Decades went by, and not much happened. Perhaps there was a lack of urgency because black holes remained mathematical constructs. Einstein himself thought that black holes did

---

[†] A black hole spacetime is the spacetime of one black hole. We can use it as a good approximation of the real world if we want to study black holes, one by one.

Figure 2: Left: See how the tarpaulin dips? Think of the boy or the tiger as the black hole and the tarpaulin as the spacetime. Copyright owned by Ang Lee, Gil Netter and David Womark. 2012. *Life of Pi*. Right: See how the batter twists? Think of the beater as the black hole and the batter as the spacetime. Courtesy of *struongdesn.com*.

not exist, concluding in his 1939 paper that "matter cannot be concentrated arbitrarily"[12].

But then in 1963, something big happened. New Zealander mathematician Roy Kerr wrote down a more general solution of the Einstein field equations[13]. Now known as the Kerr solution, it is the spacetime of a *spinning*, *uncharged* spherical object. Charged black holes become uncharged, but spinning ones keep spinning. We know that the Earth, the Moon, the Sun, the Milky Way—they are all spinning. What doesn't? If black holes existed, then chances are, they'd be spinning. The mass of a black hole bends spacetime the way the tiger bends Pi's tarpaulin; its spin twists spacetime like a beater in the batter (see Figure 2). The Kerr spacetime is one of the most important discoveries of the twentieth century.

To complete the picture, I mention also the solution of Ezra Newman et al. two years later. It is the spacetime of a *spinning*, *charged* spherical object[14].

	Non-spinning	Spinning
Uncharged	Schwarzschild	Kerr
Charged	Reissner-Nordström	Kerr-Newman

Table 1: Black hole solutions of the Einstein field equations.

Wait, what did I mean by "to complete the picture"? Are we done with black hole spacetimes that solve the Einstein field equations[‡]? Yes. Our heroine has only three features. Theoretically, every black hole has a mass, some of them spin, and some are charged. That's all. The *no-hair theorem*, first shown by Werner Israel in 1967, states[20]:

> A black hole solution of the Einstein field equations can be completely characterized by its mass, charge, and spin.

As discussed earlier, charged black holes quickly become uncharged. So for all practical purposes, mass and spin are the only properties for us to describe a black hole with. Hence, we focus on the Kerr solution from this point onward, leaving charge out of the picture. I'll be using the words "Kerr" and "spinning" interchangeably.

So our heroine is a dancer. How fast can she spin? Is there a limit on a black hole's spin? Yes. To explain this, I first need to introduce the terms *singularity* and *event horizon*. A singularity is a region in spacetime where the amount of gravity is infinite and the Laws of Physics break down. You don't want to go there unless you want to be stretched into spaghetti (and spaghetti doesn't convey the "gravity" of the situation). Next, our heroine has a veil—the event horizon. It is the surface around

---

[‡] There are also non-trivial non-black hole solutions of the Einstein field equations. A notable one is the FLRW spacetime, developed by Alexander Friedmann, Georges Lemaître, Howard Robertson, and Arthur Walker in the 1920s and 1930s[15–19]. It describes a universe that's uniform, looks the same from all directions, and is expanding or contracting.

a black hole beyond which not even light can escape. When light doesn't escape, information doesn't either. The speed of light sets a fundamental limit on our universe. Now, any black hole's singularity always lies behind its event horizon. One that doesn't is referred to as a *naked singularity*, and naked singularities are believed to be non-existent. This is known as the *cosmic censorship conjecture*.

How does this relate to the spin of a black hole? It turns out that when the spin exceeds a certain value (depending on the mass of that black hole), the event horizon disappears—the singularity becomes naked. And that's not allowed. Conversely, as long as the singularity stays behind the event horizon, the spin must be limited by a maximum value.

Our heroine cannot spin arbitrarily fast.

0.3 Geodesics: understanding our hero's journey

We now have a description of the spacetime of our heroine—the spinning black hole—and we know there is a limit on how fast she can spin. So how does our hero—the photon—travel from her all the way to us, humans?

We need *geodesics*.

In daily life, a geodesic is the shortest path between two points; it is the path a person (who hates detours) or a plane takes. Between two opposite corners of your square dining table, it's the straight line connecting them. Between your wrist and elbow, it runs along the length of your forearm. Between two points on a longitude, it's the corresponding segment on that longitude (unless you are capable of drilling through Earth). And between two points on a latitude, it's— Wait.

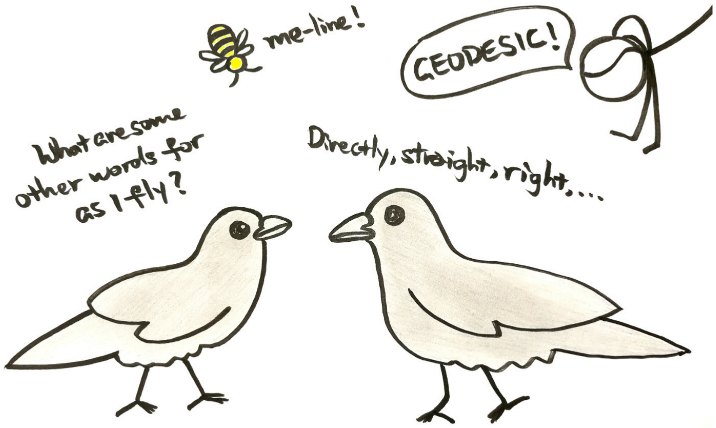

Figure 3: As the crow flies = following a geodesic on Earth.

Only segments on the equator can be geodesics, not those on other latitudes. Beijing is at 39.9^{o}N and NYC is at 40.7^{o}N, but no pilot would follow the $\sim$ 40^{o}N latitude—it is not the shortest path between the two cities. Chances are, the plane would pass over the Arctic circle. If you don't believe me, then get a globe and a string. Keeping the string tight, pin its two ends on the globe, one end on NYC, the other on Beijing. You'd see that your string wouldn't follow the $\sim$ 40^{o}N latitude (see Figure 4). Similarly, if you travel between Sydney and Cape Town, you might just pass by the Antarctic circle.

The notion of geodesics is straightforward in flat space (table, forearm) and easy to visualize on a sphere like the Earth. What about near a black hole[§]? We've established that spacetime around a black hole is bent and twisted. There, the idea of the shortest path—the most natural path any particles would take when gravity is the only force in action—isn't nearly as simple as what we experience in

---

[§] Whenever I say "near a black hole," what I mean is "near the event horizon of a black hole."

Figure 4: The strings' endpoints are fixed at Beijing (39.9^{o}N) and NYC (40.7^{o}N). The red string represents the geodesic between them; the blue string follows the $\sim\ 40^{o}$N latitude. The equator is the only latitude whose segments can be geodesics.

daily life. For particles to travel from a warped region of spacetime to us is complicated. Our hero—the photon—isn't an exception. How do we understand his treacherous journey?

Such geodesics are unimaginable. You cannot draw them the way you might draw a line on your square dining table or your globe (see Figure 5).

You need to solve equations.

In general, the geodesics that particles follow are solutions of a given set of geodesic equations. Where do the geodesic equations come from? If photons travel in the spacetime of a spinning black hole, then we can readily obtain their geodesic equations from the Kerr solution[21]. This step is doable. The next step is to solve these geodesic equations to get the geodesics. Given the complexity of the Kerr spacetime, this step had been impossible.

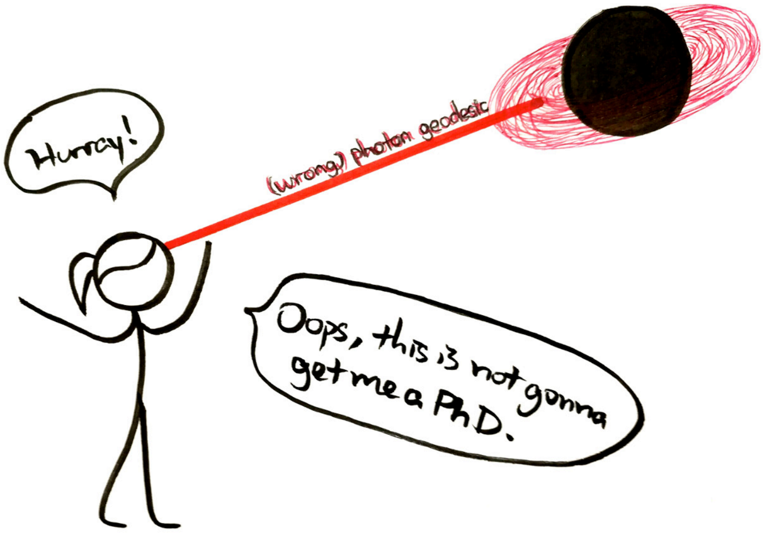

Figure 5: A *wrong* cartoon of our hero's journey from our heroine to us (see Figure 7 for a correct one). The ``straight line'' is much too naïve.

Until 2016. In our paper[1], Achilleas Porfyriadis, Andrew Strominger, and I computed these geodesics for the special case of photons emitted from the region near a fast-spinning black hole. For the first time, the journey photons take from such a black hole to a distant observer was written down analytically, in terms of elementary functions. I'll explain in Section 0.5 how we did it. But why should you care? In particular:

1. Do fast-spinning black holes even exist?
2. If so, are regions near them interesting?
3. Are analytical expressions really useful?

I'll answer these questions one by one.

0.4 Black holes are black: observing our heroine

We learned in Section 0.2 where our heroine comes from—theoretically. How about in reality? How does a black hole form? Right now, we have observational evidence for three types of black holes classified according to mass: stellar-mass black holes, intermediate-mass black holes, and supermassive black holes.

A stellar-mass black hole forms from the death of a star. When a star runs out of fuel, it collapses inwards due to its own gravity. If its mass is high enough, it turns into a black hole. Otherwise it may become a white dwarf (the fate of the Sun) or a neutron star (heavier than a white dwarf and lighter than a black hole). Stellar-mass black holes have masses typically ranging from five to thirty times the mass of the Sun, and there are millions of them in every galaxy[22].

There are several postulates on how an intermediate-mass black hole forms: the merging of stellar mass black holes, neutron stars, or white dwarfs; the collision of massive stars; the collapse of a dense region in the early universe—the case of primordial black holes[23].

The formation of a supermassive black hole is an open research topic. They grow by merging with other black holes and gravitationally accreting matter[24]. Such black holes are found in the center of galaxies[25]. Sagittarius A* (in the direction of the constellation Sagittarius) is the supermassive black hole residing in the center of the Milky Way[26]. These black holes have masses typically ranging from one hundred thousand to ten billion times the mass of the Sun.

How do we know so much about our heroine? After all, we are unable to access information from behind her veil—the event horizon. We, diligent paparazzi, learn about a black hole through the be-

	Mass (in solar masses)	Example of a black hole
Stellar-mass	< 100	Cygnus X-1 [27,28]
Intermediate-mass	$100 - 100,000$	Hyper-Luminous X-ray source 1 [29]
Supermassive	$> 100,000$	Sagittarius A* [26]

Table 2: Types of black holes classified by mass (1 solar mass = the mass of the Sun).

havior of its neighboring stars and other matter—which emit light. Our hero brings her to us. In fact, matter accreting around a black hole can form a bright disk[30]. The photons emitted by such stars and other matter travel to us, allowing us to see not only them, but also the black hole itself indirectly.

Wait, wouldn't everything around the black hole be "sucked in"? Return to the solar system for a minute. If the Sun is replaced by a black hole of the same mass and spin, what would happen to the Earth? Nothing. The Earth will continue to orbit that black hole the way it orbited the Sun. Any two objects with equal mass and spin have the same impact on the geometry of spacetime. General relativity doesn't care about other properties. Hence, there can be stars and other matter orbiting a black hole, as long as they are outside its event horizon.

So how does a neighboring star help us measure the mass of a black hole? A common strategy is to determine the star's orbit: the size of the orbit and how long it takes for the star to go around the black hole. The Laws of Gravitation would then allow us to compute the black hole's mass. That is, if we are able to make accurate observations of that orbiting star. This is doable and done for stellar-mass black holes in the Milky Way, and we refer to our heroine's friend—that neighboring star—as the *companion star*[22].

The case of a supermassive black hole is more complicated. Its size is incomparable to that of any individual star—it takes forever to sample a sufficiently large part of the star's orbit around the enormous black hole. To understand its entire orbit is thus difficult. The mass of Sagittarius A*, the supermassive black hole in the center of Milky Way, has been determined from tracing the orbits of individual stars around it[31]. This was made possible through not only twenty-five years of monitoring and data collection, but also the proximity of Sagittarius A* to the Earth. The task is much tougher for "out-of-galaxy" supermassive black holes.

What about spin? Measuring the spin of a black hole is more challenging because the twist of spacetime caused by spin manifests itself in only the region near the black hole. For a black hole with a disk of matter, the effect is evident in the innermost part of that disk—the part that's closest to the event horizon. Astronomical processes in that region involve a lot of energy; the disk of a black hole is nothing like the calm and cool rings of Saturn.

One method to determine a black hole's spin is by examining light emitted by a particular type of atom in its disk. Iron atoms are abundant, and their emissions are the easiest to observe[32]. Say there are iron atoms sitting on your dining table, and they emit a bunch of photons. What do you measure the energy of those photons to be? It should be about 6,400 electron-volts[¶]. What if, instead of your table, the iron atoms are in the disk around a black hole? In this case, rather than measuring one value for that energy, you'll get a range of values for the many emitted photons. This is a result of gravitational effects. In particular, the twist of spacetime due to the black hole's spin widen the range of values. Hence, by examining the disk around a black hole, focusing on one type of atom, and measuring the observed energies of its emitted photons, you can determine its spin.

[¶] An electron-volt is a tiny unit of energy. 6,400 electron-volts is about 0.00000000000000024 calories.

All of this relies on both our software (theoretical understanding) and our hardware (telescopes). How are humans doing with the observational side of things?

In the 1940s, when radio astronomy was advancing and X-ray astronomy wasn't quite there yet, the galaxy Cygnus A stood out as a bright radio source[33]. But it was not recognized until decades later that the supermassive black hole at its center was the cause of the source[34]. The discovery of neutron stars in the 1960s confirmed the physical relevance of compact astronomical objects[35]. And in the early 1970s, X-ray astronomy provided us with the first indirect observation of a black hole: Cygnus X-1[27,28]. Since the Earth's atmosphere blocks X-rays, it was discovered using a rocket that carried X-ray instruments.

The discovery of Cygnus X-1 led to a friendly wager between British physicist Stephen Hawking and American physicist Kip Thorne (the 2017 Physics Nobel Prize winner—the physicist behind *Interstellar*). Hawking, who had bet that the source was not a black hole, conceded his defeat two and a half decades later.

Today, we have an unprecedented amount of observational evidence for black holes. Below are some notable telescopes.

- The Hubble Space Telescope (launched in 1990), which detects light in the near ultraviolet, visible, and near infrared parts of the spectrum. It provided a significant amount of evidence that galaxies center around supermassive black holes[36,37].
- The Chandra X-ray Observatory (launched in 1999), which detects light in the X-ray part of the spectrum. It was the first to see X-ray emissions from Sagittarius A*[38].
- The Event Horizon Telescope (first data capture in 2006), which detects light in the radio part of the spectrum. It aims to resolve the event horizons around Sagittarius A* and the black hole centering the galaxy Messier 87[39].
- XMM-Newton (launched in 1999), Suzaku (launched in 2005), and NuSTAR (launched in 2012), which all detect light in the X-ray part of the spectrum (see Figure 6). These three tele-

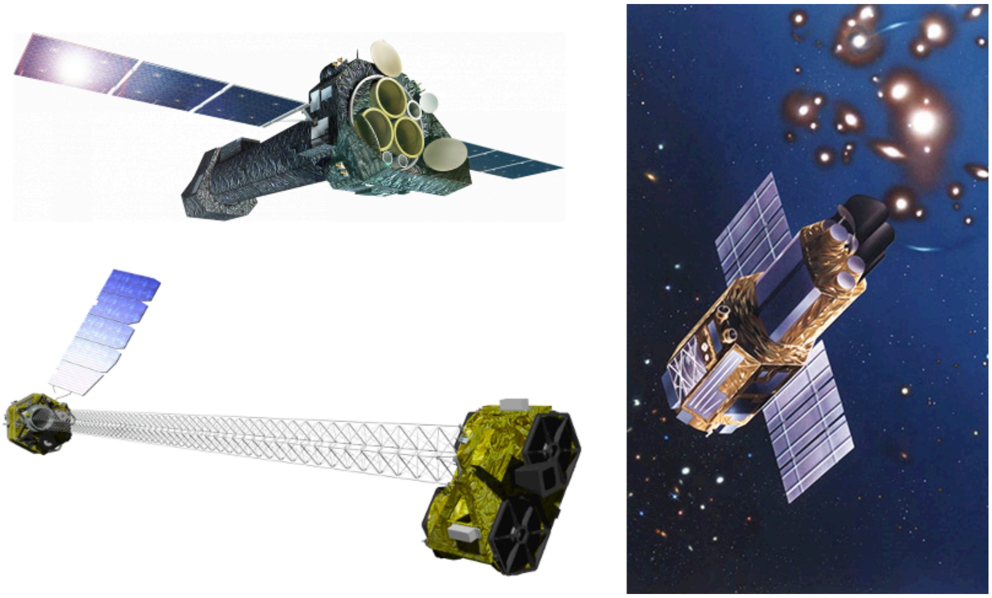

Figure 6: Artists' concepts of the X-ray telescopes XMM-Newton (top left), NuSTAR (bottom left), and Suzaku (right) in orbit. Image credit: D. Ducros/ESA, NASA/JPL-Caltech, and ISAS/JAXA, respectively.

> scopes, by looking at high-energy photons emitted from the regions near black holes, provided an enormous amount of data for spinning black holes (see Table 3). In fact, they gave us evidence that our heroine is generally good at spinning.

In Section 0.2, we discussed the limit on a black hole's spin, which depends on its mass. As supported by data, a large proportion of the black holes in our universe are likely to be spinning near the maximum rate.

To answer Question 1:

> Yes, fast-spinning black holes are likely to be abundant.

Black hole	Spin rate (max.= 1)	Black hole	Spin rate (max.= 1)
MCG-6-30-15	≥ 0.98	SWIFT J0501.9-3239	≥ 0.96
Fairall 9	~ 0.52	Ton S180	~ 0.91
SWIFT J2127.4+5654	~ 0.6	RBS 1124	≥ 0.98
1 H0707-495	≥ 0.98	Mrk 359	~ 0.66
Mrk 79	~ 0.70	Mrk 841	≥ 0.52
Mrk 335	~ 0.70	IRAS 13224-3809	≥ 0.995
NGC 3783	≥ 0.98	Mrk 1018	~ 0.58
Ark 120	~ 0.94	IRAS 00521-7054	≥ 0.84
3C 120	≥ 0.95	NGC 4051	≥ 0.99
1 H0419-577	≥ 0.88	NGC 1365	~ 0.97
Ark 564	~ 0.96	Mrk 110	≥ 0.99

Table 3: A list of spinning black holes that we have observational evidence for. Taken from Laura Brenneman's review paper[40], with data from the X-ray telescopes Suzaku, XMM-Newton, and NuSTAR. Notice the large proportion of fast-spinning black holes.

0.5 Symmetries: solving for our hero's journey

You are assigned your Calculus homework today, but you can't be bothered to look at it yet. You think you are smart. You think you can get it done if you do it on the due date. Why not wait? You have arthritis. You want to exercise to stay healthy, so you hit the pool. Water exercises are gentle on your joints, and compared to exercising on the ground, you can burn the same amount of calories. Why not go for the pool?

These examples remotely capture what physicists mean by *symmetries*. You get your homework done whether you do it today or on the due date—today is "symmetrical" to the due date. (If you don't finish it though, you'll have more trouble than no symmetry.) You get your workout done whether you do it on the ground or in a pool—the ground is "symmetrical" to the pool. Here are some more examples: The speed of light remains the same to you whether you are on a bullet train or taking a walk with your pet turtle. The Laws of Physics remain unchanged regardless of *where* or *when* you do your experiments.

Isn't it convenient that general relativity holds today and tomorrow, in your house and near a black hole? Today is "symmetrical" to tomorrow; your house is "symmetrical" to the region near a black hole (yes, I mean it). This is why physicists love symmetries.

In 1915, the same year Einstein formulated general relativity, German mathematician Emmy Noether showed that every symmetry corresponds to a conserved quantity—a quantity that remains the same no matter how other things change[41]. For example, a temporal symmetry—same regardless of *when*—corresponds to the conservation of energy; a spatial symmetry—same regardless of *where*—corresponds to the conservation of momentum.

What symmetries are present in the Kerr spacetime? The Earth is nothing like a black hole, but it *is* a spinning, uncharged spherical object. So return to the Earth for a minute—well, not quite—chill in a satellite. Pretend that there are no continents on Earth (only uniformly blue ocean) and forget the clouds. From the satellite, if you watch the Earth for ten minutes, could you do a before-versus-after comparison of the planet? No. If the side of the Earth that you faced has spun away so you are facing a different side now, could you tell any difference? No. The "Earth without continents or clouds" has temporal symmetry and rotational symmetry, corresponding to the conservation of energy and angular momentum, respectively. The same goes for a spinning black hole. In the Kerr spacetime, there are two more conserved quantities we have at hand. One wasn't derived through physical considerations[42] and the other depends on the mass of the particle traveling in the spacetime.

If it is our hero—the photon—then this quantity is zero because the photon weighs nothing.

In general, symmetries and conserved quantities simplify equations. Intuitively, same is easier to understand than different; a non-change is easier to understand than a change.

In Section 0.3, we learned that the Kerr solution of the Einstein field equations allows us to write down geodesic equations for any particles traveling in the Kerr spacetime. The solutions to the geodesic equations, in turn, would give us geodesics—the answers to *how* the particles travel. Despite the four conserved quantities, however, the Kerr geodesic equations are difficult to solve.

Interestingly, in the region very close to our heroine, the symmetries are enhanced. In 1999, American physicists James Bardeen and Gary Horowitz zoomed in on the region near a fast-spinning black hole and examined it in detail[43]. Treating that region as its own spacetime, they discovered two symmetries, which include a dilation symmetry—same regardless of how far you go "down the road" to the black hole's event horizon. In other words, any point on that road is "symmetrical" to any other point.

The enhanced symmetries greatly simplify the geodesic equations in that region. Certain terms in the unsolvable geodesic equations become negligible. After they drop out, the equations become much nicer-looking—and analytically solvable.

Fundamentally, symmetries inform us of the underlying order and structure of nature. This is the reason behind their use in solving equations. Isn't it elegant that near fast-spinning black holes, symmetries are enhanced?

To answer Question 2:

> Yes, regions near fast-spinning black holes are extremely interesting.

We now know how photons travel in the vicinity of a fast-spinning black hole, but that's only one side of the story. How do they travel to *us*, humans? Once they leave that region, the symmetries are no longer enhanced.

Physicists like spherical cows[‖]—we like to approximate. Compared with the warped spacetime around a fast-spinning black hole, the world we and our telescopes live in can be approximated as flat. In flat spacetime, there exist ten symmetries. If you take the Kerr geodesic equations and set the distance from the black hole to be large, again terms become negligible and can be dropped out. These are not the same terms as in the case near the black hole. Nevertheless, the geodesic equations can now be analytically solved.

So, we are equipped with solutions to the geodesic equations—geodesics—in both the region near a fast-spinning black hole and the region near us (far from the black hole). How do they connect? There is a mathematical method, called the *matched asymptotic expansions*, which allows us to bridge our geodesics. This is how my collaborators and I wrote down the geodesics describing the journeys photons take from fast-spinning black holes to a distant observer, expressed in terms of elementary functions[1] (see Figure 7).

But wait a minute. As soon as the Kerr geodesic equations were written down in the 1960s, numerical solutions of the geodesics were readily available. Why did we go through so much trouble to find these analytical solutions? What's the difference between numerical and analytical solutions anyway?

Go back to your square dining table and roll a tennis ball from one of its corners to the opposite.

[‖] A dairy farmer seeks advice from a physicist regarding increasing milk production. The physicists goes home, thinks hard on the problem, then calls the farmer. "I have a solution," he says. "Let's assume the cows were spherical and lived in a vacuum . . ."

Figure 7: A cartoon of our hero's treacherous journey where he travels for light-years to present our heroine (who *really* warps spacetime) to us, humans.

Having an analytical solution of the ball's geodesic means you know exactly where it is at any point on its journey. You can draw the journey—a continuous line—without lifting your marker off the table.

A numerical solution, on the other hand, corresponds to a bunch of dots instead of a continuous line. It has limitation. Is there a number between 0.55 and 0.56? Of course. For example, 0.551, 0.553647. There is an infinite number of numbers between any two numbers. Doing numerical computations to an infinite accuracy would take an infinite amount of time. It's unfeasible. But isn't knowing where the ball is 0.55 seconds and 0.56 seconds into its journey on your table good enough? Can't you guess where it is in between? Not necessarily. Without an analytical equation to guide you, between 0.55 seconds and 0.56 seconds, your tennis ball could jump up and crack your chandelier and come back and journey on without you realizing. You'd have no idea because all you know is how it behaves at two discrete points: 0.55 seconds and 0.56 seconds.

Hence, analytical solutions are superior—by far. Most of the time, only when they are unavailable do we rely on numerics. It is only through analytical expressions that we gain the deepest, fullest understanding.

To answer Question 3:

> Yes, analytical expressions are extremely useful.

Photons travel from fast-spinning black holes to our telescopes. Our analytical solutions for their geodesics opened a door to tackling various problems and led to further computations in the recent two years. For example: the observed image of a light-emitting particle orbiting a black hole[44]; the observed energies of photons emitted by iron atoms in the disk around a black hole[2]. In the long run, we hope for our analytical solutions to complement numerical methods in astronomy.

0.6 Epilogue

In Einstein's 1936 paper on the gravitational lensing effect, he wrote[45]:

> "Of course, there is no hope of observing this phenomenon directly."

But we did, forty-three years later[5]. Never in Einstein's wildest dreams would he have imagined the amount of observational evidence for black holes that we have today. Neither did he have nearly as much theoretical understanding of our universe as physicists do now.

We are tiny beings on the planet called Earth. Earth is one of the many celestial bodies orbiting the Sun. The solar system is one of the hundreds of billions of star systems in the Milky Way. Then there are galaxy groups, galaxy clusters, and superclusters containing many galaxies like the Milky Way. For the insignificant *us* to hear stories of our distant, enormous, and invisible heroine—the black hole—isn't it awe-inspiring? We must thank our messenger, our hero—the photon.

Refreshing fall night in New England. You look up and see the stars. And you find yourself thinking about what you are seeing, how you are seeing them. You march across Harvard Yard, listening to the crisp sound of your shoes crunching dead leaves, and you tell me: The photons are tired. No, not just tired. They've completed their mission, traveled heroically from light-years away just to hit our eyes, to cease to exist. Did they "die"? Well, they carried energy, and energy is conserved. They did not come here in vain—they've become a part of us, their energy transferred to us. Across spacetime.

It's humbling, isn't it?

On our long road to reality, we laugh, we cry, we work with patience and photons and spherical cows. And we see something breathtaking, even in the black night. Light.

1

Introduction

THIS IS AN ERA OF RAPID PROGRESS in observational black hole astrophysics. With the detection of gravitational waves from a binary black hole merger, LIGO has established gravitational-wave observation as a new tool to study these “unseeable” objects[6,46–49]. The majority of present methods, however, still rely on electromagnetic emissions in the vicinity of black holes.

In the last two decades, among others, the X-ray telescopes XMM-Newton, Suzaku, and NuSTAR have provided an enormous amount of data on black holes, especially supermassive ones in active galactic nuclei. In particular, their data have enabled astrophysicists to determine the spins of the observed black holes, leading to the conclusion that a large number of them are likely to have high spin[40,50]. Examples include the black holes centering the galaxies NGC 4051, NGC 1365, and MCG-6-30-15. Today, the Event Horizon Telescope (EHT) is expected to soon deliver unprecedented up-close images of the supermassive black holes at the centers of Milky Way (Sagittarius A*) and Messier 87 (M87)[39,51–56]. The latter, too, is a candidate high-spin black hole[57]. Therefore, extreme Kerr black holes, which spin at the maximally allowed theoretical limit, are of observational relevance.

Such black holes are also of particular interest from a theoretical perspective, which is the focus of this dissertation. Extreme Kerr is a critical point of the Kerr family: The region of spacetime in the immediate vicinity of its event horizon—the Near-Horizon Extreme Kerr (NHEK) region—solves the Einstein field equations on its own[43].

To obtain the NHEK metric, first consider the Kerr metric, which describes neutral rotating black holes of mass M and angular momentum $J = aM$. In Boyer-Lindquist coordinates $x^a \sim (\hat{t}, \hat{r}, \theta, \hat{\phi})$, it is given by

$$ds^2 = -\frac{\Delta}{\hat{\rho}^2}\left(d\hat{t} - a\sin^2\theta d\hat{\phi}\right)^2 + \frac{\sin^2\theta}{\hat{\rho}^2}\left((\hat{r}^2 + a^2)d\hat{\phi} - ad\hat{t}\right)^2 + \frac{\hat{\rho}^2}{\Delta}d\hat{r}^2 + \hat{\rho}^2 d\theta^2\,, \qquad (1.1)$$

where

$$\Delta(\hat{r}) = \hat{r}^2 - 2M\hat{r} + a^2\,, \qquad \hat{\rho}^2(\hat{r},\theta) = \hat{r}^2 + a^2\cos^2\theta\,.$$

This metric admits two Killing vectors, $\partial_{\hat{\phi}}$ and $\partial_{\hat{t}}$, generating axisymmetry and time-translation symmetry, respectively. Along every geodesic in Kerr, in addition to the conserved angular momentum and energy, the Carter constant is another conserved quantity.

Now we take the extreme Kerr limit

$$a = M, \tag{1.2}$$

and introduce dimensionless Bardeen-Horowitz coordinates

$$t = \frac{\hat{t}}{2M}\,, \quad \phi = \hat{\phi} - \frac{\hat{t}}{2M}\,, \quad r = \frac{\hat{r} - M}{M}\,. \tag{1.3}$$

Then the NHEK region is at

$$r \ll 1, \tag{1.4}$$

and the leading piece of the resulting metric takes the form[43]

$$ds^2 = 2M^2\Gamma(\theta)\left(-r^2dt^2 + \frac{dr^2}{r^2} + d\theta^2 + \Lambda(\theta)^2(d\phi + r\,dt)^2\right), \tag{1.5}$$

where

$$\Gamma(\theta) = \frac{1}{2}(1 + \cos^2\theta)\,, \qquad \Lambda(\theta) = \frac{2\sin\theta}{(1+\cos^2\theta)}. \tag{1.6}$$

The NHEK geometry has an enhanced $\mathsf{SL}(2,\mathbb{R}) \times \mathsf{U}(1)$ isometry, generated by the Killing vector fields

$$W_0 = \partial_\phi, \tag{1.7}$$

$$H_+ = \partial_t, \tag{1.8}$$

$$H_0 = t\,\partial_t - r\,\partial_r, \tag{1.9}$$

$$H_- = \left(t^2 + \frac{1}{r^2}\right)\partial_t - 2tr\,\partial_r - \frac{2}{r}\,\partial_\phi. \tag{1.10}$$

In particular, the time-translation symmetry is enlarged to an $\mathsf{SL}(2,\mathbb{R})$ global conformal symmetry, which includes dilations and special-conformal transformations. These enhanced symmetries greatly constrain and simplify gravitational dynamics in the NHEK region.

Over the past few years, they have rendered feasible a number of analytical computations of potentially observable astrophysical processes that could not otherwise be performed[1–3,44,58–75]. Such computations form the core of this dissertation. We consider exclusively high-spin black holes (extreme Kerr and near-extreme Kerr) and electromagnetic emissions in the near-horizon region. All our calculations are performed analytically.

In Chapter 2, we lay the groundwork for an exploration of the consequences of the enhanced symmetries on electromagnetic emissions from NHEK. The intense frame-dragging in this region leads to the expectation that such emissions peak near the superradiant bound, at which the ratio of the angular momentum to the energy is the Schwarzschild radius. We solve analytically, to leading order in the deviation from the superradiant bound, the equations for null geodesics that connect emission points in the NHEK region to observation points in the region far from the black hole. These are the trajectories of photons that start near the horizon and end at the telescope. Our solutions are obtained in terms of elementary functions only.

In Chapter 3, we surround the black hole with a geometrically thin, stationary, axisymmetric, equatorial disk of slowly accreting matter, and we assume that every particle in the disk emits monochromatic light isotropically in the form of photons that follow null geodesics. We use geometric optics developed in[76] and build upon the methods in Chapter 2 to treat photon trajectories originating from the NHEK region. The analytic formula we obtain for the observed flux, up to a proportionality constant, is independent of the disk model and therefore universal. We also propose a model for a radiant disk that respects the symmetries of NHEK. Due to the logarithmic divergence of the disk's proper length at extremality, this model implies a logarithmically divergent overall proportionality constant in the observed flux. Our result is directly relevant for the profile of FeKα line emissions that have been extensively analyzed in[32,77–80].

In Chapter 4, we start by assuming some physical process in NHEK capable of producing highly energetic photons and that it is invariant under the emergent symmetries of the background geometry. We predict the polarization profile of near-horizon emissions from M87, a candidate high-spin black hole. Our analytical computations produce polarimetric images measured by a distant observer stationed at a fixed polar angle (15° for M87) relative to the black hole's axis of symmetry. The polarization lines form a distinctive whorl that spirals into a central point inside the black shadow. An infinite series of subsidiary whorls also appear nearer the edge of the shadow, arising from photons that librate around the black hole multiple times before escaping to infinity. Moreover, we find that for any observation angle, the polarimetric images of these emissions lie within the black hole shadow and are not obscured by light from bright sources behind the black hole. Despite our focus on M87, whose polarization will be measured by the EHT[81–90], our methods and results apply to all high-spin black holes.

2

Photon Emission near Extreme Kerr

In this chapter, we study the electromagnetic emissions from the near-horizon region of an extreme Kerr black hole and analytically compute the geodesics of the corresponding photons.

Our analytical methods are an immediate consequence of the enhanced $\mathsf{SL}(2,\mathbb{R})\times\mathsf{U}(1)$ isometry group in the near-horizon geometry of extreme Kerr black holes. The intense frame-dragging in this region leads to the expectation that such emissions peak near the superradiant bound, at which the ratio of the angular momentum to the energy is the Schwarzschild radius. We solve analytically, to leading order in the deviation from the superradiant bound, the equations for null geodesics that connect emission points in the near-horizon region of an extreme Kerr to observation points in the region far from the black hole.[*] These are trajectories of photons that start near the horizon and end at the telescope. Our solutions are obtained in terms of elementary functions only.

Previously such geodesics were only known in terms of elliptic integrals and their inverse functions and were often studied numerically. For a general Kerr spacetime[91] collects the basic results in terms of elliptic integrals and[92,93] obtain the null geodesics in terms of elliptic and generalized hypergeometric functions respectively. These general results in terms of elliptic functions are highly complex and numerical codes[95–97] have been developed for astrophysical applications which require inversion with respect to various of their arguments.

The results in this chapter have been useful for the study of a variety of problems related to observations of electromagnetic radiation that originates from or passes through the NHEK region. Examples include the observed image of a light-emitting particle orbiting a black hole[44] and the profile of iron line emissions from an accretion disk[2].

The rest of the chapter is organized as follows. In Section 2.1 we set up the geodesic equations in Boyer-Lindquist and Bardeen-Horowitz coordinates and divide the spacetime into the near and the far regions. In Section 2.2 we analytically solve for the radial null geodesic motion in the $r-\theta$ plane. And in Section 2.3 we do the same for the motion in the $r-\phi$ and $r-t$ planes. Finally we summarize

---

[*] The r, ϕ and t equations are solved generically while the θ equation is solved only in special cases.

the results Section 2.4.

2.1 GEODESIC EQUATIONS

The Kerr metric in Boyer-Lindquist coordinates $x^a \sim (\hat{t}, \hat{r}, \theta, \hat{\phi})$ is given by:

$$\begin{aligned} ds^2 &= g_{ab} dx^a dx^b \\ &= -\frac{\Delta}{\hat{\rho}^2}\left(d\hat{t} - a\sin^2\theta d\hat{\phi}\right)^2 + \frac{\sin^2\theta}{\hat{\rho}^2}\left((\hat{r}^2+a^2)d\hat{\phi} - a d\hat{t}\right)^2 + \frac{\hat{\rho}^2}{\Delta}d\hat{r}^2 + \hat{\rho}^2 d\theta^2 \, , \end{aligned} \tag{2.1}$$

where

$$\Delta(\hat{r}) = \hat{r}^2 - 2M\hat{r} + a^2 \, , \qquad \hat{\rho}^2(\hat{r}, \theta) = \hat{r}^2 + a^2\cos^2\theta \, .$$

This describes neutral rotating black holes of mass M and angular momentum $J = aM$. The general form of the geodesic equation for $x^a(\tau)$ with affine parameter τ is

$$\partial_\tau^2 x^a + \Gamma^a_{bc}\partial_\tau x^b \partial_\tau x^c = 0 \, , \quad g_{ab}\partial_\tau x^a \partial_\tau x^b = -\mu^2 \, , \tag{2.2}$$

where $\mu = 0$ for null geodesics and $\mu = 1$ for time-like geodesics. In the Kerr spacetime there are three additional conserved quantities along every geodesic:

$$\begin{aligned}
\hat{E} &= -g_{\hat{t}a}\partial_\tau x^a\,, \\
\hat{L} &= g_{\hat{\phi}a}\partial_\tau x^a\,, \\
Q &= Y_{ab}\partial_\tau x^a\partial_\tau x^b - (\hat{L} - a\hat{E})^2\,.
\end{aligned} \tag{2.3}$$

$\hat{E}$ and $\hat{L}$ are the energy and axial angular momentum. The Carter constant Q here is constructed from the Killing tensor (square of Killing-Yano),

$$\begin{aligned}
Y_{ab}dx^a dx^b &= a^2\cos^2\theta\left[\frac{\Delta}{\hat{\rho}^2}(d\hat{t} - a\sin^2\theta d\hat{\phi})^2 - \frac{\hat{\rho}^2}{\Delta}d\hat{r}^2\right] \\
&\quad + \hat{r}^2\left[\frac{\sin^2\theta}{\hat{\rho}^2}\left(ad\hat{t} - (\hat{r}^2 + a^2)d\hat{\phi}\right)^2 + \hat{\rho}^2 d\theta^2\right]\,.
\end{aligned} \tag{2.4}$$

These conservation laws enable integration of the geodesic equation into the form[42]

$$\int^{\hat{r}} \frac{d\hat{r}'}{\sqrt{\hat{R}}} = \int^{\theta} \frac{d\theta'}{\sqrt{\hat{\Theta}}}\,, \tag{2.5}$$

$$\hat{\phi} = \int^{\hat{r}} \frac{a\hat{E}\hat{r}'^2 + (\hat{L} - a\hat{E})(\Delta - a^2)}{\Delta\sqrt{\hat{R}}}d\hat{r}' + \int^{\theta} \frac{\hat{L}\cot^2\theta'}{\sqrt{\hat{\Theta}}}d\theta'\,, \tag{2.6}$$

$$\hat{t} = \int^{\hat{r}} \frac{\hat{E}\hat{r'}^2(\hat{r'}^2 + a^2) + a(\hat{L} - a\hat{E})(\Delta - \hat{r'}^2 - a^2)}{\Delta\sqrt{\hat{R}}} d\hat{r}' + \int^{\theta} \frac{a^2 \hat{E} \cos^2\theta'}{\sqrt{\hat{\Theta}}} d\theta' \,, \tag{2.7}$$

where

$$\begin{aligned} \hat{R} &= \left(\hat{E}(\hat{r'}^2 + a^2) - \hat{L}a\right)^2 - \Delta\left(\mu^2\hat{r'}^2 + (\hat{L} - a\hat{E})^2 + Q\right) \,, \qquad (2.8) \\ \hat{\Theta} &= Q - \cos^2\theta' \left(a^2(\mu^2 - \hat{E}^2) + \hat{L}^2/\sin^2\theta'\right) \,. \qquad (2.9) \end{aligned}$$

The integrals are understood to be path integrals along the trajectory. At every point of the trajectory the conditions $\hat{R} \geq 0 \,, \hat{\Theta} \geq 0$ must hold but the signs of $d\hat{r'}$, $d\theta'$ and $\sqrt{\hat{R}}$, $\sqrt{\hat{\Theta}}$ change at corresponding turning points in such a way that $d\hat{r}'/\sqrt{\hat{R}}$ and $d\theta'/\sqrt{\hat{\Theta}}$ are always positive.

We consider null geodesics,

$$\mu = 0 \,, \tag{2.10}$$

in the extreme Kerr spacetime,

$$a = M, \tag{2.11}$$

which are near the so-called superradiant bound:

$$\lambda = 1 - \frac{\hat{L}}{2M\hat{E}} \ll 1. \tag{2.12}$$

In this case we will find that, to leading order in λ, the radial integrals in (2.5—2.7) are soluble in terms of elementary functions. As already noted by Bardeen in[98], $\lambda = 0$ is a special point in the parameter space of extreme Kerr geodesics and one expects many photons emitted from the near-horizon region to have small λ. It is therefore gratifying that this case is explicitly soluble.

It is convenient to introduce the dimensionless Bardeen-Horowitz coordinates,

$$t = \frac{\hat{t}}{2M}\,, \quad \phi = \hat{\phi} - \frac{\hat{t}}{2M}\,, \quad r = \frac{\hat{r} - M}{M}\,. \tag{2.13}$$

The near-horizon region is then $r \ll 1$, and the metric takes the form[43]

$$ds^2 = 2M^2\Gamma(\theta)\left(-r^2dt^2 + \frac{dr^2}{r^2} + d\theta^2 + \Lambda(\theta)^2(d\phi + rdt)^2\right) + \dots\,, \tag{2.14}$$

where

$$\Gamma(\theta) = \frac{1}{2}(1 + \cos^2\theta)\,, \qquad \Lambda(\theta) = \frac{2\sin\theta}{(1 + \cos^2\theta)}, \tag{2.15}$$

and the subleading corrections are suppressed by powers of r. The leading term displayed on the right hand side solves the Einstein equation on its own. It is referred to as the Near-Horizon Extreme Kerr or 'NHEK' metric and has an enhanced symmetry group[43,99]. The coordinates (2.13) are particularly well-suited for studying near horizon physics in extreme and near-extreme Kerr. For example, they may be used to resolve the prograde circular photon and innermost stable orbits whose Boyer-Lindquist radial coordinates degenerate in the extreme limit with that of the horizon (see, e.g., the appendix in[65]). We are interested in trajectories of photons emitted near the horizon and observed by a distant telescope. These are geodesics which start at $(t_n, r_n, \theta_n, \phi_n)$ with $r_n \ll 1$ in the NHEK region and end at $(t_f, r_f, \theta_f, \phi_f)$ with $r_f \gg 1$ in the far asymptotically flat region.

In the null case $\hat{E}$ may be scaled out of the geodesic equation, whose solutions are labeled by λ and the convenient dimensionless shifted Carter constant

$$q^2 = 3 - \frac{Q}{M^2 \hat{E}^2} < 4(1 - \lambda + \lambda^2) \,, \tag{2.16}$$

where the last inequality expresses positivity of the kinetic energy in a local frame. We will show below that, given (2.12), a geodesic that originates in NHEK and reaches out to the far asymptotically flat region must have a positive q^2. We will take $q > 0$ and hold it fixed while expanding in small λ. Motion in the equatorial plane has $q = \sqrt{3}$.

In terms of the coordinates (2.13) and parameters (2.12) and (2.16) the geodesic equations (2.5—2.7) become:

$$\int_{r_n}^{r_f} \frac{dr}{\sqrt{R}} = \int_{\theta_n}^{\theta_f} \frac{d\theta}{\sqrt{\Theta}} \,, \tag{2.17}$$

$$\phi_f - \phi_n = -\frac{1}{2} \int_{r_n}^{r_f} \frac{\Phi}{r\sqrt{R}} dr + \frac{1}{2} \int_{\theta_n}^{\theta_f} \frac{(3 + \cos^2\theta - 4\lambda)\cot^2\theta}{\sqrt{\Theta}} d\theta \,, \tag{2.18}$$

$$t_f - t_n = \frac{1}{2} \int_{r_n}^{r_f} \frac{T}{r^2\sqrt{R}} dr + \frac{1}{2} \int_{\theta_n}^{\theta_f} \frac{\cos^2\theta}{\sqrt{\Theta}} d\theta \,, \tag{2.19}$$

where

$$R = r^4 + 4r^3 + (q^2 + 8\lambda - 4\lambda^2)r^2 + 8\lambda r + 4\lambda^2\,, \tag{2.20}$$

$$\Theta = 3 - q^2 + \cos^2\theta - 4(1-\lambda)^2\cot^2\theta\,, \tag{2.21}$$

$$\Phi = r^3 + 4r^2 + (3 + 4\lambda)r + 4\lambda\,, \tag{2.22}$$

$$T = r^4 + 4r^3 + 7r^2 + 4(1+\lambda)r + 4\lambda\,. \tag{2.23}$$

The integrals in (2.17—2.19) are of elliptic type and are often manipulated numerically. In this chapter we will perform the radial integrals analytically to leading order in small λ using the method of matched asymptotic expansions (MAE) for all geodesics extending from the near to the far region. Our solutions are obtained in terms of elementary functions only. We will proceed in the small λ regime by dividing the spacetime into two regions:

$$\text{Near Region} \quad r \ll 1\,, \tag{2.24}$$

$$\text{Far Region} \quad r \gg \sqrt{\lambda}\,. \tag{2.25}$$

The two regions overlap in the

$$\text{Overlap Region} \quad \sqrt{\lambda} \ll r \ll 1\,. \tag{2.26}$$

We now proceed to solve the equations in the near and far regions and match the solutions in the overlap region.

2.2 The r–θ motion

In this section we solve the radial integral

$$I = \int_{r_n}^{r_f} \frac{dr}{\sqrt{R(r)}}\,, \tag{2.27}$$

to leading order in λ via MAE. Given (2.12) we have that

$$R \approx r^4 + 4r^3 + q^2 r^2 + 8\lambda r + 4\lambda^2\,. \tag{2.28}$$

In the near region (2.24) we have

$$R_n(r) = R(r \ll 1) = q^2 r^2 + 8\lambda r + 4\lambda^2\,, \tag{2.29}$$

while in the far region (2.25) we have

$$R_f(r) = R(r \gg \sqrt{\lambda}) = r^2(r^2 + 4r + q^2)\,. \tag{2.30}$$

We first check the conditions under which small λ geodesics in the near and far regions connect.

Turning points in the radial motion occur at the zeroes of $R(r)$. In the far region these are located at

$$r_{f\pm} = -2 \pm \sqrt{4 - q^2}\,. \tag{2.31}$$

If q^2 is positive, this has no turning points with positive r. On the other hand, if q^2 is negative, there is a turning point at positive r, and the geodesic bounces off the black hole before it penetrates the near region. We therefore take

$$q^2 > 0\,, \tag{2.32}$$

ignoring the measure zero case $q = 0$. In the near region the zeroes are at

$$r_{n\pm} = \frac{2\lambda}{q^2}\left(-2 \pm \sqrt{4 - q^2}\right)\,. \tag{2.33}$$

Since $0 < q^2 < 4$ to leading order in λ, the square root is always a positive number less than 2. Hence there is a positive root if and only if λ is negative. In that case, a geodesic emanating from the horizon will turn around before it reaches the far region at $r \sim \sqrt{\lambda}$. This is due to the fact that photons on such trajectories exceed the superradiant bound. On the other hand, there are two turning points, and if the geodesic originates in the near region but outside both turning points, $r > r_{n\pm}$, it can reach the far region. Hence λ can have either sign but geodesics with negative λ cannot get all the way to the horizon.

To leading order in λ the near and far radial integrals can now be performed explicitly:

$$\begin{aligned} I_n(r) &= \int^r \frac{dr'}{\sqrt{R_n(r')}} = \frac{1}{q} \ln \left(q\sqrt{R_n(r)} + q^2 r + 4\lambda \right) + C_n \,, && (2.34) \\ I_f(r) &= \int^r \frac{dr'}{\sqrt{R_f(r')}} = -\frac{1}{q} \ln \frac{1}{r^2} \left(q\sqrt{R_f(r)} + q^2 r + 2r^2 \right) + C_f \,, && (2.35) \end{aligned}$$

where C_n, C_f are integration constants. In the overlap region (2.26) we have:

$$\begin{aligned} I_n(r) &= \frac{1}{q} \left(\ln r + \ln 2q^2 + q\, C_n + \frac{4\lambda}{q^2 r} + \ldots \right) \,, && (2.36) \\ I_f(r) &= \frac{1}{q} \left(\ln r - \ln 2q^2 + q\, C_f - \frac{2r}{q^2} + \ldots \right) \,. && (2.37) \end{aligned}$$

Matching $I_n = I_f$ in the overlap region we find:

$$C_f = C_n + \frac{2}{q} \ln 2q^2 \,. \tag{2.38}$$

The integral (2.27) is given by $I = I_f(r_f) - I_n(r_n)$ and using (2.34), (2.35), and (2.38) we find:

$$I = -\frac{1}{q} \ln \frac{\left(qD_n + q^2 r_n + 4\lambda \right) \left(qD_f + 2r_f + q^2 \right)}{4q^4\, r_f} \,, \tag{2.39}$$

where,

$$\begin{aligned} D_n &= \sqrt{R_n(r_n)} = \sqrt{q^2 r_n^2 + 8\lambda r_n + 4\lambda^2} \,, && (2.40) \\ D_f &= \frac{1}{r_f} \sqrt{R_f(r_f)} = \sqrt{r_f^2 + 4r_f + q^2} \,. && (2.41) \end{aligned}$$

2.3 THE r–ϕ AND r–t MOTION

Given (2.12) we have that

$$\Phi \approx r^3 + 4r^2 + 3r + 4\lambda \,, \tag{2.42}$$

$$T \approx r^4 + 4r^3 + 7r^2 + 4r + 4\lambda \,, \tag{2.43}$$

and we can perform the radial integrals for the r–ϕ and r–t motion in (2.18) and (2.19),

$$I^\phi = \int_{r_n}^{r_f} \frac{\Phi(r)}{r\sqrt{R(r)}} dr \,, \quad I^t = \int_{r_n}^{r_f} \frac{T(r)}{r^2\sqrt{R(r)}} dr \,, \tag{2.44}$$

via MAE as follows.

In the near region (2.24) we have

$$\Phi_n(r) = \Phi(r \ll 1) = 3r + 4\lambda \,, \tag{2.45}$$

$$T_n(r) = T(r \ll 1) = 4r + 4\lambda \,, \tag{2.46}$$

while in the far region (2.25) we have

$$\Phi_f(r) = \Phi(r \gg \sqrt{\lambda}) = r(r^2 + 4r + 3) \,, \tag{2.47}$$

$$T_f(r) = T(r \gg \sqrt{\lambda}) = r(r^3 + 4r^2 + 7r + 4) \,. \tag{2.48}$$

All integrals are now doable:

$$\begin{aligned} I_n^\phi(r) = \int^r \frac{\Phi_n(r')}{r'\sqrt{R_n(r')}}dr' \quad &= \quad \frac{3}{q}\ln\left(q\sqrt{R_n(r)}+q^2r+4\lambda\right)- \\ &\quad\; -2\ln\frac{1}{r}\left(\sqrt{R_n(r)}+2r+2\lambda\right)+C_n^\phi\,, \end{aligned} \tag{2.49}$$

$$\begin{aligned} I_f^\phi(r) = \int^r \frac{\Phi_f(r')}{r'\sqrt{R_f(r')}}dr' \quad &= \quad -\frac{3}{q}\ln\frac{1}{r^2}\left(q\sqrt{R_f(r)}+q^2r+2r^2\right)+ \\ &\quad\; +2\ln\frac{1}{r}\left(\sqrt{R_f(r)}+r^2+2r\right)+\frac{1}{r}\sqrt{R_f(r)}+C_f^\phi\,, \end{aligned} \tag{2.50}$$

$$I_n^t(r) = \int^r \frac{T_n(r')}{r'^2\sqrt{R_n(r')}}dr' \quad = \quad -\frac{1}{\lambda r}\sqrt{R_n(r)}+C_n^t\,, \tag{2.51}$$

$$\begin{aligned} I_f^t(r) = \int^r \frac{T_f(r')}{r'^2\sqrt{R_f(r')}}dr' \quad &= \quad -\frac{7q^2-8}{q^3}\ln\frac{1}{r^2}\left(q\sqrt{R_f(r)}+q^2r+2r^2\right)+ \\ &\quad\; +2\ln\frac{1}{r}\left(\sqrt{R_f(r)}+r^2+2r\right)+\frac{q^2r-4}{q^2r^2}\sqrt{R_f(r)}+C_f^t\,, \end{aligned} \tag{2.52}$$

where $C_n^{\phi,t}, C_f^{\phi,t}$ are integration constants. In the overlap region (2.26) we have:

$$I_n^\phi(r) \quad = \quad \frac{1}{q}\left(3\ln r+3\ln 2q^2+q\left(C_n^\phi-2\ln(q+2)\right)-\frac{4\lambda(q^2-3)}{q^2r}+\dots\right)\,, \tag{2.53}$$

$$I_f^\phi(r) \quad = \quad \frac{1}{q}\left(3\ln r-3\ln 2q^2+q\left(C_f^\phi+2\ln(q+2)\right)+q^2+\frac{2(2q^2-3)r}{q^2}+\dots\right) \tag{2.54}$$

$$I_n^t(r) \quad = \quad -\frac{1}{q}\left(\frac{q^2}{\lambda}-q\,C_n^t+\frac{4}{r}+\frac{2\lambda(q^2-4)}{q^2r^2}+\dots\right)\,, \tag{2.55}$$

$$\begin{aligned} I_f^t(r) \quad &= \quad -\frac{1}{q}\left(\frac{4}{r}-\frac{7q^2-8}{q^2}\ln r-\frac{q^4-(7q^2-8)\ln 2q^2-8}{q^2}-\right. \\ &\qquad\qquad \left. -q\left(C_f^t+2\ln(q+2)\right)-\frac{4(q^4-4q^2+6)r}{q^4}+\dots\right)\,, \end{aligned} \tag{2.56}$$

so matching $I_n^{\phi,t} = I_f^{\phi,t}$ in the overlap region we find:

$$\begin{aligned}
C_f^{\phi} &= C_n^{\phi} + \frac{6}{q} \ln 2q^2 - 4\ln(q+2) - q\,, && (2.57)\\
C_f^{t} &= C_n^{t} - \frac{q}{\lambda} - \frac{q^4 - (7q^2-8)\ln 2q^2 - 8}{q^3} - 2\ln(q+2) && (2.58)\\
&\approx C_n^{t} - \frac{q}{\lambda}\,,
\end{aligned}$$

where in the last line we have used (2.12). The integrals (2.44) are given by $I^{\phi,t} = I_f^{\phi,t}(r_f) - I_n^{\phi,t}(r_n)$ and using (2.49—2.52) and (2.57—2.58) we find:

$$\begin{aligned}
I^{\phi} &= -\frac{3}{q} \ln \frac{1}{r_f} \left(qD_n + q^2 r_n + 4\lambda\right)\left(qD_f + 2r_f + q^2\right) \\
&\quad +2\ln \frac{1}{r_n} \left(D_n + 2r_n + 2\lambda\right) + \left(D_f + r_f + 2\right) && (2.59)\\
&\quad +D_f + \frac{6}{q} \ln 2q^2 - 4\ln(q+2) - q\,, \\
I^{t} &= 2\ln\left(D_f + r_f + 2\right) - \frac{7q^2-8}{q^3} \ln \frac{1}{r_f} \left(qD_f + 2r_f + q^2\right) && (2.60)\\
&\quad + \frac{q^2 r_f - 4}{q^2 r_f} D_f + \frac{1}{\lambda r_n} D_n - \frac{q}{\lambda}\,.
\end{aligned}$$

In the special case of motion confined to the equatorial plane the geodesic equations reduce to (2.18) and (2.19) with the θ integrals dropped. In this case the shifts in the azimuthal angle ϕ and time t are given by $\phi_f - \phi_n = -(1/2)\, I^{\phi}\,|_{q=\sqrt{3}}$ and $t_f - t_n = (1/2)\, I^{t}\,|_{q=\sqrt{3}}$ respectively, or explicitly:

$$\begin{aligned}
\phi_f - \phi_n &= \frac{\sqrt{3}}{2}\ln\frac{1}{r_f}\left(\sqrt{3}\,\mathcal{D}_n + 3r_n + 4\lambda\right)\left(\sqrt{3}\,\mathcal{D}_f + 2r_f + 3\right) \\
&\quad - \ln\frac{1}{r_n}\left(\mathcal{D}_n + 2r_n + 2\lambda\right)\left(\mathcal{D}_f + r_f + 2\right) && (2.61) \\
&\quad - \frac{1}{2}\mathcal{D}_f - \sqrt{3}\ln 6 + 2\ln(\sqrt{3}+2) + \frac{\sqrt{3}}{2}\,, \\
t_f - t_n &= \ln\left(\mathcal{D}_f + r_f + 2\right) - \frac{13}{6\sqrt{3}}\ln\frac{1}{r_f}\left(\sqrt{3}\,\mathcal{D}_f + 2r_f + 3\right) && (2.62) \\
&\quad + \frac{3r_f - 4}{6r_f}\mathcal{D}_f + \frac{1}{2\lambda r_n}\mathcal{D}_n - \frac{\sqrt{3}}{2\lambda}\,,
\end{aligned}$$

with

$$\mathcal{D}_n = D_n\big|_{q=\sqrt{3}} = \sqrt{3r_n^2 + 8\lambda r_n + 4\lambda^2}\,, \tag{2.63}$$

$$\mathcal{D}_f = D_f\big|_{q=\sqrt{3}} = \sqrt{r_f^2 + 4r_f + 3}. \tag{2.64}$$

These are the equations that relate an endpoint of an equatorial null geodesic near the horizon (t_n, r_n, ϕ_n) to its endpoint in the region far from the black hole (t_f, r_f, ϕ_f) and the associated constant λ along the geodesic.

For geodesics which move in the θ direction we note that positivity of the shifted Carter constant q^2 (derived in (2.32) for all geodesics which connect between the near and far regions) restricts the values of θ that these geodesics may possibly explore. This is because $\Theta \geq 0$ then implies $3+\cos^2\theta - 4\cot^2\theta \geq 0$ which means that θ must lie between $\theta_0 = \arccos\sqrt{2\sqrt{3}-3} \approx 47^\circ$ and $\pi - \theta_0 \approx 133^\circ$. This fact has been derived previously from an analysis of the NHEK geodesics alone in[100].

Finally, it is worth mentioning that while in our expansion in small λ we have been keeping q^2 fixed and finite, all of the equations and statements derived in this chapter are also true for the case of small q^2 provided that it remains $q^2 \gg \sqrt{\lambda}$. In this case the only thing that needs to be modified are the definitions of the near region (2.24) to $r \ll \min\left(1, q^2\right)$ and the overlap region (2.26) to $\sqrt{\lambda} \ll r \ll \min\left(1, q^2\right)$.

2.4 SUMMARY

In this chapter, we studied null geodesics in the extreme Kerr spacetime. We used the method of matched asymptotic expansions to integrate, to leading order in the deviation from the superradiant bound, all radial integrals in Carter's integral geodesic equations. The key equations we derived are (2.39), (2.59), and (2.60). In the special case of motion confined to the equatorial plane, we derived the equations (2.61, 2.62), which relate an endpoint of a null geodesic near the horizon to its endpoint in the region far from the black hole and the associated angular momentum constant along the geodesic.[†]

All our results are expressed in terms of elementary functions only. This is a critical improvement over previous results in the literature, which were only known in terms of elliptic functions and their generalizations. It enables one to solve explicitly for various parameters appearing in the integral geodesic equations, a step that is often necessary for various applications. For example, building upon the methods in this chapter and using geometrical optics developed in[76,101], one may obtain observables related to the propagation of electromagnetic radiation from the near-horizon region of

---

[†] App. 4.A3 explores θ-motions in terms of elliptic functions.

extreme Kerr black holes. These include broadened FeKα emission lines[2] and images of orbiting hot spots[44].

3

Accretion Disk Flux

In this chapter, we analytically compute the broadening of electromagnetic line emissions originating from the innermost part of a radiant accretion disk around a high-spin black hole.

The observational signatures of black holes depend sensitively on their surroundings and can be influenced by myriad other elements present in their environment (such as their magnetosphere, corona, jets, etc.), each of which carries its own degrees of freedom. Therefore, when making predictions for observations by telescopes, the common strategy is to produce many templates covering as much of this parameter space as possible. But we can also investigate the inverse problem: Is there a region in parameter space that produces a distinctive signature so its observation would explain the nature of the source?

A distinctive corner in the parameter space is occupied by rapidly spinning black holes that saturate the Kerr bound for a black hole's angular momentum with respect to its mass, $J \leq M^2$. In this regime, an enhancement of symmetry in the immediate vicinity of the black hole's horizon[43,99] allows for an analytic study of a variety of potentially observable phenomena[1–3,44,58–75], which often exhibit a striking universality. A characteristic example, which is relevant for the computation in this chapter, is the observation[1,44,98] that all of the light emitted from the near-vicinity of a rapidly spinning black hole is constrained to appear on the so-called NHEKline: a vertical line segment on the edge of the shadow of every high-spin black hole.

We surround the black hole with a geometrically thin, stationary, axisymmetric, equatorial disk of slowly accreting matter, and we assume that every particle in the disk emits monochromatic light isotropically in the form of photons that follow null geodesics. Using geometric optics developed in[76] and building upon the methods in Chapter 2, we compute the broadening of electromagnetic line emissions observed along the NHEKline. The resulting flux is independent of the disk's surface emissivity and therefore universal.

The rest of the chapter is organized as follows. In Section 3.1 we present the main result. In Section 3.2 we review the method of geometric optics, which may be used to obtain the flux observed at infinity as a function of the photons' redshift, $F_o(g)$. In Section 3.3 we use this method to treat photon trajectories originating from the NHEK region in extreme Kerr and obtain an analytic formula for $F_o(g)$. Up to a proportionality constant, the result is independent of the disk model. And in Section 3.4 we generalize the result to the case of a near-extreme Kerr. In Section 3.5 we propose a model for a radiant disk that respects the symmetries of NHEK. Due to the logarithmic divergence of the disk's proper length at extremality, this model implies a logarithmically divergent overall proportionality constant in $F_o(g)$. Finally we summarize the results Section 3.6.

3.1 MAIN RESULT

We now present the main result of the chapter: the observed flux due to emissions from the accretion disk of a high-spin black hole.

Suppose the observer's screen has Cartesian coordinates (α, β) and is located at a dimensionless coordinate distance $r_o \gg 1$ from the black hole, at a polar angle θ_o with respect to the hole's rotation axis. The observer receives nonvanishing flux $F_o(g)$ provided $\theta_o \in (\theta_c, \pi - \theta_c)$, with $\theta_c = \arccos \sqrt{2\sqrt{3} - 3}$, and $g \in \left(1/\sqrt{3}, \sqrt{3}\right)$. The flux is given by

$$F_o \propto \frac{1}{M^3 r_o^2 \sin\theta_o} \frac{g\left(g - 1/\sqrt{3}\right)\left(g + \sqrt{3}\right)}{\sqrt{4g^2\left(3 + \cos^2\theta_o - 4\cot^2\theta_o\right) - 3\left(g - 1/\sqrt{3}\right)\left(5g + \sqrt{3}\right)}}. \tag{3.1}$$

This result holds independently of the details of the disk (which only enter through the proportionality constant). It is directly relevant for the profile of FeKα line emissions which have been extensively

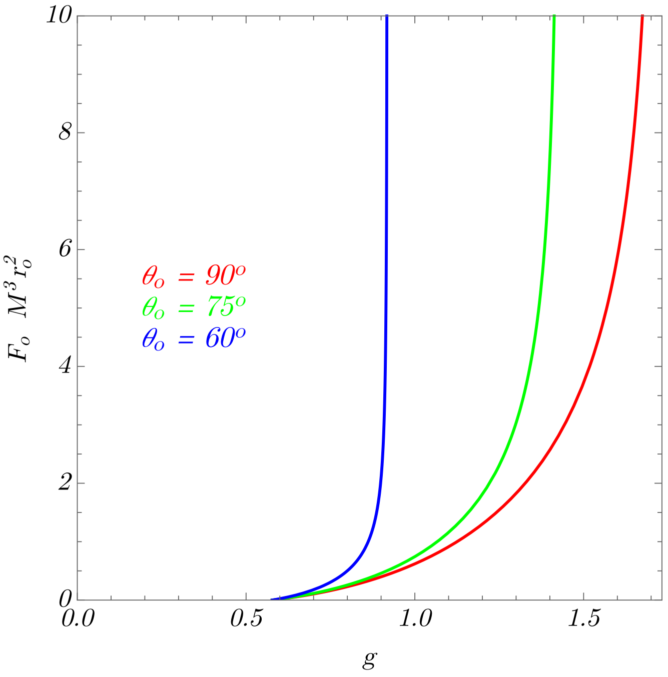

Figure 3.1: The profile of line emissions from the near-horizon region of a (near-)extremal black hole [Eq. (3.1)]. This is our main result: an analytic expression for the flux F_o measured by an observer at dimensionless radius r_o and polar angle θ_o from the hole as a function of the redshift g. The result is independent of the disk's surface emissivity and therefore universal. This is an example of critical behavior in astronomy. Note that all the divergences in these plots are integrable. They arise from emissions that are aimed directly at the observer, in that they appear at the center of the NHEKline shown in Fig. (??).

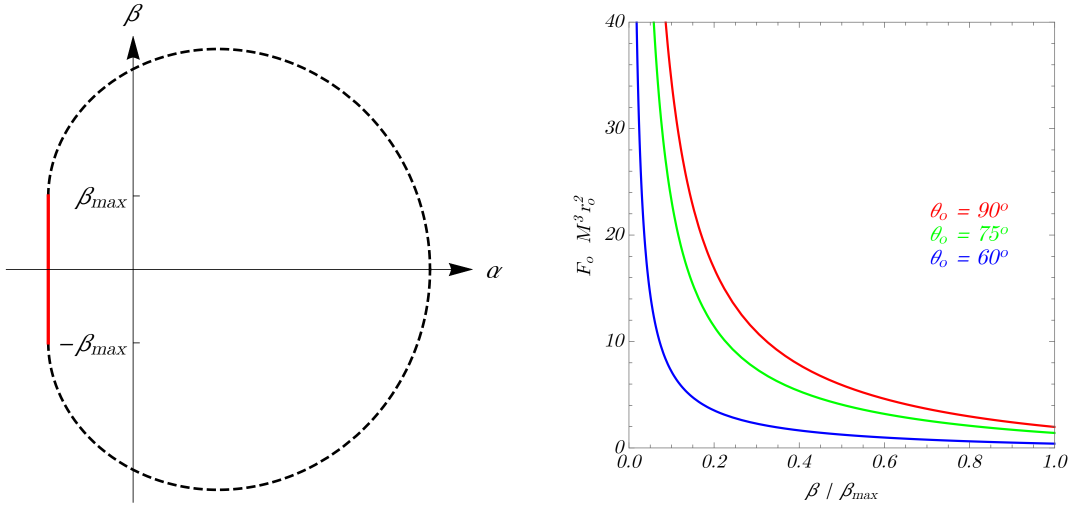

Figure 3.2: In the high-spin regime, the shadow that a black hole casts on a distant observer's screen develops a vertical edge: the NHEKline [Eq. (4.33)], depicted in red in the left panel. All electromagnetic emissions from the near-horizon region, including those from the innermost part of its accretion disk, are constrained to emerge on this vertical line segment. The line emissions from the near-horizon region computed in this chapter may be thought of as brightness profiles along the NHEKline and we plot them as such on the right panel. The divergences are likely due to the caustics discussed in Ref.[44], which should be regulated by diffraction effects beyond our geometric optics approximation.

analyzed in [32,77–80] (see also, e.g., the reviews [102–104]). Furthermore, we find that the flux F_o emerges on the NHEKline, defined on the observer's screen by [44]

$$\alpha = -2M \csc\theta_o, \qquad |\beta| < \beta_{\text{max}} = M\sqrt{3+\cos^2\theta_o - 4\cot^2\theta_o}, \tag{3.2}$$

at an elevation β which is completely fixed by the redshift g according to

$$\beta = \pm M\sqrt{3+\cos^2\theta_o - 4\cot^2\theta_o - \frac{3}{4g^2}\left(g-1/\sqrt{3}\right)\left(5g+\sqrt{3}\right)}. \tag{3.3}$$

It follows that, for a suitable source line, a high-resolution telescope such as EHT might be able to observe the critical flux 3.1 as a characteristic brightness profile along the NHEKline.

3.2 Electromagnetic line emissions from a black hole accretion disk

The profile of electromagnetic line emissions from a disk of matter accreting onto a black hole is commonly computed via the geometric optics methods developed by Bardeen and Cunningham [76,98,101]. In this section, we review how this is done for the case of emissions originating from a slowly accreting equatorial disk that is geometrically thin.

Astrophysically realistic black holes are described by the Kerr family of metrics, parameterized by their mass M and angular momentum $J = aM$. In Boyer-Lindquist coordinates, the Kerr line element is

$$ds^2 = -\frac{\Delta}{\Sigma}\left(\mathrm{d}t - a\sin^2\theta\,\mathrm{d}\phi\right)^2 + \frac{\Sigma}{\Delta}\,\mathrm{d}\hat{r}^2 + \Sigma\,\mathrm{d}\theta^2 + \frac{\sin^2\theta}{\Sigma}\left[\left(\hat{r}^2 + a^2\right)\mathrm{d}\phi - a\,\mathrm{d}t\right]^2, \tag{3.4}$$

where

$$\Delta(\hat{r}) = \hat{r}^2 - 2M\hat{r} + a^2, \qquad \Sigma(\hat{r},\theta) = \hat{r}^2 + a^2\cos^2\theta. \tag{3.5}$$

A particle orbiting on a prograde, circular, equatorial geodesic at radius $\hat{r} = \hat{r}_s$ has four-velocity[21]

$$u_s = u_s^t\left(\partial_t + \Omega_s\,\partial_\phi\right), \tag{3.6}$$

where

$$u_s^t = \frac{\hat{r}_s^{3/2} + aM^{1/2}}{\sqrt{\hat{r}_s^3 - 3M\hat{r}_s^2 + 2aM^{1/2}\hat{r}_s^{3/2}}}, \qquad \Omega_s = \frac{M^{1/2}}{\hat{r}_s^{3/2} + aM^{1/2}}. \tag{3.7}$$

Here and hereafter, the subscript s stands for source. Such an orbit is stable as long as

$$\hat{r}_s \geq \hat{r}_{\mathrm{ISCO}} = M\left(3 + Z_2 - \sqrt{\left(3 - Z_1\right)\left(3 + Z_1 + 2Z_2\right)}\right), \tag{3.8}$$

where $\hat{r}_{\text{ISCO}}$ denotes the radius of the Innermost Stable Circular Orbit (ISCO), with

$$Z_1 = 1 + \left(1 - a_\star^2\right)^{1/3} \left[(1 + a_\star)^{1/3} + (1 - a_\star)^{1/3}\right], \tag{3.9}$$

$$Z_2 = \left(3a_\star^2 + Z_1^2\right)^{1/2}, \tag{3.10}$$

where $a_\star = a/M$.

In this chapter, we consider a Kerr black hole (4.4) surrounded by a thin accretion disk consisting of particles falling along the equatorial geodesics described by the four-velocity (3.6). Their actual four-velocity may also have a vertical component for motion in and out of the equator, as well as a radial component providing the disk with a nonzero accretion rate. However, we will assume these components to be small relative to the angular velocity, so that we may treat the particles' orbits as circular. In the region outside the ISCO, this assumption is valid for slowly accreting disks (e.g., it has been carefully established in the context of the Novikov-Thorne model[105–107]).

The particles in the disk can emit radiation that flows along null geodesics to reach a distant observer at radius r_o and polar angle θ_o. Here and hereafter, the subscript o stands for observer. By the reflection symmetry of the problem, we may assume without loss of generality that the observer lies in the northern hemisphere, $\theta_o \in (0, \pi/2)$.[*] We also assume that the disk is stationary and axisymmetric, in which case it suffices to consider the null geodesic motion in the (r, θ) plane only.

Let p denote the four-momentum of the null geodesic corresponding to a photon trajectory connecting a source point to the observer. For such geodesics, the energy $E = -p_t$ may be scaled out of

---

[*] In this chapter, we ignore the measure-zero, degenerate cases of a precisely face-on ($\theta_o = 0$) or precisely edge-on ($\theta_o = \pi/2$) observer.

the geodesic equation, whose solutions may therefore be labeled by

$$\hat{\lambda} = \frac{L}{E}, \qquad \hat{q} = \frac{\sqrt{Q}}{E}, \tag{3.11}$$

where $L = p_\phi$ denotes the component of angular momentum parallel to the axis of symmetry and $Q = p_\theta^2 - \cos^2\theta(a^2 p_t^2 - p_\phi^2 \csc^2\theta)$ is the Carter constant.[†] The null geodesic equation in the (r, θ) plane is given by

$$\int_{\hat{r}_s}^{\hat{r}_o} \frac{\mathrm{d}\hat{r}}{\pm\sqrt{\hat{R}(\hat{r})}} = \int_{\theta_s}^{\theta_o} \frac{\mathrm{d}\theta}{\pm\sqrt{\hat{\Theta}(\theta)}}, \tag{3.12}$$

where

$$\hat{R}(\hat{r}) = \left(\hat{r}^2 + a^2 - a\hat{\lambda}\right)^2 - \Delta\left[\hat{q}^2 + (a - \hat{\lambda})^2\right], \tag{3.13}$$

$$\hat{\Theta}(\theta) = \hat{q}^2 + a^2\cos^2\theta - \hat{\lambda}^2\cot^2\theta. \tag{3.14}$$

These integrals are line integrals along a trajectory connecting the source and observer, with the signs chosen so that the integrals grow secularly. Since the emitted energy of the photon is $E_s = -p \cdot u_s$ and the energy at the distant observer is the conserved quantity $E_o = E = -p_t$, the redshift factor is[76]

$$g = \frac{E_o}{E_s} = \frac{\sqrt{\hat{r}_s^3 - 3M\hat{r}_s^2 + 2aM^{1/2}\hat{r}_s^{3/2}}}{\hat{r}_s^{3/2} + M^{1/2}(a - \hat{\lambda})}. \tag{3.15}$$

[†] Note that $\hat{q}$ is manifestly real for photons emitted from the equatorial plane.

This relation may be used to determine the conserved quantity $\hat{\lambda}$ in terms of $(\hat{r}_s, g)$. Then, in principle, the geodesic equation (3.12) may be used to determine $\hat{q}$ also in terms of $(\hat{r}_s, g)$.

At the observer, the standard procedure involves defining impact parameters (α, β) in terms of $(\hat{\lambda}, \hat{q})$ for every geodesic hitting the observer's screen[76,98]:

$$\alpha = -\frac{\hat{\lambda}}{\sin\theta_o}, \qquad \beta = \pm\sqrt{\hat{\Theta}(\theta_o)}. \tag{3.16}$$

A bundle of nearby geodesics that reach the screen from the disk then subtends a solid angle given by

$$\mathrm{d}\Omega = \frac{1}{\hat{r}_o^2}\,\mathrm{d}\alpha\,\mathrm{d}\beta = \frac{1}{\hat{r}_o^2}\left|\frac{\partial(\alpha,\beta)}{\partial(\hat{\lambda},\hat{q})}\right|\mathrm{d}\hat{\lambda}\,\mathrm{d}\hat{q} = \frac{1}{\hat{r}_o^2}\left|\frac{\partial(\alpha,\beta)}{\partial(\hat{\lambda},\hat{q})}\right|\left|\frac{\partial(\hat{\lambda},\hat{q})}{\partial(\hat{r}_s,g)}\right|\mathrm{d}\hat{r}_s\,\mathrm{d}g. \tag{3.17}$$

The first Jacobian is straightforward to compute from Eq. (3.16):

$$\left|\frac{\partial(\alpha,\beta)}{\partial(\hat{\lambda},\hat{q})}\right| = \frac{\hat{q}}{\sin\theta_o\,|\beta|}. \tag{3.18}$$

On the other hand, the second Jacobian can typically only be computed numerically because no analytic expression relating $\hat{r}_s$, g, and $\hat{q}$ has been derived in the most general setting considered here.

Finally, the specific flux carried to the observer by the bundle of photons is given by

$$\mathrm{d}F_o = I_o\,\mathrm{d}\Omega = g^3 I_s\,\mathrm{d}\Omega, \tag{3.19}$$

where Liouville's theorem on the invariance of the phase space density of photons has been used to relate the observed specific intensity I_o to the emitted one I_s. We take the disk's specific intensity to be monochromatic at energy $E_\star$ (e.g., $E_{\text{FeK}\alpha} = 6.38\text{keV}$), and isotropic with surface emissivity $\mathcal{E}(\hat{r}_s)$:

$$I_s = \mathcal{E}(\hat{r}_s)\delta\left(E_s - E_\star\right) = g\mathcal{E}(\hat{r}_s)\delta\left(E_o - gE_\star\right). \tag{3.20}$$

Plugging this expression into Eq. (3.19) and using Eqs. (3.17)–(3.18), the dg integral corresponds to trivially setting $g = E_o/E_\star$, so we arrive at

$$F_o = \frac{g^4}{\hat{r}_o^2 \sin\theta_o} \int \frac{\hat{q}}{|\beta|} \left| \frac{\partial(\hat{\lambda}, \hat{q})}{\partial\left(\hat{r}_s, g\right)} \right| \mathcal{E}(\hat{r}_s)\, \mathrm{d}\hat{r}_s, \tag{3.21}$$

where we have absorbed a factor of $E_\star$ into $\mathcal{E}(r_s)$. Here, it is understood that the integral is to be evaluated over the radial extent of the accretion disk, typically starting from the ISCO. In the most general setting discussed so far, the result of the integral (3.21) will depend, via the surface emissivity $\mathcal{E}(\hat{r}_s)$, on the particular disk model (e.g., Novikov-Thorne) that one chooses to employ for describing the accretion of matter into the black hole.[‡]

In the next sections, we will consider the regime where the black hole has (near-)maximal spin and the emissions come from the innermost portion of the accretion disk lying near the ISCO. In this regime, we will find an analytic expression for the Jacobian $\partial(\hat{\lambda}, \hat{q})/\partial(\hat{r}_s, g)$ which will enable us to compute F_o analytically. Moreover, we will find that, up to an overall (possibly infinite) constant, the answer is entirely independent of the disk's surface emissivity and therefore universal.

[‡] In practice, a (broken) power law $\mathcal{E}(r_s) \propto r_s^{-p}$ is often implemented when fitting data, with the power(s) chosen to best fit the data (see e.g., Ref.[32]).

3.3 CRITICAL BEHAVIOR OF THE MAXIMALLY SPINNING EXTREME KERR

In this section, we specialize to the critical point of the Kerr family of metrics: the $J = M^2$ extreme Kerr. Small deviations from extremality are considered in the next section.

It is convenient to define shifted dimensionless radial coordinate and parameters[1,44]

$$r = \frac{\hat{r} - M}{M}, \qquad \lambda = 1 - \frac{\hat{\lambda}}{2M}, \qquad q^2 = 3 - \frac{\hat{q}^2}{M^2}, \tag{3.22}$$

in terms of which the geodesic equation (3.12) becomes

$$\int_{r_s}^{r_o} \frac{\mathrm{d}r}{\sqrt{R(r)}} = \int_{\theta_s}^{\theta_o} \frac{\mathrm{d}\theta}{\sqrt{\Theta(\theta)}}, \tag{3.23}$$

where

$$R(r) = r^4 + 4r^3 + \left(q^2 + 8\lambda - 4\lambda^2\right) r^2 + 8\lambda r + 4\lambda^2, \tag{3.24}$$

$$\Theta(\theta) = 3 - q^2 + \cos^2\theta - 4(1-\lambda)^2 \cot^2\theta. \tag{3.25}$$

When the source point r_s is near the horizon ($r_s \ll 1$) and the observation point r_o is far in the asymptotically flat region of the spacetime ($r_o \gg 1$), an analytical solution for the radial integral was recently found in Ref.[1]. In the same regime, an analytical expression for the polar integral was also recently obtained in Ref.[44]. The analysis in Refs.[1,44] shows that all electromagnetic signals from the near-horizon region $r_s \ll 1$ appear on the observer's screen on the NHEKline with coordinates

$$\begin{aligned} \alpha &= -2M \csc\theta_o, & (3.26) \\ \beta &= \pm M\sqrt{3 - q^2 + \cos^2\theta_o - 4\cot^2\theta_o}. & (3.27) \end{aligned}$$

Moreover, a key observation that may be derived semi-analytically from the results in Ref.[44] is that for a fixed redshift g, the dominant contribution to the flux measured from sources at r_s is achieved by photons emitted with conserved quantities (λ, q) such that r_s is a near-region radial turning point for the photon's geodesic. The near-region radial turning point is given by[1,44]

$$r_s = -\frac{2\lambda}{q^2}\left(2 + \sqrt{4 - q^2}\right). \tag{3.28}$$

On the other hand, for $r_s \ll 1$, we obtain from Eq. (3.15)

$$\lambda = -\frac{3r_s}{4g}\left(g - 1/\sqrt{3}\right). \tag{3.29}$$

The parameter ranges are $\lambda < 0$, $g \in (1/\sqrt{3}, \sqrt{3})$, and $q \in (0, \sqrt{3 + \cos^2\theta_o - 4\cot^2\theta_o})$. Note that Eqs. (3.28)–(3.29) imply that q depends only on g:

$$q = \frac{\sqrt{3}}{2g}\sqrt{\left(g - 1/\sqrt{3}\right)\left(5g + \sqrt{3}\right)}. \tag{3.30}$$

Given Eq. (3.26), this implies that β also depends only on g according to

$$\beta = \pm M\sqrt{3 + \cos^2\theta_o - 4\cot^2\theta_o - \frac{3}{4g^2}\left(g - 1/\sqrt{3}\right)\left(5g + \sqrt{3}\right)}, \tag{3.31}$$

meaning that the flux at different points on the observer's NHEKline is dominated by photons of different energy. From Eqs. (3.29)–(3.30), we may readily compute the Jacobian

$$\frac{\partial(\lambda, q)}{\partial(r_s, g)} = -\frac{3\sqrt{3}}{16qg^4}\left(g - 1/\sqrt{3}\right)\left(g + \sqrt{3}\right). \tag{3.32}$$

Using this in Eq. (3.21), we then find

$$F_o = \frac{3\sqrt{3}\left(g - 1/\sqrt{3}\right)\left(g + \sqrt{3}\right)}{8r_o^2 \sin\theta_o\, |\beta|} \int \mathcal{E}(r_s)\, \mathrm{d}r_s. \tag{3.33}$$

This remarkable equation is the main result of the chapter. Together with Eq. (3.31), it gives an explicit analytic formula for the observed flux F_o as a function of the redshift g [Eq. (3.1)], or equivalently, as a function of the elevation β on the NHEKline. We plot these functions in Figs. 3.1 and ??, respectively. The result is independent, up to an overall constant, of the particular disk model. The latter's role is merely to supply an emissivity function $\mathcal{E}$, whose integral fixes the overall scale of F_o. As we will see in Section 3.5, this overall scale might in fact be diverging at extremality.

It is worth emphasizing that the factorization of Eq. (3.21) into the form of Eq. (3.33) is consistent with expectations from conformal symmetry. Indeed, the $\mathsf{SL}(2, \mathbb{R})$ global conformal symmetry includes dilations and this implies that there are no special radii in the near-horizon part of the disk. As a result, one would expect that in the end the radial integration in Eq. (3.21) trivializes as manifested in Eq. (3.33).

3.4 NEAR-CRITICAL BEHAVIOR OF THE NEAR-EXTREME KERR

In this section, we consider a near-extremal black hole with a small deviation from extremality measured by a parameter $\epsilon \ll 1$ such that

$$a = M\sqrt{1-\epsilon^3}. \tag{3.34}$$

This choice of parametrization places the ISCO at an $\mathcal{O}\left(\epsilon\right)$ coordinate distance from the horizon:

$$r_{\text{ISCO}} = 2^{1/3}\epsilon + \mathcal{O}\left(\epsilon^2\right). \tag{3.35}$$

As has been previously observed in Ref.[65] for gravitational wave fluxes from extreme-mass-ratio inspirals, and in Ref.[44] for electromagnetic wave fluxes from an orbiting hot spot, the near-extreme result is often simply related to the extremal one by a natural identification of parameters. This is believed to be a manifestation of the action of the infinite-dimensional conformal group, which can relate extremal to near-extremal physics. Here the relevant identification of parameters is

$$r \to \epsilon r, \qquad \lambda \to \epsilon\lambda. \tag{3.36}$$

We have verified that with this identification, all the equations of the previous section concerning extreme Kerr are valid to leading order in ϵ for the near-extreme case as well. In particular, Eq. (3.33) gives the leading-order observed flux from the portion of the accretion disk that is located at an $\mathcal{O}\left(\epsilon\right)$ coordinate distance from the horizon of a near-extreme Kerr black hole, whose deviation from extremality is given by ϵ. Moreover, the flux from any other portion of the accretion disk that is at an $\mathcal{O}\left(\epsilon^p\right)$ coordinate distance from the horizon, with $0 < p < 3/2$, may be similarly obtained via the identification

$$r \to \epsilon^p r, \qquad \lambda \to \epsilon^p \lambda. \tag{3.37}$$

3.5 SYMMETRIC MODEL FOR A RADIANT DISK: A CONJECTURE

In the previous sections, we have seen that the profile of electromagnetic emissions from the innermost parts of an accretion disk surrounding a (near-)extremal Kerr is independent of the disk model, up to an overall constant that is given by the disk's integrated emissivity function $\mathcal{E}$. In this section, we motivate and propose a symmetric model for a homogeneous radiant disk. This symmetric disk model implies that the overall constant that multiplies the emission profile (3.1) diverges logarithmically as the black hole approaches extremality.

The source particle number current for an equatorial, stationary, axisymmetric disk that terminates at the ISCO takes the form

$$\mathcal{J}_s = \rho(\hat{r}_s) H(\hat{r} - \hat{r}_{\mathrm{ISCO}}) \delta\left(\theta - \pi/2\right) u_s, \tag{3.38}$$

where H is the Heaviside step function. We assume that this source current, which is completely fixed by the radial density profile of emitters in the disk, $\rho(\hat{r}_s)$, is conserved: $\nabla_\mu \mathcal{J}_s^\mu = 0$. We also assume that every particle emits isotropically, so that the local emissivity at the surface of the disk is $\mathcal{E}(\hat{r}_s) = \rho(\hat{r}_s)$.

Near extremality, the emergent conformal symmetry of the NHEK geometry includes dilations. To preserve this symmetry, we assume that the disk has a uniform particle number density per unit proper radial length. This completely fixes the surface emissivity to

$$\mathcal{E}(\hat{r}_s) = \frac{1}{u_s^t \hat{r}_s \sqrt{\Delta(\hat{r}_s)}} = \frac{\sqrt{\hat{r}_s^3 - 3M\hat{r}_s^2 + 2aM^{1/2}\hat{r}_s^{3/2}}}{\hat{r}_s \left(\hat{r}_s^{3/2} + aM^{1/2}\right) \sqrt{\hat{r}_s^2 - 2M\hat{r}_s + a^2}}. \tag{3.39}$$

Integrating this over radii r_s that scale like $r_s \sim \epsilon^p$ produces a logarithmically divergent constant

$$\int \mathcal{E}(r_s)\, \mathrm{d}r_s \sim \log \epsilon \tag{3.40}$$

that multiplies the profile (3.1). This is due to the logarithmic divergence of the disk's proper length at extremality.

In the terminology of Ref.[67], the choice of emissivity function (3.39) makes the source current (3.38) a vector field of weight $H = 0$ on Kerr. As a result, its leading piece in a near-horizon expansion is completely determined by the symmetries of NHEK. Any other choice of disk model that has a well-behaved near-horizon limit will also have a source current of weight $H = 0$ and therefore its leading behavior in the NHEK limit will match that of our symmetric model, with deviations arising only at subleading order (from near-horizon fields with larger conformal dimension). In particular, we expect the same logarithmic divergence (3.40) in the flux received from any slowly accreting disk with a well-behaved near-horizon limit.

3.6 SUMMARY

In this chapter, we studied high-spin black holes with a geometrically thin, stationary, axisymmetric, and equatorial disk of slowly accreting matter. Using geometric optics and building upon the method developed in Chapter 2, we obtained the flux due to emissions from the disk observed at infinity as a function of the photons' redshift, $F_o(g)$, given by 3.1.

This result holds independently of the disk model, which enters only through the proportionality constant, and is therefore universal. Our computation is directly relevant for the profile of FeKα line emissions. Hence, it could pertain to spectral observations by experiments such as XMM-Newton, Suzaku, and NuSTAR, which have revealed emissions from high-spin supermassive black holes centering the galaxies MCG-6-30-15 ($a \gtrsim 0.98M$), NGC 1365 ($a \gtrsim 0.97M$), and NGC 4051 ($a \gtrsim 0.99M$) among others[108–111].

Further, we proposed a model for a radiant disk that respects the symmetries of NHEK. Due to the logarithmic divergence of the disk's proper length at extremality, this model implies a logarithmically divergent overall proportionality constant in $F_o(g)$. Since the flux emerges on the NHEKline, it follows that, for a suitable source line, a high-resolution telescope might be able to observe the critical flux 3.1 as a characteristic brightness profile along the NHEKline.

4

Polarization Whorls

In this chapter, we predict the polarization profile of near-horizon emissions from high-spin black holes, in particular the black hole centering the galaxy Messier 87 (M87).

The Event Horizon Telescope (EHT) is preparing to deliver unprecedented up-close images of the supermassive black holes at the center of the Milky Way (Sagittarius A*) and M87[56]. It is expected to resolve the near-horizon regions of these black holes with a few dozen pixels at the horizon scale. This offers an opportunity for theorists to make predictions: What will the images look like?

The data collected by the EHT will provide a wealth of information about the electromagnetic emissions from the black hole's vicinity. The optical appearance of the black hole is determined by the intensity of the surrounding electromagnetic emissions, and has been the focus of intense investigation[39,51–55]. The EHT will also measure the polarization of the incident light, which is expected to carry important information about dynamics in the region surrounding the black hole[81–90]. The present work concerns this polarimetric image, which has received comparatively less attention.

The determination of the optical and polarimetric image of a generic black hole is an arduous task, as one must account for a multitude of complex astrophysical effects. This task is further complicated by the need to make numerous assumptions regarding the black hole's surroundings, such as the matter distribution and its radiative properties. As a result, analytic computation is in most cases completely infeasible. Instead, extensive numerical simulation is required in order to properly account for myriad physical ingredients. The proliferation of tunable parameters and model-dependent assumptions can make it difficult to extract physical predictions or intuition from numerics.

In the special case of high-spin black holes, however, certain features exhibit universal critical behavior that is independent of the detailed assumptions and parameters entering the model. This occurs because general relativity dictates that a rapidly spinning black hole develops an emergent conformal symmetry in its near-horizon region[43,98,99]. This conformal symmetry imposes strong constraints on fields and matter near the horizon with observable astrophysical consequences. Over the past several years, this symmetry has been exploited in order to analytically compute several otherwise intractable[*] astrophysically relevant processes[58,59,64,67,68,70,72,73,112–114].

To our great fortune, just such a high-spin black hole (likely within 2% of criticality[57]) centers the galaxy M87 and will soon be imaged by the EHT. The simplifying nature of the extremal limit allows us to perform our calculations analytically, and we obtain a striking polarimetric image of its near-horizon emissions. The polarization lines form a distinctive whorl that spirals into a central point inside the shadow, and the image lies entirely within the shadow and are not obscured by emissions from behind M87.

Our computations and predictions are valid for any high-spin black holes. We assume only that there is some physical process in the near-horizon region of the black hole capable of producing highly energetic photons and that it is invariant under the same emergent symmetries as the background geometry. The latter assumption is standard for the more familiar cases of axisymmetry and time-translation symmetry.

The rest of the chapter is organized as follows. In Section 4.1 we present the main result. In Section 4.2 we review the Kerr geometry and the geometric optics approximation. In Section 4.3 we outline our calculation of the polarimetric image. Finally we summarize the results Section 4.4. Various technical steps are relegated to the appendices.

---

[*] Numerical analyses are particularly problematic in this regime due to the critical behavior. Hence, the analytic and numeric approaches have complementary domains of applicability.

4.1 MAIN RESULT

We now present the main result of the chapter: the predictions for the polarimetric images of high-spin black holes, in particular M87 (Fig. 4.2).

Consider an observer located at a large distance $r_o \to \infty$ from an extreme black hole $\left(|J| = M^2\right)$, stationed at a fixed polar angle θ_o relative to the black hole's axis of symmetry. Photons emitted from the vicinity of the black hole impinge upon the screen of the observer, which we label with Cartesian coordinates (α_o, β_o) [Eqs. (4.27)].

A uniformly backlit black hole casts a shadow on the observer's screen [Eqs. (4.30)–(4.34)]. We find that near-horizon emissions are confined to appear within this shadow—that is, they cannot be obscured by bright sources located behind the black hole [App. 4.A3].

Photons impinging on the observer's screen register a polarization defined by the direction of oscillation of the transverse electric field. For the symmetric choice of source polarization, this direction is given by [Eqs. (4.29) & (4.79)]

$$\vec{\mathcal{E}} = \frac{1}{(\beta_o^2 + \gamma_o^2)} \left(\beta_o\beta_s + \gamma_o\gamma_s, \gamma_o\beta_s - \beta_o\gamma_s\right), \tag{4.1}$$

where the prefactor is fixed by the normalization condition $\vec{\mathcal{E}} \cdot \vec{\mathcal{E}} = 1$ (though its overall sign is irrelevant), and

$$\gamma_i = -(\alpha_i + M \sin\theta_i), \tag{4.2}$$

$$\alpha_s = \frac{\sin\theta_o}{\sin\theta_s}\alpha_o, \qquad \beta_s = (-1)^m \beta_o \sqrt{1 + \frac{\gamma_o^2 - \gamma_s^2}{\beta_o^2}}. \tag{4.3}$$

Here, M denotes the mass of the black hole and m the number of librations (angular turning points) of the geodesic connecting the source located at $(r_s \sim M, \theta_s)$ to the observer. Given a point (α_o, β_o) on the observer's screen, there is a single geodesic connecting it to a source point θ_s in the near-horizon region. Solving for this geodesic allows us to eliminate both θ_s and m from Eq. (4.1). This is described in detail in App. 4.A3, where we derive a formula [Eq. (4.126)] for θ_s as a function of the observer parameters by solving the geodesic equation.

Example plots of the polarimetric image (4.1) at $\theta_o = 0^\circ$ and $\theta_o = 90^\circ$ are depicted in Fig. 4.1. Both images display striking features. At $\theta_o = 0^\circ$, the integral curves, whose tangent field describes the direction of local linear polarization, assume a whorling pattern. They spiral outwards from the origin, which is an optical image of the north pole of the black hole, and reach an accumulation point at a circle corresponding to an image of the south pole. At this point, the number of angular turning points of the connecting geodesic jumps by one, and the integral curves spiral away from this circle towards a second concentric circle corresponding to a second image of the north pole. This pattern repeats indefinitely, with an infinite set of concentric circles demarcating an infinite number of coverings of the horizon of the black hole.

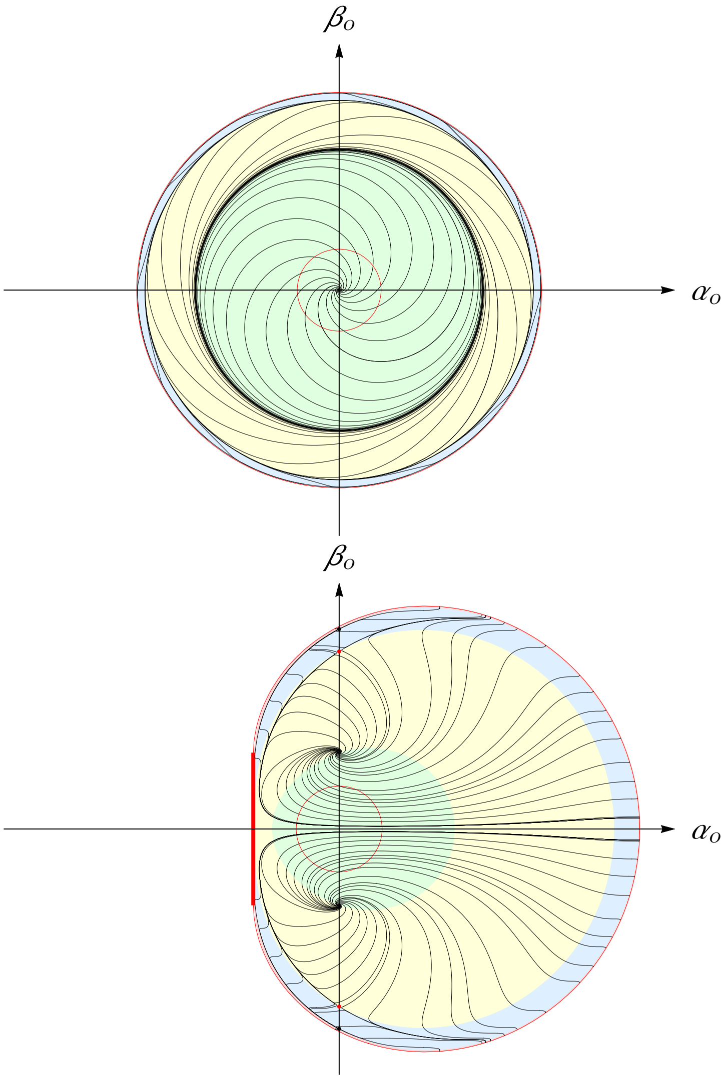

Figure 4.1: Polarimetric image observed by a face-on observer at the pole ($\theta_o = 0°$) and by an edge-on observer in the equatorial plane ($\theta_s = 90°$). The inner red circle is the locus $\alpha_o^2 + \beta_o^2 = M^2$, corresponding to the location of the event horizon, while the outer red contour is the edge of the shadow. The black hole's spin is counterclockwise about the origin in the top image, and right-handed about the β_o-axis in the bottom image. The top image, which is circularly symmetric in accordance with the axisymmetry of the Kerr black hole, depicts a swirling pattern around the pole that resembles a hair whorl. The bottom image, which is reflection symmetric in accordance with the equatorial symmetry of the Kerr black hole, contains two whorls because gravity bends light from both the northern and southern poles back towards the observer. The colors indicate the number m of angular turning points of the geodesic connecting the source to the observer: $m = 0$ (direct) light appears in the green region, while the yellow, blue, and red regions correspond to relativistic images with $m = 1, 2$, and 3, respectively. There are infinitely many more regions (which correspond to geodesics with diverging m) bunched up near the edge of the shadow (which corresponds to the photon orbit) but their area rapidly decreases with m and they become indiscernible past $m > 3$.

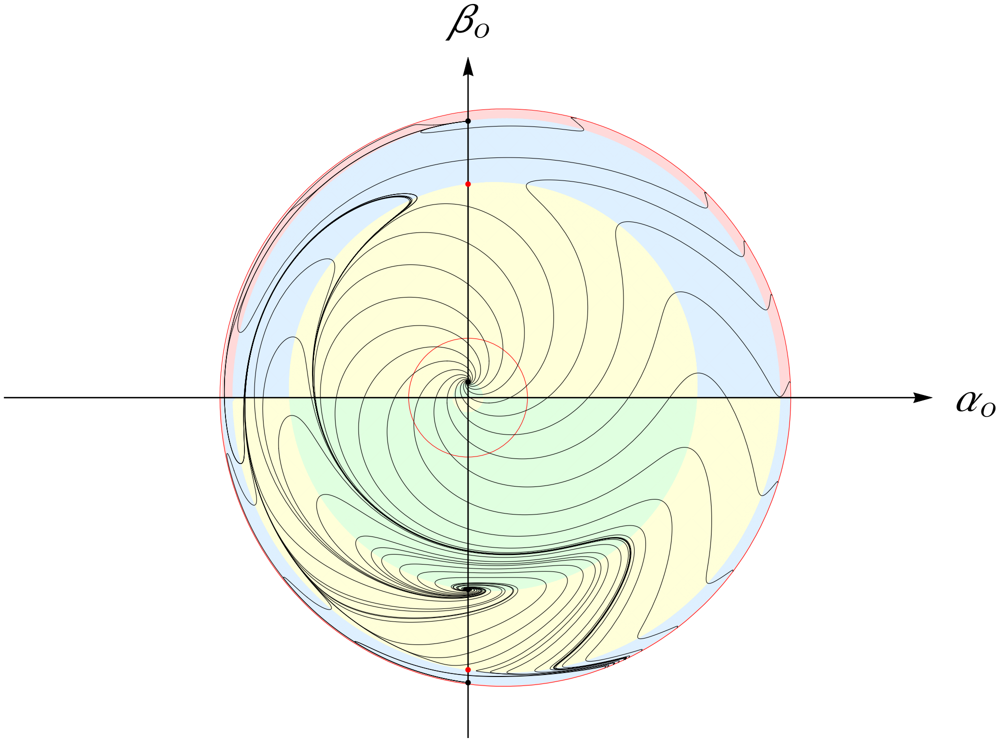

Figure 4.2: Prediction for the polarimetric image of the black hole at the center of M87 as seen at the EHT ($\theta_o = 15°$). Regions of different m are colored according to the same conventions as in Fig. 4.1. Small dots along the vertical axis indicate the apparent locations of the poles.

The image seen by an edge-on observer ($\theta_o = 90^\circ$) is less symmetric, although the qualitative features found in the face-on ($\theta_o = 0^\circ$) case remain. The integral curves of the local polarization whorl around special points on the $\alpha_o = 0$ axis corresponding to images of the north and south poles. Domain walls corresponding to local extrema of the map $\theta_s(\alpha_o, \beta_o)$ control the pattern farther away from the origin, and accumulate near the shadow of the black hole.

In Fig. 4.2, we plot the corresponding polarimetric image for an observer situated 15° off-axis, which is the angle relevant for observations of the black hole at the center of the galaxy M87. This generic image is more complicated than the special cases considered in Fig. 4.1, although it retains a (distorted) distinctive whorl-like pattern that could serve as a diagnostic for a high-spin black hole.

4.2 PROPAGATION OF LIGHT AND ITS POLARIZATION AROUND A BLACK HOLE

In this section, we review the standard treatment of the propagation of light and its polarization in the background of a rotating black hole[91]. We follow the conventions of Ref.[115].

4.2.1 KERR GEOMETRY

The Kerr metric describes astrophysically realistic rotating black holes of mass M and angular momentum $J = aM$. In Boyer-Lindquist coordinates (t, r, θ, ϕ), the Kerr line element is

$$ds^2 = -\frac{\Delta}{\Sigma}\left(\mathrm{d}t - a\sin^2\theta\,\mathrm{d}\phi\right)^2 + \frac{\Sigma}{\Delta}\,\mathrm{d}r^2 + \Sigma\,\mathrm{d}\theta^2 + \frac{\sin^2\theta}{\Sigma}\left[\left(r^2 + a^2\right)\mathrm{d}\phi - a\,\mathrm{d}t\right]^2, \quad (4.4)$$

where

$$\Delta(r) = r^2 - 2Mr + a^2, \qquad \Sigma(r,\theta) = r^2 + a^2\cos^2\theta. \tag{4.5}$$

This metric admits two Killing vectors ∂_t and ∂_ϕ generating time-translation symmetry and axisymmetry, respectively. In addition to these isometries, the Kerr metric also admits the existence of an irreducible symmetric Killing tensor[†]

$$K_{\mu\nu} = -J_\mu{}^\lambda J_{\lambda\nu}, \tag{4.6}$$

where

$$J = a\cos\theta\,\mathrm{d}r \wedge \left(\mathrm{d}t - a\sin^2\theta\,\mathrm{d}\phi\right) - r\sin\theta\,\mathrm{d}\theta \wedge \left[a\,\mathrm{d}t - \left(r^2 + a^2\right)\mathrm{d}\phi\right]. \tag{4.7}$$

Many special properties of the Kerr geometry arise from the existence of a special complex null

---

[†] A Killing tensor satisfies $\nabla_{(\lambda}K_{\mu\nu)} = 0$. The antisymmetric tensor $J_{\mu\nu} = -J_{\nu\mu}$ satisfies the Killing-Yano equation $\nabla_{(\lambda}J_{\mu)\nu} = 0$.

tetrad $\{l, n, m, \bar{m}\}$, where $\{l, n\}$ is a pair of real null vectors and m is a complex null vector such that

$$\begin{aligned} l \cdot l = n \cdot n = m \cdot m = \bar{m} \cdot \bar{m} &= 0, & (4.8) \\ l \cdot m = l \cdot \bar{m} = n \cdot m = n \cdot \bar{m} &= 0, & (4.9) \\ l \cdot n &= -1, & (4.10) \\ m \cdot \bar{m} &= 1, & (4.11) \end{aligned}$$

and

$$g_{\mu\nu} = 2\left(m_{(\mu}\bar{m}_{\nu)} - l_{(\mu}n_{\nu)}\right). \tag{4.12}$$

A possible choice of null tetrad obeying all these conditions in Kerr is[‡]

$$\begin{aligned} l &= \frac{1}{\sqrt{2\Delta\Sigma}}\left[\left(r^2+a^2\right)\partial_t + \Delta\,\partial_r + a\,\partial_\phi\right], & (4.13) \\ n &= \frac{1}{\sqrt{2\Delta\Sigma}}\left[\left(r^2+a^2\right)\partial_t - \Delta\,\partial_r + a\,\partial_\phi\right], & (4.14) \\ m &= \frac{1}{\sqrt{2}(r+ia\cos\theta)}\left(ia\sin\theta\,\partial_t + \partial_\theta + \frac{i}{\sin\theta}\,\partial_\phi\right). & (4.15) \end{aligned}$$

Under the geometric optics approximation, photons propagate along null geodesics. In the Kerr geometry (4.4), this implies that a photon passing through a point x^μ in the spacetime has a four-

---

[‡] This choice is not unique: for instance, the conditions (4.8) are invariant under rescalings $(l, n) \to \left(F^{-1}l, Fn\right)$ for any scalar function F. The standard choice for Kerr is the Kinnersley tetrad $\{l', n', m, \bar{m}\}$, where $(l', n') = \left(F^{-1}l, nF\right)$ with $F = \sqrt{\Delta/2\Sigma}$ (see, *e.g.*: Ref.[91]). We have performed this rescaling in order to ensure that the tetrad (4.13) has the simple near-horizon limit (4.46).

momentum $p = p_\mu \, \mathrm{d}x^\mu$ of the form

$$p(x^\mu, \omega, \ell, k) = -\omega \, \mathrm{d}t \pm_r \frac{\sqrt{\mathcal{R}(r)}}{\Delta(r)} \, \mathrm{d}r \pm_\theta \sqrt{\Theta(\theta)} \, \mathrm{d}\theta + \ell \, \mathrm{d}\phi, \tag{4.16}$$

where the two choices of sign $\pm_r$ and $\pm_\theta$ determine the radial and polar directions of travel, respectively. Here, we also introduced radial and polar potentials

$$\begin{aligned} \mathcal{R}(r) &= \left[\omega\left(r^2 + a^2\right) - a\ell\right]^2 - k\Delta(r), && (4.17) \\ \Theta(\theta) &= k - \left(\ell \csc\theta - a\omega \sin\theta\right)^2, && (4.18) \end{aligned}$$

with (ω, ℓ, k) denoting the photon's energy, component of angular momentum parallel to the axis of symmetry, and Carter constant, respectively:[§]

$$\begin{aligned} \omega &= -p_t, && (4.19) \\ \ell &= p_\phi, && (4.20) \\ k &= K^{\mu\nu} p_\mu p_\nu = p_\theta^2 + 2ap_tp_\phi + a^2p_t^2 \sin^2\theta + p_\phi^2 \csc^2\theta. && (4.21) \end{aligned}$$

[§] The Carter constant k and Carter integral $Q = p_\theta^2 - \cos^2\theta \left(a^2p_t^2 - p_\phi^2 \csc^2\theta\right)$ are related by $k = Q + (\ell - a\omega)^2$.

These quantities are conserved along the photon's trajectory, as is the Penrose-Walker constant[¶]

$$\begin{aligned}\kappa &= 2p^\mu f^\nu \left(l_{[\mu}n_{\nu]} - m_{[\mu}\bar{m}_{\nu]}\right)(r - ia\cos\theta) \\ &= 2\left[(p \cdot l)\,(f \cdot n) - (p \cdot m)\,(f \cdot \bar{m})\right](r - ia\cos\theta)\,,\end{aligned} \tag{4.22}$$

provided that the vector f is orthogonal to p and parallel transported along it,

$$f \cdot p = 0, \qquad p^\mu \nabla_\mu f^\nu = 0. \tag{4.23}$$

When f is a unit-norm spacelike vector, $f \cdot f = 1$, we may interpret it as the photon's linear polarization. Its parallel transport is then determined by the conservation of the Penrose-Walker constant (4.22), which is typically rewritten as

$$\kappa = (A - iB)(r - ia\cos\theta) \equiv \kappa_1 + i\kappa_2, \tag{4.24}$$

where

$$A = (p \cdot l)(f \cdot n) - (p \cdot n)(f \cdot l), \tag{4.25}$$

$$iB = (p \cdot m)(f \cdot \bar{m}) - (p \cdot \bar{m})(f \cdot m). \tag{4.26}$$

[¶] The last step follows from the identity (4.12). The conserved quantity κ is associated with the existence of a conformal Killing spinor, which every Petrov D spacetime admits. For the Kerr spacetime, one can show that $|\kappa|^2 = \kappa_1^2 + \kappa_2^2 = k\,(f \cdot f)$.

When a photon of momentum (4.16) impinges upon the screen of a distant observer at polar angle θ_o, it appears at Cartesian coordinates (α_o, β_o) on the observer's screen given by[44,76,98]

$$\alpha_o = -\frac{\ell}{\omega \sin\theta_o}, \qquad \beta_o = \pm_o \frac{\sqrt{\Theta(\theta_o)}}{\omega}, \tag{4.27}$$

where the sign $\pm_o$ is equal to that of p_θ at the observer. With

$$\gamma_o = -(\alpha_o + a \sin\theta_o), \tag{4.28}$$

the observed linear polarization of the photon (or equivalently, the direction of the electromagnetic wave's electric field) is given by a vector with Cartesian components on the screen

$$\vec{\mathcal{E}} = (\mathcal{E}_\alpha, \mathcal{E}_\beta) = \frac{1}{(\beta_o^2 + \gamma_o^2)} \left(\beta_o \kappa_1 + \gamma_o \kappa_2, \gamma_o \kappa_1 - \beta_o \kappa_2\right), \tag{4.29}$$

which has unit norm because $\kappa_1^2 + \kappa_2^2 = \omega^2 \left(\beta_o^2 + \gamma_o^2\right) = k$. The overall sign is irrelevant.

A backlit black hole casts a shadow on the observer's screen. Provided $0 < a < M$, the contour of the shadow is traced by the curve $(\alpha(\tau), \beta(\tau))$ where

$$\begin{aligned} \alpha(\tau) &= \frac{\tau^2 (\tau - 3M) + a^2 (\tau + M)}{a (\tau - M) \sin\theta_o}, && (4.30) \\ \beta(\tau) &= \pm_o \sqrt{a^2 \cos^2\theta_o - \frac{\tau^3 [\tau (\tau - 3M)^2 - 4a^2 M] + [\tau^2 (\tau - 3M) + a^2 (\tau + M)]^2 \cot^2\theta_o}{a^2 (\tau - M)^2}}, && (4.31) \end{aligned}$$

where

$$\tau \in [\tau_-, \tau_+] , \qquad \tau_\pm \equiv 2M \left[1 + \cos\left(\frac{2}{3} \arccos \pm \frac{a}{M} \right) \right] . \tag{4.32}$$

The extremal regime $a \to M$ is subtle[44]. In that limit, the shadow develops a vertical edge at[‖]

$$\alpha = -2M \csc\theta_o, \qquad |\beta| < M\sqrt{3 + \cos^2\theta_o - 4\cot^2\theta_o}, \tag{4.33}$$

with the remainder of the contour given by the curve

$$M\alpha\,(\tau) \;=\; \left(\tau^2 - M^2 - 2M\tau\right)\csc\theta_o, \tag{4.34}$$

$$M\beta\,(\tau) \;=\; \pm_o\sqrt{\tau^3\,(4M-\tau) + M^4\cos^2\theta_o - \left(\tau^2 - M^2 - 2M\tau\right)^2\cot^2\theta_o}, \tag{4.35}$$

where $\tau \in (M, 4M)$.

4.2.2 NHEK GEOMETRY

When the angular momentum of a rotating black hole nears saturation of the Kerr bound $|J| \le M^2$, the region of spacetime in the vicinity of its event horizon develops a region of divergent proper depth[21]. To resolve physics in this near-horizon region, one can introduce Bardeen-Horowitz coordi-

---

[‖] This vertical edge is visible to observers in the range $\theta_o \in [\theta_c, \pi - \theta_c]$ but disappears above the critical angle $\theta_c = \arctan\,(4/3)^{1/4} \approx 47^\circ$, which is why it only appears in the depiction of the edge-on case in Figs. 4.1 and 4.2.

nates

$$t = \frac{2M}{\epsilon^p} T, \qquad r = M(1 + \epsilon^p R), \qquad \phi = \Phi + \frac{T}{\epsilon^p}, \tag{4.36}$$

and then zoom into the horizon by taking the scaling limit $\epsilon \to 0$, with either

$$\text{Extremal limit}: \qquad a = M, \ p = 1, \tag{4.37}$$

$$\text{Near-extremal limit}: \qquad a = M\sqrt{1 - \epsilon^2}, \ 0 < p < 1. \tag{4.38}$$

Applying this procedure to the Kerr metric (4.4) produces the Near-Horizon Extreme Kerr (NHEK) line element[43]

$$d\hat{s}^2 = 2M^2\Gamma \left[-R^2 \, \mathrm{d}T^2 + \frac{\mathrm{d}R^2}{R^2} + \mathrm{d}\theta^2 + \Lambda^2 \left(\mathrm{d}\Phi + R \, \mathrm{d}T \right)^2 \right], \tag{4.39}$$

where

$$\Gamma(\theta) = \frac{1 + \cos^2\theta}{2}, \qquad \Lambda(\theta) = \frac{2\sin\theta}{1 + \cos^2\theta}, \tag{4.40}$$

which forms a spacetime solution to Einstein's equations in its own right. From now on, we denote contractions with respect to this hatted metric by $\circ$ and reserve $\cdot$ for contractions in Kerr.

In the remainder of this chapter, we will study electromagnetic emissions from the near-horizon region described by the NHEK geometry (4.39). For simplicity, we will restrict our attention to the case of a precisely extremal black hole with $a = M$ and use the scaling limit (4.37). However, we expect the polarimetric images we obtained to be identical to leading order in ϵ in the scaling limit (4.38) relevant for the physically realistic case of a near-extremal black hole such as M87. Moreover, as subleading corrections are power-suppressed in ϵ, we expect this leading-order result to be an excellent approximation for M87 ($\epsilon < 0.2$).

The NHEK geometry has an enlarged $\mathsf{SL}(2,\mathbb{R}) \times \mathsf{U}(1)$ isometry group generated by the four Killing vector fields

$$\begin{aligned} W_0 &= \partial_\Phi, && (4.41) \\ H_+ &= \partial_T, && (4.42) \\ H_0 &= T\,\partial_T - R\,\partial_R, && (4.43) \\ H_- &= \left(T^2 + \frac{1}{R^2}\right)\partial_T - 2TR\,\partial_R - \frac{2}{R}\,\partial_\Phi, && (4.44) \end{aligned}$$

thanks to an enhancement of the time translation symmetry H_+ to an $\mathsf{SL}(2,\mathbb{R})$ global conformal symmetry that also includes dilations H_0 and special conformal transformations H_-.

In the near-horizon limit, the irreducible Killing tensor (4.6) in Kerr becomes a reducible Killing tensor in NHEK that is given (up to a mass term) by the Casimir of $\mathsf{SL}(2,\mathbb{R}) \times \mathsf{U}(1)$,

$$\hat{K}^{\mu\nu} = M^2\hat{g}^{\mu\nu} - H_0^\mu H_0^\nu + \frac{1}{2}\left(H_+^\mu H_-^\nu + H_-^\mu H_+^\nu\right) + W_0^\mu W_0^\nu. \tag{4.45}$$

Meanwhile, the extreme Kerr tetrad (4.13) descends to the NHEK tetrad

$$\hat{l} = \frac{1}{2M\sqrt{\Gamma}}\left(\frac{1}{R}\,\partial_T + R\,\partial_R - \partial_\Phi\right), \tag{4.46}$$

$$\hat{n} = \frac{1}{2M\sqrt{\Gamma}}\left(\frac{1}{R}\,\partial_T - R\,\partial_R - \partial_\Phi\right), \tag{4.47}$$

$$\hat{m} = \frac{1}{\sqrt{2}M}\left(\frac{1}{1+i\cos\theta}\,\partial_\theta + \frac{\cos\theta + i}{2\sin\theta}\,\partial_\Phi\right), \tag{4.48}$$

which also satisfies the null tetrad conditions (4.8) with respect to the NHEK metric (4.39).

Under the geometric optics approximation, a photon passing through a point X^μ in the NHEK geometry (4.39) has a four-momentum $P = P_\mu\,\mathrm{d}X^\mu$ of the form

$$P(X^\mu, E, L, K) = -E\,\mathrm{d}T \pm_r \frac{\sqrt{(E+LR)^2 - KR^2}}{R^2}\,\mathrm{d}R \pm_\theta \sqrt{K - \frac{L^2}{\Lambda^2}}\,\mathrm{d}\theta + L\,\mathrm{d}\Phi, \tag{4.49}$$

where the signs determine the direction of travel, and (E, L, K) denote the photon's near-horizon energy (with respect to NHEK time), component of angular momentum parallel to the axis of symmetry, and Carter constant, respectively:[**]

$$E = -P_T, \tag{4.50}$$

$$L = P_\Phi, \tag{4.51}$$

$$K = \hat{K}^{\mu\nu}P_\mu P_\nu = \left(1 - \frac{1}{2\Gamma}\right)\left[\left(P_\Phi - \frac{P_T}{R}\right)^2 - P_R^2 R^2\right] + \frac{1}{2\Gamma}\left(P_\Theta^2 + \frac{P_\Phi^2}{\Lambda^2}\right). \tag{4.52}$$

[**] Observe that $K - L^2 = -h_0^2 + \frac{1}{2}(h_+h_- + h_-h_+)$, where $h_i = H_i^\mu u_\mu$ are the conserved quantities associated with the generators of $\mathsf{SL}(2,\mathbb{R})$. Since these are not independent of each other, we use the $\mathsf{SL}(2,\mathbb{R})$ Casimir $K - L^2$, which is in involution with all the h_i[100]. This is exactly analogous to exploiting the conservation of J_z and J^2, rather than (J_x, J_y, J_z), in a problem with $\mathsf{SO}(3)$ symmetry.

These quantities are conserved along the photon's trajectory, as is the Penrose-Walker constant[††]

$$\mathcal{K} = M\,(\mathcal{A} - i\mathcal{B})\,(1 - i\cos\theta), \tag{4.53}$$

where

$$\begin{aligned} \mathcal{A} &= (P \circ \hat{l})(F \circ \hat{n}) - (P \circ \hat{n})(F \circ \hat{l}), && (4.54) \\ i\mathcal{B} &= (P \circ \hat{m})(F \circ \bar{\hat{m}}) - (P \circ \bar{\hat{m}})(F \circ \hat{m}), && (4.55) \end{aligned}$$

provided that the vector F is orthogonal to P and parallel transported along it,

$$F \circ P = 0, \qquad P^\mu \hat{\nabla}_\mu F^\nu = 0. \tag{4.56}$$

As in Kerr, when the vector F is a unit-norm spacelike vector, $F \circ F = 1$, we may interpret it as the photon's linear polarization. Its parallel transport is then determined by the conservation of the Penrose-Walker constant (4.53).

[††] Note that $M(1 - i\cos\theta)$ is the near-horizon limit (4.36) of its Kerr analogue $r - ia\cos\theta$. Up to some factors of M, these are the Weyl tensor components Ψ_2 (in the Newman-Penrose formalism) of NHEK and Kerr, respectively.

In the geometric optics approximation, a thin beam of photons is modeled by a narrow bundle of rays. Together, these rays form a null geodesic congruence. If we give each photon in the beam the same energy, then we can uniquely fix the vector field tangent to the congruence by setting it equal, at every point x^μ within the beam, to the momentum $p(x^\mu)$ of the photon passing through that point. For a light beam in Kerr, this results in the vector field (4.16).

Additionally, we can also define a polarization vector field $f(x^\mu)$ at every point within the light beam. This spacelike vector field must have unit norm and be everywhere orthogonal to $p(x^\mu)$, the generator of the null congruence. Thus, a beam of radiation, which is completely characterized by its intensity and polarization, can be described by two vector fields p and f obeying the null geodesic and parallel transport equations[‡‡]

$$p^\mu \nabla_\mu p^\nu = p^\mu \nabla_\mu f^\nu = 0, \qquad p \cdot p = p \cdot f = 0, \qquad f \cdot f = 1. \tag{4.57}$$

Next, suppose that we shine such a beam of radiation out of (or into) the near-horizon region of an extreme Kerr black hole. The NHEK portion of the beam is then described by a momentum $P(X^\mu)$ and polarization $F(X^\mu)$ obeying the NHEK analogues of Eqs. (4.57),

$$P^\mu \hat{\nabla}_\mu P^\nu = P^\mu \hat{\nabla}_\mu F^\nu = 0, \qquad P \circ P = P \circ F = 0, \qquad F \circ F = 1. \tag{4.58}$$

[‡‡] In general, f is a complex vector field subject to the normalization condition $f \cdot \bar{f} = 1$. Here, we assume the light is linearly polarized light, in which case f is real and $f \cdot f = 1$.

However, the converse is not true: not all NHEK vector fields $P(X^\mu)$ and $F(X^\mu)$ solving these equations describe beams of radiation that escape the NHEK region and connect to a distant observer. Those that do have to obey an additional constraint: they must arise as the near-horizon limits of corresponding Kerr vector fields $p(x^\mu)$ and $f(x^\mu)$. As we will now show, this requirement imposes additional symmetry constraints on $P(X^\mu)$ and $F(X^\mu)$. This is a specific instance of a more general phenomenon: the near-horizon limit of a field in extreme Kerr acquires a definite scaling weight under NHEK dilations[67]. Further details are presented in App. 4.A1.

4.3.1 Generic photons

Rotating black holes exhibit a surprising phenomenon known as superradiance: they can amplify the energy of an object scattered off the horizon, as long as its incident energy does not exceed the so-called superradiant bound

$$\omega - \Omega_H \ell \leq 0, \tag{4.59}$$

where Ω_H denotes the angular frequency of the event horizon. For an extremal black hole, $\Omega_H = 1/(2M)$, and we refer to photons not saturating the superradiant bound ($\omega \neq \Omega_H \ell$) as generic.

In the near-horizon limit (4.36), the Kerr four-momentum (4.16) of a generic photon entering the

NHEK region is

$$\begin{aligned} p(x^\mu, \omega, \ell, k) &= -\tfrac{2M\omega-\ell}{\epsilon}\, \mathrm{d}\left(T \pm_r \tfrac{1}{R}\right) + \mathcal{O}\left(\epsilon^0\right) \\ &= P\left(X^\mu, \tfrac{2M\omega-\ell}{\epsilon}, 0, 0\right) + \mathcal{O}\left(\epsilon^0\right), \end{aligned} \tag{4.60}$$

where the second line follows by comparison with the four-momentum (4.49) of a NHEK photon. Hence, the conserved quantities (ω, ℓ, k) along the photon's trajectory in Kerr are related to their NHEK analogues (E, L, K) by

$$\omega - \Omega_H \ell = \frac{\epsilon E}{2M}, \qquad L = 0, \qquad K = 0, \tag{4.61}$$

in accordance with Eqs. (4.83) with $H = 1$. Note that this relation reflects the high energy cost incurred by near-horizon photons that climb out of NHEK: an outgoing photon undergoes a parametrically large redshift as it escapes from the parametrically deep gravitational well of the black hole. Conversely, from the perspective of an observer lying at a Boyer-Lindquist radius of order ϵ from the horizon, an infalling particle with $\omega - \Omega_H \ell \neq 0$ in Kerr must necessarily have a NHEK energy that diverges as the observer is pushed deeper into NHEK ($E \to \infty$ as $\epsilon \to 0$). For this reason, NHEK is naturally a site of high-energy collisions that can supply the highly energetic photons needed for our signal[67,116].

Moreover, note that under a NHEK dilation $(T,R)\to(T',R')=(T/\epsilon,\epsilon R)$,

$$\begin{aligned} P(X^\mu,E,0,0) &= -E\,\mathrm{d}\left(T\pm_r\frac{1}{R}\right) && (4.62)\\ \longrightarrow\ P(X'^\mu,E,0,0) &= -\frac{E}{\epsilon}\,\mathrm{d}\left(T\pm_r\frac{1}{R}\right)=\frac{1}{\epsilon}P(X^\mu,E,0,0). && (4.63)\end{aligned}$$

Infinitesimally, this imposes a symmetry condition on a narrow bundle of rays surrounding the photon,

$$\mathcal{L}_{H_0}P(X^\mu,E,0,0)=P(X^\mu,E,0,0), \tag{4.64}$$

in agreement with Eq. (4.85) with $H=1$. This proves that a generic beam of photons in Kerr enters (or leaves) the near-horizon region along a null geodesic congruence with the largest allowed weight. (We show that $H\leq 1$ in App. 4.A1.)

In fact, we can make a stronger statement: any generic beam of photons entering (or leaving) the near-horizon region must do so along a principal null congruence (PNC) of the NHEK geometry. There are two such congruences: the ingoing one generated by $\hat{n}$ and the outgoing one generated by $\hat{l}$, where $(\hat{l},\hat{n})$ are the real vectors in the NHEK tetrad (4.46). Indeed, note that

$$\begin{aligned} &\text{Outgoing PNC }(\pm_r=1): && P(X^\mu,E,0,0)=-E\,\mathrm{d}\left(T+\frac{1}{R}\right)=\frac{E}{MR\sqrt{\Gamma}}\hat{l}, && (4.65)\\ &\text{Ingoing PNC }(\pm_r=-1): && P(X^\mu,E,0,0)=-E\,\mathrm{d}\left(T-\frac{1}{R}\right)=\frac{E}{MR\sqrt{\Gamma}}\hat{n}. && (4.66)\end{aligned}$$

4.3.2 Photons at the superradiant bound

Notice that if we fine-tune the Kerr photon to be at the superradiant bound $\omega = \Omega_H \ell$, then $2M\omega - \ell = 0$ and as such, the leading term in the expansion (4.60) vanishes. Note that the limits $\ell \to 2M\omega$ and $\epsilon \to 0$ do not commute. In order to ensure that the superradiant photons solve the NHEK geodesic equation, the limit $\ell \to 2M\omega$ must be taken first. Hence, the expansion starts at the next order, with

$$\begin{aligned} p(x^\mu, \omega, \ell, k) &= \pm_r \frac{\sqrt{\ell^2 - k}}{R}\, \mathrm{d}R \pm_\theta \sqrt{k - \frac{\ell^2}{\Lambda^2}}\, \mathrm{d}\theta + \ell\, \mathrm{d}\Phi + \mathcal{O}(\epsilon) \\ &= P(X^\mu, 0, \ell, k) + \mathcal{O}(\epsilon)\,, \end{aligned} \tag{4.67}$$

where the second line follows by comparison with the four-momentum (4.49) of a NHEK photon. Hence, the conserved quantities (ω, ℓ, k) along the photon's trajectory in Kerr are related to their NHEK analogues (E, L, K) by

$$\omega - \Omega_H \ell = \frac{E}{2M} = 0, \qquad \ell = L, \qquad k = K, \tag{4.68}$$

in accordance with Eqs. (4.83) with $H = 0$. Moreover, note that under a NHEK dilation $(T, R) \to (T', R') = (T/\epsilon, \epsilon R)$,

$$\begin{aligned} P(X^\mu, 0, L, K) &= \pm_r \frac{\sqrt{L^2 - K}}{R}\,\mathrm{d}R \pm_\theta \sqrt{K - \frac{L^2}{\Lambda^2}}\,\mathrm{d}\theta + L\,\mathrm{d}\Phi \\ \longrightarrow P(X'^\mu, 0, L, K) &= P(X^\mu, 0, L, K). \end{aligned} \tag{4.69}$$

Infinitesimally, this imposes a symmetry condition on a narrow bundle of rays surrounding the photon,

$$\mathcal{L}_{H_0} P(X^\mu, 0, L, K) = 0, \tag{4.70}$$

in agreement with Eq. (4.85) with $H = 0$. Although such null geodesic congruences may appear mathematically fine-tuned, they are abundantly realized in nature as the photon beams emitted by an orbiting hot spot or the near-horizon portion of a slowly accreting disk[2,44].

4.3.3 Symmetric source polarization

We now imagine that every point in the near-horizon region of an extreme Kerr black hole emits beams of radiation in every direction with some (possibly vanishing) intensity. Thus, at every point X^μ, we could have photons emitted with any momentum $P(X^\mu, E, L, K)$ and corresponding polarization $F(X^\mu, E, L, K)$. From the preceding discussion, we know that such light beams may escape to the asymptotically flat region with two qualitatively different behaviors:

1). Photons in the beam have NHEK four-momentum $P(X^\mu, E/\epsilon, 0, 0)$ aligned with the outgoing PNC [Eq. (4.65)]. They have vanishing NHEK angular momentum and Carter constant ($L = K = 0$), but parametrically large NHEK energy ($E \sim 1/\epsilon$). They reach the far region as generic $H = 1$ photons with finite energy above extremality $\omega - \Omega_H \ell = \epsilon E/2M \neq 0$ and arbitrary Kerr Carter constant k [Eqs. (4.61)]. They can appear anywhere within the shadow of the black hole.

2). Photons in the beam have NHEK four-momentum $P(X^\mu, 0, L, K)$ [Eq. (4.67)] and vanishing NHEK energy ($E = 0$). They reach the far region as $H = 0$ photons at the superradiant bound $\omega = \Omega_H \ell$ with Kerr angular momentum and Carter constant given by $\ell = L$ and $k = K$ [Eqs. (4.68)]. (Note that this is true for $H = 0$ photons. We neglect the measure-zero set of photons with $H < 0$, which may only come out with $\omega = \ell = k = 0$.) They can only appear on the vertical edge of the black hole's shadow (the NHEKline).

In both cases, the near-horizon polarization must necessarily obey Eqs. (4.58) and (4.85),

$$P^\mu \hat{\nabla}_\mu F^\nu = 0, \qquad P \circ F = 0, \qquad F \circ F = 1, \qquad \mathcal{L}_{H_0} F = 0. \tag{4.71}$$

This last dilation-invariance condition is derived in App. (4.A1) from properties of the near-horizon limit (4.36). It is one of the additional symmetry constraints alluded to below Eqs. (4.58).

A spacetime tends to impart its symmetries to the physics it drives. For instance, since accretion onto a black hole is a gravitational process, we expect accretion disks to inherit the stationarity and axisymmetry of the Kerr metric (4.4)—this standard assumption is largely borne out by numerical simulations (at least in the slow accretion regime). By this reasoning, we may also expect that the physical processes responsible for electromagnetic emissions from NHEK (whatever they are) respect the symmetries of the spacetime. Thus, we make the natural assumption that

$$\mathcal{L}_{W_0} F = \mathcal{L}_{H_\pm} F = 0. \tag{4.72}$$

That is, we suppose that the near-horizon source configuration produces radiation possessing the same symmetries as the NHEK geometry (4.39): stationarity, axisymmetry, dilation invariance, and special-conformal symmetry. This will be our only physical assumption and it will lead us to a clear signature. It would be interesting to find an example of a physical mechanism that would produce such a polarization profile at the source—in the interim, we simply note that traditional simulations also appear to predict a whorl-like pattern in certain regimes[85–87,90].

For $H = 1$ photons with four-momentum (4.60), we find that there is a unique choice (up to an irrelevant overall sign) of source polarization in NHEK obeying Eqs. (4.71) together with the symmetry-based assumption (4.72):

$$F = \frac{1}{2M\Gamma}\left(\mp_r \partial_\theta + \frac{\cos\theta}{\Lambda}\partial_\Phi\right) = \frac{1}{\sqrt{2}}\left(\frac{\cos\theta \mp_r i}{\cos\theta + i}\hat{m} + \frac{\cos\theta \pm_r i}{\cos\theta - i}\hat{\bar{m}}\right). \tag{4.73}$$

Plugging this into Eqs. (4.53), one immediately sees that $\mathcal{A} = \mathcal{B} = 0$ because $F \circ \hat{l} = F \circ \hat{n} = 0$ and $P \circ \hat{m} = P \circ \hat{\bar{m}} = 0$ by Eqs. (4.8) and (4.65). As such, we obtain

$$\mathcal{K} = 0. \tag{4.74}$$

However, this result is misleading because it does not imply the vanishing of the Penrose-Walker constant κ along the beam in Kerr. For $H = 1$ geodesics (see App. 4.A2),

$$\kappa = \frac{\hat{\kappa}}{\epsilon} + \tilde{\kappa} + \mathcal{O}\left(\epsilon\right), \qquad \hat{\kappa} = \mathcal{K}. \tag{4.75}$$

Although we have found that the leading-order $\mathcal{O}\left(\epsilon^{-1}\right)$ piece of κ vanishes, its subleading $\mathcal{O}\left(\epsilon^{0}\right)$ piece does not: we show in App. 4.A2 that to leading-order in ϵ,

$$\kappa = \tilde{\kappa} = \omega\left(\beta_s \pm_r i\gamma_s\right), \tag{4.76}$$

where, by analogy with Eqs. (4.27)–(4.29), we defined source quantities

$$\alpha_s = -\frac{\ell}{\omega \sin\theta_s}, \qquad \beta_s = \pm_s \frac{\sqrt{\Theta(\theta_s)}}{\omega}, \qquad \gamma_s = -(\alpha_s + M\sin\theta_s). \tag{4.77}$$

Here, the choice of sign $\pm_s$ corresponds to the initial direction of the photon's polar motion.

We conclude that under our symmetry-based assumption (4.72), the formula for κ holds for all the photons received by a distant observer from the near-horizon region of an extreme Kerr black hole.

4.3.4 POLARIZATION AT THE OBSERVER

From Eq. (4.76), we can now read off

$$\kappa_1 = \omega\beta_s, \qquad \kappa_2 = \pm_r \omega\gamma_s. \tag{4.78}$$

Finally, plugging this into Eq. (4.29) yields the polarization profile measured by a distant observer:

$$\vec{\mathcal{E}} = \frac{1}{(\beta_o^2 + \gamma_o^2)} \left(\beta_o\beta_s \pm_r \gamma_o\gamma_s, \gamma_o\beta_s \mp_r \beta_o\gamma_s\right). \tag{4.79}$$

This quantity depends on both the observer parameters $(\theta_o, \alpha_o, \beta_o)$ and the source parameters $(\theta_s, \alpha_s, \beta_s)$, as well as the discrete sign choices $(\pm_r, \pm_s, \pm_o)$. We will now eliminate the variables $(\theta_s, \alpha_s, \beta_s, \pm_r, \pm_s, \pm_o)$ in favor of $(\theta_o, \alpha_o, \beta_o)$, which are the only variables parameterizing observations.

First, we have $\pm_o = \operatorname{sign}(\beta_o)$ by definition. Next, since we are interested in photons that are eventually outgoing, we set $\pm_r = 1$. (This choice does not exclude initially ingoing photons that reach a radial turning point before escaping to the far region and is therefore still completely general—see App. 4.A3 for details.) Since the conserved quantities of the geodesics are the same at the observer and the source, we can eliminate (α_s, β_s) in favor of (α_o, β_o):

$$\begin{aligned} \alpha_s &= -\frac{\ell}{\omega \sin\theta_s} = \frac{\sin\theta_o}{\sin\theta_s}\alpha_o, \\ \beta_s &= \pm_s \frac{\sqrt{\Theta(\theta_s)}}{\omega} = \pm_s\sqrt{\beta_o^2 + \gamma_o^2 - \gamma_s^2}, \end{aligned} \tag{4.80}$$

where the last equality follows from the conservation of $k/\omega^2 = \beta_i^2 + \gamma_i^2$ for $i \in \{o, s\}$. Finally, we fix θ_s and $\pm_s$ by solving the geodesic equation, as described in App. 4.A3. Putting everything together results in our prediction (4.1).

Finally, we wish to reiterate that although the calculations in this chapter were explicitly carried out only for the precisely extremal black hole with $a = M$, we expect our results to still hold (to leading order in ϵ) for near-extremal black holes with a small deviation from extremality $a = M\sqrt{1-\epsilon^2}$ with $\epsilon \ll 1$.

4.4 SUMMARY

In this chapter, we determined the polarimetric images for the near-horizon emissions of high-spin black holes. For a distant observer stationed at any fixed polar angle relative to a black hole's axis of symmetry, we found that the polarization lines form a distinctive whorl that spirals into a central point inside the black hole's shadow. An infinite series of subsidiary whorls also appear nearer the edge of the shadow, arising from photons that librate around the black hole multiple times before escaping to infinity. Further, the image lies entirely within the shadow and are not obscured by emissions from behind the black hole.

In particular, we predicted the polarization profile of the black hole centering the galaxy M87, which corresponds to an observer at a 15° polar angle. The up-close images of M87 is expected to soon be delivered by the EHT, which will also measure the polarization of the incident light. Although the signal might not be observable if it is obscured by emissions between M87's near-horizon region and the telescope, our theoretical methods and results are applicable to any future experiment that observes high-spin black holes.

4.A1 GEODESICS CONNECTING THE NEAR-HORIZON AND FAR REGIONS

It is natural to ask what happens to the Kerr momentum p and polarization f of a light beam entering (or leaving) the NHEK region (4.39). To answer this question, we first take the near-horizon limit (4.36) of p and f, resulting in

$$p(x^\mu) = \epsilon^{-H}\left[\hat{p}(X^\mu) + \mathcal{O}(\epsilon)\right], \qquad f(x^\mu) = \epsilon^{-H'}\left[\hat{f}(X^\mu) + \mathcal{O}(\epsilon)\right], \tag{4.81}$$

for some integers H and H'. Note that as discussed in Section IV of Ref.[67], these scaling powers may become fractional powers in the context of a near-extremal black hole. We can then proceed along the same lines as Ref.[67]. We begin by noting, based on physical grounds, that neither p nor f is allowed to blow up on the event horizon. Demanding their regularity on the horizon requires that $H, H' \leq 1$. Next, plugging the leading-order near-horizon expansions (4.81) into Eqs. (4.57) yields

$$\hat{p}^\mu\hat{\nabla}_\mu\hat{p}^\nu = \hat{p}^\mu\hat{\nabla}_\mu\hat{f}^\nu = 0, \qquad \hat{p}\circ\hat{p} = \hat{p}\circ\hat{f} = 0, \qquad \epsilon^{-2H'}\hat{f}\circ\hat{f} = 1, \tag{4.82}$$

where all the contractions and covariant derivatives appearing in these leading-order expressions are meant to be taken with respect to the NHEK metric (4.39), rather than the Kerr metric (4.4) that is meant to be used in Eqs. (4.57).

These equations indicate that, for any allowed weight $H \leq 1$, the NHEK vector field $\hat{p}$ describing the leading-order near-horizon beam is also tangent to a null geodesic congruence, like its Kerr counterpart p. This was to be expected: at every NHEK coordinate X^μ within the beam, $\hat{p}(X^\mu)$ must by definition equal the momentum of the photon passing through X^μ. However, it is important to note that the Kerr conserved quantities (4.19) of the photons in the beam need not equal their NHEK counterparts (4.50)—in general, their precise relation is given by

$$\omega - \Omega_H \ell = \epsilon^{-H+1}\frac{\hat{E}}{2M} = \frac{\epsilon E}{2M}, \qquad \ell = \epsilon^{-H}\hat{L} = L, \qquad k = \epsilon^{-2H}\hat{K} = K, \tag{4.83}$$

where $\Omega_H = 1/(2M)$ denotes the angular velocity of the horizon at extremality and the hatted conserved quantities are defined relative to $\hat{p}$ (so as to always be finite) while the unhatted quantities are defined relative to $P = \epsilon^{-H}\hat{p}$ (and therefore may be parametrically large or small). These nontrivial relations follow directly from the infrared limit (4.36) and the near-horizon expansions (4.81), with the various factors of ϵ arising from the scaling to a region of infinite redshift near the horizon.

Note that these relations also appear in App. B of Ref.[67]. As an example, note from the definitions (4.19) and (4.50) that $\ell = p \cdot \partial_\phi$ and $\hat{L} = \hat{p} \circ \partial_\Phi$, where ϕ and Φ are the Kerr and NHEK angular coordinates, respectively. One can check that $\partial_\phi = \partial_\Phi + \mathcal{O}(\epsilon)$, so to leading order in ϵ,

$$\ell = p \cdot \partial_\phi = \epsilon^{-H}\left[\hat{p} + \mathcal{O}\left(\epsilon^1\right)\right] \circ \partial_\Phi = \epsilon^{-H}\left[\hat{L} + \mathcal{O}\left(\epsilon^0\right)\right]. \tag{4.84}$$

On the other hand, the near-horizon limit of the polarization vector field is much more constrained by Eqs. (4.82), which are manifestly inconsistent unless $H' = 0$: indeed, if $H' \neq 0$, then the norm of the near-horizon polarization vector $\hat{f}$ either vanishes or diverges. Both situations are unphysical: the latter because it is meaningless and the former because it requires the polarization to become longitudinal, or pure gauge. Note that since the physical photon polarization is invariant under longitudinal shifts $f \to f + cp$, we must in general relax the parallel transport condition $p^\mu \nabla_\mu f^\nu = 0$ to the weaker condition $p^\mu \nabla_\mu f^\nu \propto p^\nu$, which still guarantees the parallel transport of the orthogonality condition $p \cdot f = 0$. In general, f will have a longitudinal component with weight $H' = 1$, but it can always be removed by a gauge transformation.

The values of the weights H and H' are significant because they determine the leading behavior of the fields p and f under scale transformations of the near-horizon region: the Lie derivatives of $\hat{p}$ and $\hat{f}$ along the generator H_0 of NHEK dilations $(T, R) \to (T/\epsilon, \epsilon R)$ are fixed to be

$$\mathcal{L}_{H_0}\hat{p} = H\hat{p}, \qquad \mathcal{L}_{H_0}\hat{f} = H'\hat{f} = 0. \tag{4.85}$$

4.A2 SUBLEADING ORDER EXPANSION

In this appendix, we extend the preceding discussion beyond leading order in the NHEK limit (4.36). Working to subleading order in ϵ (and recalling from App. 4.A1 that $H' = 0$), the near-horizon expansions (4.81) of the momentum p and polarization f of a light beam in Kerr are extended to

$$p(x^\mu) = \epsilon^{-H}\left[\hat{p}(X^\mu) + \epsilon\tilde{p}(X^\mu) + \mathcal{O}\left(\epsilon^2\right)\right], \tag{4.86}$$

$$f(x^\mu) = \hat{f}(X^\mu) + \epsilon\tilde{f}(X^\mu) + \mathcal{O}\left(\epsilon^2\right), \tag{4.87}$$

where the limit requires that the following symmetry properties be satisfied:

$$\begin{aligned}\mathcal{L}_{H_0}\hat{p} &= H\hat{p}, &(4.88)\\ \mathcal{L}_{H_0}\hat{f} &= 0, &(4.89)\\ \mathcal{L}_{H_0}\tilde{p} &= (H-1)\tilde{p}, &(4.90)\\ \mathcal{L}_{H_0}\tilde{f} &= -\tilde{f}. &(4.91)\end{aligned}$$

Likewise, in the NHEK limit (4.36), the Penrose-Walker constant (4.24) in Kerr has an expansion

$$\kappa = \epsilon^{-H}\left[\hat{\kappa} + \epsilon\tilde{\kappa} + \mathcal{O}\left(\epsilon^2\right)\right]. \tag{4.92}$$

We now focus on the case $H = 1$ of relevance to the discussion in Section 4.3.3 of generic photons, with leading momentum $\hat{p}$ as given in Eqs. (4.65),

$$\hat{p} = \frac{2M\omega - \ell}{2M^2\Gamma}\left(\frac{1}{R^2}\,\partial_T \pm_r \partial_R - \frac{1}{R}\,\partial_\Phi\right). \tag{4.93}$$

There is a unique corresponding choice (4.73) of leading-order polarization obeying the symmetry-based conditions (4.72),

$$\hat{f} = \frac{1}{\sqrt{2}}\left(\frac{\cos\theta \mp_r i}{\cos\theta + i}\hat{m} + \frac{\cos\theta \pm_r i}{\cos\theta - i}\hat{\bar{m}}\right), \tag{4.94}$$

which solves Eqs. (4.57) to leading order in ϵ. As claimed in Eq. (4.74), with these choices, we find that the Penrose-Walker constant vanishes to leading order,

$$\hat{\kappa} = 0. \tag{4.95}$$

Next, to subleading order in the near-horizon limit (4.36), the Kerr four-momentum (4.16) of a generic photon is

$$\begin{aligned}\tilde{p} \;&=\; \frac{1}{2M^2\Gamma}\Big(\frac{\ell\delta + 4\omega M(1-\delta)}{2R\Gamma}\,\partial_T \pm_r \frac{R}{\Gamma}\left(\ell - \omega M\delta\right)\partial_R \\ &\quad +\omega\beta_s\,\partial_\theta + \frac{\ell\left(\frac{1}{\delta} - \frac{3}{2}\right) - \omega M\left(2 - \frac{5}{2}\delta + \frac{1}{4}\delta^2\right)}{\Gamma}\,\partial_\Phi\Big),\end{aligned} \tag{4.96}$$

where we introduced $\delta(\theta) \equiv \Gamma(\theta)\Lambda(\theta) = \sin^2\theta$ and β_s was defined in Eq. (4.80). There is a unique corresponding choice of subleading-order polarization obeying the conditions in Eq. (4.88),

$$\begin{aligned}\tilde{f} \;&=\; \frac{R}{4M\Gamma(2M\omega - \ell)}\left(\frac{2\ell\Gamma\cot\theta + \omega\left(M\sin 2\theta \mp_r \beta_s\right)}{R}\,\partial_T\right. \\ &\quad +\omega R\left(\beta_s \pm_r M\sin 2\theta\right)\partial_R \pm_r \frac{\ell\left(\frac{2}{\delta} - 3\right) + \omega M\left(2 - \delta + \delta^2\right)}{\Gamma}\,\partial_\theta \\ &\quad \left. + \left[\frac{\ell\left(\frac{2}{\delta} - 1\right) - \omega M(2+\delta)}{\tan\theta} \pm_r \omega\beta_s\right]\partial_\Phi\right),\end{aligned} \tag{4.97}$$

which solves Eqs. (4.57) to subleading order in ϵ. Here, note that we cannot impose special-conformal invariance—in fact, $\mathcal{L}_{H_-}\tilde{f} \not\propto \tilde{f}$—but we do continue to impose the symmetries of Kerr, $\mathcal{L}_{H_+}\tilde{f} = \mathcal{L}_{W_0}\tilde{f} = 0$. With this choice, we reproduce the expression (4.76) for the subleading piece of the Penrose-Walker constant.

4.A3 ANALYTIC RAY-TRACING

The polarization vector (4.79) depends explicitly on the polar angle θ_s at the point of emission. Therefore, in order to determine the polarization profile measured by a distant observer located at $(t_o, r_o, \theta_o, \phi_o)$, we need to find the null geodesic connecting a point (α_o, β_o) on the observer's screen to the point of emission $(t_s, r_s, \theta_s, \phi_s)$ in the near-horizon region. Without loss of generality, we can set $t_o = \phi_o = 0$ and assume that the observer lies in the northern hemisphere, $\theta_o \in [0, \pi/2]$, because the entire configuration is stationary, axisymmetric, and reflection-symmetric across the equatorial plane, respectively.

The (r, θ) part of the equation is

$$\int_{r_s}^{r_o} \frac{\mathrm{d}r}{\pm\sqrt{\mathcal{R}(r)}} = \int_{\theta_s}^{\theta_o} \frac{\mathrm{d}\theta}{\pm\sqrt{\Theta(\theta)}}, \tag{4.98}$$

where the integrals are to be evaluated along the geodesic, with the signs of the integrands chosen to match those of $\mathrm{d}r$ and $\mathrm{d}\theta$, respectively. Meanwhile, the t and ϕ components of the geodesic equation determine the coordinate time elapsed $\Delta t = t_o - t_s$ and the number of windings about the axis of symmetry $n = \mathrm{mod}_{2\pi} \Delta\phi = \mathrm{mod}_{2\pi}(\phi_o - \phi_s)$. These quantities are both manifestly real whenever the integrals in Eq. (4.98) are real, but we do not need to compute them in this problem thanks to the assumed stationarity and axisymmetry of the polarization profile at the source.

The ray-tracing problem has therefore reduced to a two-dimensional calculation in the poloidal plane: given a photon originating from the point (r_s, θ_s) in the near-horizon region, we must solve Eq. (4.98) in order to determine the corresponding point $(\alpha_o(\theta_s), \beta_o(\theta_s))$ that the photon hits on the observer's screen, after which we can plug into Eq. (4.79) to determine the observed polarization at that point.

We are interested in light emitted from the near-horizon region of extreme black holes with $a = M$. In that case, the entire NHEK region of emission is squeezed into the Boyer-Lindquist horizon radius $r = M$. Generic $H = 1$ geodesics traverse this region at constant θ, since their leading-order four-momentum is of the form (4.60), $i.e.$, $p^\theta = 0$. Hence, these geodesics emerge from the near-horizon region at (r_s, θ_s), with $r_s = M$ and θ_s the angle of emission.

Having fixed the parameters of the problem, it is helpful to introduce new energy-rescaled dimensionless variables

$$R = \frac{r - M}{M}, \tag{4.99}$$

$$\lambda = \frac{\ell}{\omega M}, \tag{4.100}$$

$$q = \frac{1}{\omega M}\sqrt{k - (\ell - \omega M)^2} = \frac{\sqrt{Q}}{\omega M}, \tag{4.101}$$

$$\Delta_r = \frac{1}{2}\sqrt{q^2 + (\lambda - 1)^2}. \tag{4.102}$$

Note that the variables (λ, q) defined here differ from those introduced in Ref.[44], which were adapted to the study of $H = 0$ geodesics. The variable Q is the Carter integral mentioned in footnote §.

Geodesics that pass through the equatorial plane always satisfy $q^2 \geq 0$, whereas those that do not have $q^2 < 0$. Nonetheless, the necessary positivity of $(\omega M)^{-2}\,\Theta(\theta) = q^2 + (\lambda - 1)^2 -$

$(\lambda\csc\theta-\sin\theta)^2$ guarantees that Δ_r is real, and moreover that an asymptotic observer situated at angle θ_o only receives light with

$$\Delta_r \geq \frac{1}{2}\left|\sin\theta_o - \lambda\csc\theta_o\right| . \tag{4.103}$$

In terms of these dimensionless variables, the geodesic equation (4.98) now takes the form $I_r = G_\theta$, where

$$\begin{aligned} I_r &= \int_{R_s}^{R_o} \frac{\mathrm{d}R}{\pm\sqrt{R^4+4R^3+(7-q^2-\lambda^2)\,R^2+4(2-\lambda)R+(2-\lambda)^2}}, & (4.104)\\ G_\theta &= \int_{\theta_s}^{\theta_o} \frac{\mathrm{d}\theta}{\pm\sqrt{q^2+\cos^2\theta-\lambda^2\cot^2\theta}}, & (4.105)\end{aligned}$$

with $R_s = 0$. The properties of the radial integral as a function of (λ, q) determine the points on the observer's screen that can receive light from the near-horizon region of the black hole. In particular, the quartic polynomial

$$\mathcal{P}(R) = R^4+4R^3+\left(7-q^2-\lambda^2\right)R^2+4(2-\lambda)R+(2-\lambda)^2 \tag{4.106}$$

appearing in the denominator of the integrand of I_r must remain non-negative at all points along the geodesic.

Consider a photon emerging from the near-horizon region $R_s = 0$. In order for it to reach a distant observer at large radius $R_o \to \infty$, it cannot encounter any radial turning points along its trajectory outside of NHEK. Note that photons emitted from a given NHEK radius can still escape to infinity if they are initially ingoing and reach a turning point at a smaller NHEK radius before turning back out. This happens when one of the roots is near zero, or equivalently, only for photons near the superradiant bound $\lambda = 2$. After such photons turn around and leave NHEK, they are thereafter always outgoing. Hence, we may restrict our attention to direct emissions.

Such a turning point occurs at the smallest positive radius R_t where $\mathcal{P}(R)$ becomes negative (i.e. where $\mathcal{P}(R_t) = 0$ and $\mathcal{P}'(R_t) < 0$). The roots of $\mathcal{P}(R)$ are given by

$$R_1 = -(\Delta_r + 1) + \sqrt{(\Delta_r + 1)^2 + \lambda - 2}, \tag{4.107}$$

$$R_2 = (\Delta_r - 1) - \sqrt{(\Delta_r - 1)^2 + \lambda - 2}, \tag{4.108}$$

$$R_3 = (\Delta_r - 1) + \sqrt{(\Delta_r - 1)^2 + \lambda - 2}, \tag{4.109}$$

$$R_4 = -(\Delta_r + 1) - \sqrt{(\Delta_r + 1)^2 + \lambda - 2}. \tag{4.110}$$

Since $\mathcal{P}(0) = (2 - \lambda)^2 \geq 0$ and $\mathcal{P}(\pm\infty) = +\infty$, there are two qualitatively different classes of geodesics which can connect to the observer at infinity. The first class consists of geodesics with (λ, q) such that all of the roots R_i are complex or negative. In this case, there are no zeroes of $\mathcal{P}(R)$ lying on the contour of integration extending from $R = 0$ to $R = \infty$, so the radial integral converges to a finite quantity and the geodesic encounters a finite number of angular turning points according to Eq. (4.98). The second class consists of geodesics with (λ, q) such that $\mathcal{P}(R)$ develops a double root on the positive real axis. (R_4, if real, is always negative, so there can be at most one double root on the positive real axis.) In this case, the radial integral diverges logarithmically, and the geodesic encounters a divergent number of angular turning points as it winds around the black hole. In fact, the second class of geodesics is a limiting case of the first, where complex or negative roots approach and pinch the contour of integration as we vary (λ, q).

It is straightforward to determine the restricted range of (λ, q) labeling the geodesics that connect the near-horizon region to the observer. First, note that if $\lambda > 2$ (that is, if the photon is below the superradiant bound $\omega < \Omega_H \ell$), then all of the roots are real, R_1 and R_3 are positive, and the photon cannot escape to infinity. Conversely, a photon below the superradiant bound coming in from infinity will bounce off the black hole. We can therefore restrict our attention to the case $\lambda \leq 2$. The roots R_1 and R_4 may then be real but they can never be positive, so the only constraints come from R_2 and R_3. For $\Delta_r < 1$, these roots (if real) are negative. However, for $\Delta_r - 1 \geq \sqrt{2-\lambda} \geq 0$, they are real and positive, and the photon cannot escape to infinity.

In summary, a near-horizon photon can reach a distant observer at polar angle θ_o if and only if $\lambda \leq 2$ (it is above the superradiant bound), and moreover

$$\frac{1}{2} \left|\sin\theta_o - \lambda \csc\theta_o\right| - 1 \leq \Delta_r - 1 \leq \sqrt{2-\lambda}. \tag{4.111}$$

This condition defines a region on the observer's screen which coincides identically with the shadow cast by a uniformly backlit extremal black hole, as can be verified by substituting

$$\lambda = -\frac{\alpha_o \sin\theta_o}{M}, \qquad q = \frac{1}{M}\sqrt{(\alpha_o^2 - M^2)\cos^2\theta_o + \beta_o^2}, \tag{4.112}$$

and comparing to Eqs. (4.34). The interior of this region corresponds to geodesics of the first class discussed above, while near the boundary $\Delta_r - 1 = \sqrt{2-\lambda}$ the polynomial $\mathcal{P}(R)$ develops at double root at $R = \sqrt{2-\lambda}$. (Note that the shadow's vertical edge (4.33) lies on the line $\lambda = 2$, corresponding to the case when the double root emerges at the lower endpoint of integration.) Therefore, light rays that impinge upon the observer's screen near the edge of the shadow must have librated around the black hole an infinite number of times before reaching the asymptotic region.

For the parameter range (4.111), the radial integral takes the form

$$I_r = \frac{2}{\sqrt{r_{12}r_{34}}}\left[F\left(\arcsin\sqrt{\frac{r_{12}}{r_{32}}}\,\middle|\,\frac{r_{14}r_{32}}{r_{12}r_{34}}\right) - F\left(\arcsin\sqrt{\frac{R_3}{R_1}\frac{r_{12}}{r_{32}}}\,\middle|\,\frac{r_{14}r_{32}}{r_{12}r_{34}}\right)\right], \tag{4.113}$$

where $r_{ij} \equiv R_i - R_j$ and $F(\phi|x)$ denotes the incomplete elliptic integral of the first kind.

We have seen that light emitted from the NHEK region must always appear within the shadow cast by the black hole on the observer's screen. In order to find the explicit map from the point of emission to the corresponding point on the observer's screen, we still have to solve the (r, θ) geodesic equation (4.98). As was the case for the radial integral, one can read off qualitative features of the angular motion from the nature of the roots of the polynomial appearing in the integrand of G_θ. After a change of variables $u = \cos^2\theta$, that integrand becomes

$$\operatorname{sign}\left(\theta - \frac{\pi}{2}\right)\frac{\mathrm{d}\theta}{\sqrt{\Theta(\theta)}} = \frac{1}{2}\frac{\mathrm{d}u}{\sqrt{u(u_+ - u)(u - u_-)}}, \tag{4.114}$$

where

$$u_{\pm} = \Delta_\theta \pm \sqrt{\Delta_\theta^2 + q^2}, \qquad \Delta_\theta = \frac{1}{2}\left(1 - q^2 - \lambda^2\right). \tag{4.115}$$

Geodesic motion in the angular direction is constrained by the requirement that the argument of the square root remain positive. While we always have $u_+ \in [0,1]$, there are two qualitatively different behaviors distinguished by the sign of u_-. For $q^2 > 0$, u_- is negative and the geodesic oscillates about the equatorial plane in the angular region $\cos^2\theta \in [0, u_+]$. On the other hand, when $q^2 < 0$, then u_- is also positive and the geodesic is constrained to the angular region $\cos^2\theta \in [u_-, u_+] \subset [0,1]$, defining a cone either entirely above or entirely below the equatorial plane. We will ignore the boundary case $q = 0$, as it corresponds to a measure-zero curve on the observer's screen.

The angular integral G_θ was evaluated for Kerr geodesics with $q^2 > 0$ (and generic a) in Ref.[44] in terms of $F(\phi|x)$, the incomplete elliptic integral of the first kind. We will adopt the convention

$$F(\phi|x) = \int_0^\phi \frac{\mathrm{d}t}{\sqrt{1 - x\sin^2 t}}, \tag{4.116}$$

and we introduce

$$\Psi_j = \arcsin\left(\frac{\cos\theta_j}{\sqrt{u_+}}\right), \qquad \Upsilon_j = \arcsin\sqrt{\frac{\cos^2\theta_j - u_-}{u_+ - u_-}} \tag{4.117}$$

for notational convenience. For $\theta_o \in [0, \pi/2]$ in extreme Kerr,

$$G_\theta^{q^2>0} = \frac{1}{\sqrt{-u_-}} \left\{ 2mK\left(\frac{u_+}{u_-}\right) \pm_o \left[(-1)^m F\left(\Psi_s \middle| \frac{u_+}{u_-}\right) - F\left(\Psi_o \middle| \frac{u_+}{u_-}\right) \right] \right\}, \tag{4.118}$$

where m is the number of turning points in the polar motion and $K(x) = F(\pi/2|x)$ denotes the complete elliptic integral of the first kind. Likewise, for $q^2 < 0$, $\theta_o \in [0, \pi/2]$ and $a = M$, one can show that

$$\begin{aligned} G_\theta^{q^2<0} &= \frac{1}{\sqrt{u_-}} \left(m \pm_o \frac{1-(-1)^m}{2} \right) K\left(1 - \frac{u_+}{u_-}\right) && (4.119) \\ &\pm_o \frac{1}{\sqrt{u_-}} \left[(-1)^m F\left(\Upsilon_s \middle| 1 - \frac{u_+}{u_-}\right) - F\left(\Upsilon_o \middle| 1 - \frac{u_+}{u_-}\right) \right]. && (4.120) \end{aligned}$$

We can now solve the geodesic equation (4.98), $I_r = G_\theta$, for θ_s. After some technical manipulations, this results in

$$\cos\theta_s = \begin{cases} \pm_o \sqrt{u_+} (-1)^m \mathrm{sn}\left(X_m \middle| \frac{u_+}{u_-}\right) & q^2 > 0, \\ \sqrt{u_-} \mathrm{dn}\left(Y_m \middle| 1 - \frac{u_+}{u_-}\right) & q^2 < 0, \end{cases} \tag{4.121}$$

where we introduced the Jacobi elliptic functions. Note that the elliptic function $\mathrm{sn}(u|x)$ inverts the incomplete elliptic integral of the first kind: $\mathrm{sn}\left(F(\arcsin\phi|x)|x\right) = \phi$. The elliptic function $\mathrm{dn}(u|x)$ satisfies $\mathrm{dn}^2(u|x) + x\,\mathrm{sn}^2(u|x) = 1$. While $\mathrm{sn}(-u|x) = -\mathrm{sn}(u|x)$ is odd in its first argument,

$\mathrm{dn}(-u|x) = \mathrm{dn}(u|x)$ is even. $\mathrm{sn}(u|x)$ and $\mathrm{dn}(u|x)$ and defined the quantities

$$
\begin{aligned}
X_m &= \sqrt{-u_-}I_r \pm_o F\left(\Psi_o\middle|\frac{u_+}{u_-}\right) - 2mK\left(\frac{u_+}{u_-}\right), && (4.122) \\
Y_m &= \sqrt{u_-}I_r \pm_o F\left(\Upsilon_o\middle|1-\frac{u_+}{u_-}\right) - \left(m \pm_o \frac{1-(-1)^m}{2}\right)K\left(1-\frac{u_+}{u_-}\right). && (4.123)
\end{aligned}
$$

Although it is not immediately apparent, both expressions for $\cos\theta_s$ are in fact independent of the number m of polar turning points along the trajectory. In order to see this, begin by noting that

$$
\begin{aligned}
X_{m+1} &= X_m - 2K\left(\frac{u_+}{u_-}\right), && (4.124) \\
Y_{m+1} &= Y_m - \left[1 \pm_o (-1)^m\right]K\left(1-\frac{u_+}{u_-}\right). && (4.125)
\end{aligned}
$$

Next, note that because of the periodicity conditions $\mathrm{sn}(u \pm 2K(x)|x) = -\mathrm{sn}(u|x)$ and $\mathrm{dn}(u \pm 2K(x)|x) = \mathrm{dn}(u|x)$, the quantities $(-1)^m\mathrm{sn}(X_m|u_+/u_-)$ and $\mathrm{dn}(Y_m|1-u_+/u_-)$ are both invariant under integer shifts in m. It follows that X_m and Y_m can be respectively replaced by X_0 and Y_0 in Eq. (4.121), from which the m-dependence thereby disappears, as claimed.

Moreover, after some further technical manipulations, the two expressions for $\cos\theta_s$ in Eq. (4.121) can be packaged together into the remarkably simple formula (valid for all $q^2 \neq 0$)

$$
\theta_s = \arccos\left[\pm_o\sqrt{u_+}\mathrm{sn}\left(\frac{\sqrt{-u_-}}{\mathrm{sign}(-u_-)}I_r \pm_o F\left(\Psi_o\middle|\frac{u_+}{u_-}\right)\middle|\frac{u_+}{u_-}\right)\right]. \qquad (4.126)
$$

Note that to further simplify the $q^2 < 0$ expression and relate it to the $q^2 > 0$ case, one repeatedly invokes the relation

$$K(x)-\frac{1}{\sqrt{x}}K\left(\frac{1}{x}\right)=-iK(1-x), \tag{4.127}$$

valid for $x=u_+/u_-\geq 1$, along with the nontrivial identity

$$\frac{1}{\sqrt{x}}K\left(\frac{1}{x}\right)-F\left(\arcsin\sqrt{\frac{u_j}{u_+}}\middle|x\right)=iF\left(\arcsin\sqrt{\frac{u_j-u_-}{u_+-u_-}}\middle|1-x\right),\qquad x=\frac{u_+}{u_-}. \tag{4.128}$$

While the above expression for θ_s is independent of the integer m, the sign $\pm_s$ does depend on its parity,

$$\pm_s=\mathrm{sign}(p_\theta)|_{R_s}=(-1)^m\mathrm{sign}(\beta_o)=(-1)^m\pm_o, \tag{4.129}$$

and must be determined for each geodesic. If $\theta_o=0$, then $\pm_o$ is ill-defined and we take $\pm_s=(-1)^{m+1}$ by convention. Note that when $\theta_o=0$, the β_o-axis becomes ill-defined because the projection of the axis of symmetry onto the plane perpendicular to the observer's line of sight degenerates to a point. Moreover, the value of m is also ill-defined because the observer sits on a turning point of the incoming photons' trajectories. In drawing the edge-on case in Fig. 4.1, we adopted the convention that the direct light should be labeled $m=0$, in which case $\pm_s=(-1)^{m+1}$.

In practice, to produce polarization plots, we only need to find the boundaries between regions of different m. Since the source dependent terms in Eqs. (4.118)-(4.119) are bounded, as the radial integral grows, more turning points are necessary to satisfy the geodesic equation. Schematically, since the radial integral assumes small values near the center of the shadow and diverges near the boundary, one expects nested regions of increasing m as one moves out towards the edge of the shadow. In the $q^2 < 0$ case, we find that $m = 0$ whenever

$$0 < \pm_o \sqrt{u_-} I_r + F\left(\Upsilon_o \middle| 1 - \frac{u_+}{u_-}\right) < K\left(1 - \frac{u_+}{u_-}\right), \tag{4.130}$$

and $m = 1$ otherwise. In the $q^2 > 0$ case, geodesics with m angular turning points obey

$$(2m-1)K\left(\frac{u_+}{u_-}\right) < \sqrt{-u_-} I_r \pm_o F\left(\Psi_o \middle| \frac{u_+}{u_-}\right) < (2m+1)K\left(\frac{u_+}{u_-}\right). \tag{4.131}$$

The contours of the regions satisfying this inequality for different m are the boundaries of the regions depicted with different colors in Fig. 4.1. Mathematically, the existence of these regions can ultimately be traced back to the periodicity of the elliptic function $\mathrm{sn}(u|x)$, which implies that its inverse $F\left(\arcsin \mathrm{sn}(u|x) \middle| x\right)$ is multivalued (not equal to u everywhere). As such, when the formula (4.126) for θ_s is substituted back into the geodesic integrals (4.118)-(4.119), one must choose the appropriate branch of the elliptic integral to satisfy Eq. (4.98). This inverse has infinitely many branches labeled by m, which correspond to the infinitely many coverings of the horizon in our polarimetric images.

5

Conclusion

In this thesis, we examined astrophysical processes in the vicinity of the event horizon of an extreme Kerr black hole. This region of spacetime has an $\mathsf{SL}(2,\mathbb{R}) \times \mathsf{U}(1)$ isometry. We explored the consequences of the enhanced symmetries on electromagnetic emissions from this region and performed a number of analytical computations that are traditionally done only numerically.

We first solved for the near-superradiant geodesics that extend from the near-horizon region to a distant observatory, expressing our results in terms of elementary functions. We used the method of matched asymptotic expansions to integrate, to leading order in the deviation from the superradiant bound, all radial integrals in Carter's integral geodesic equations. They relate an endpoint of a null geodesic near the horizon to its endpoint in the region far from the black hole and the associated angular momentum constant along the geodesic. Our results enabled one to solve explicitly for various parameters appearing in the integral geodesic equations, a necessary step for various applications.

Building upon these methods and using geometrical optics, we computed the broadening of electromagnetic line emissions from the innermost part of an accretion disk. We obtained an analytic formula for the flux observed at infinity as a function of the photons' redshift. It is independent of the disk model and therefore universal. Further, we proposed a model for a radiant disk that respects the symmetries of the near-horizon region of an extreme Kerr black hole. Due to the logarithmic divergence of the disk's proper length at extremality, this model implies a logarithmically divergent overall proportionality constant in the flux.

Finally, we investigated the polarized near-horizon emissions from fast-spinning black holes and found patterns of whorls aligned with the black hole's spin. For a distant observer stationed at any fixed polar angle relative to a black hole's axis of symmetry, the polarization lines form a distinctive whorl that spirals into a central point inside the black hole's shadow. An infinite series of subsidiary whorls also appear nearer the edge of the shadow, arising from photons that librate around the black hole multiple times before escaping to infinity. The image lies entirely within the shadow and are not obscured by emissions from behind the black hole.

Fast-spinning black holes are of not only theoretical relevance, but observational. Our computation in Chapter 3 is directly relevant to the profile of Fe$K\alpha$ line emissions from black hole accretion disks. It could pertain to spectral observations by experiments such as XMM-Newton, Suzaku, and NuSTAR. And our prediction for the polarization profile of near-horizon emissions from M87 is relevant to experiments like the Event Horizon Telescope, which is expected to measure the polarization of the incident light.

References

[1] Achilleas P. Porfyriadis, Yichen Shi, and Andrew Strominger. Photon Emission Near Extreme Kerr Black Holes. *Phys. Rev.*, D95(6):064009, 2017. doi: 10.1103/PhysRevD.95.064009.

[2] Alexandru Lupsasca, Achilleas P. Porfyriadis, and Yichen Shi. Critical Emission from a High-Spin Black Hole. *Phys. Rev.*, D97(6):064017, 2018. doi: 10.1103/PhysRevD.97.064017.

[3] Delilah Gates, Daniel Kapec, Alexandru Lupsasca, Yichen Shi, and Andrew Strominger. Polarization Whorls from M87 at the Event Horizon Telescope. 2018.

[4] Albert Einstein. The Foundation of the General Theory of Relativity. *Annalen Phys.*, 49(7): 769–822, 1916. doi: 10.1002/andp.200590044,10.1002/andp.19163540702.

[5] D. Walsh, R. F. Carswell, and R. J. Weymann. 0957 + 561 A, B - Twin quasistellar objects or gravitational lens. *Nature*, 279:381–384, 1979. doi: 10.1038/279381a0.

[6] B. P. Abbott et al. Observation of Gravitational Waves from a Binary Black Hole Merger. *Phys. Rev. Lett.*, 116(6):061102, 2016. doi: 10.1103/PhysRevLett.116.061102.

[7] Karl Schwarzschild. On the gravitational field of a mass point according to Einstein's theory. *Sitzungsber. Preuss. Akad. Wiss. Berlin (Math. Phys.)*, 1916:189–196, 1916.

[8] H. Reissner. Über die Eigengravitation des elektrischen Feldes nach der Einsteinschen Theorie. *Annalen der Physik*, 355:106–120, 1916. doi: 10.1002/andp.19163550905.

[9] H. Weyl. Zur Gravitationstheorie. *Annalen der Physik*, 359:117–145, 1917. doi: 10.1002/andp.19173591804.

[10] G. Nordström. On the Energy of the Gravitation field in Einstein's Theory. *Koninklijke Nederlandse Akademie van Wetenschappen Proceedings Series B Physical Sciences*, 20:1238–1245, 1918.

[11] G. B. Jeffery. The Field of an Electron on Einstein's Theory of Gravitation. *Proceedings of the Royal Society of London Series A*, 99:123–134, May 1921. doi: 10.1098/rspa.1921.0028.

[12] Albert Einstein. On a stationary system with spherical symmetry consisting of many gravitating masses. *Annals Math.*, 40:922–936, 1939. doi: 10.2307/1968902.

[13] R. P. Kerr. Gravitational Field of a Spinning Mass as an Example of Algebraically Special Metrics. *Physical Review Letters*, 11:237–238, September 1963. doi: 10.1103/PhysRevLett.11.237.

[14] E. T. Newman, E. Couch, K. Chinnapared, A. Exton, A. Prakash, and R. Torrence. Metric of a Rotating, Charged Mass. *Journal of Mathematical Physics*, 6:918–919, June 1965. doi: 10.1063/1.1704351.

[15] A. Friedmann. Über die Krümmung des Raumes. *Zeitschrift fur Physik*, 10:377–386, 1922. doi: 10.1007/BF01332580.

[16] A. Friedmann. Über die Möglichkeit einer Welt mit konstanter negativer Krümmung des Raumes. *Zeitschrift fur Physik*, 21:326–332, December 1924. doi: 10.1007/BF01328280.

[17] G. Lemaître. Expansion of the universe, A homogeneous universe of constant mass and increasing radius accounting for the radial velocity of extra-galactic nebulae. *Mon. Not. Roy. Astron. Soc.*, 91:483–490, March 1931. doi: 10.1093/mnras/91.5.483.

[18] H. P. Robertson. Kinematics and World-Structure. *Astrophys. J.*, 82:284, November 1935. doi: 10.1086/143681.

[19] A. G. Walker. On Milne's Theory of World-Structure. *Proceedings of the London Mathematical Society, (Series 2) volume 42, p. 90-127*, 42:90–127, 1937. doi: 10.1112/plms/s2-42.1.90.

[20] W. Israel. Event Horizons in Static Vacuum Space-Times. *Physical Review*, 164:1776–1779, December 1967. doi: 10.1103/PhysRev.164.1776.

[21] James M. Bardeen, William H. Press, and Saul A Teukolsky. Rotating black holes: Locally nonrotating frames, energy extraction, and scalar synchrotron radiation. *Astrophys. J.*, 178: 347, 1972. doi: 10.1086/151796.

[22] Ramesh Narayan and Jeffrey E. McClintock. Observational Evidence for Black Holes. 2013.

[23] M. Coleman Miller and E. J. M Colbert. Intermediate - mass black holes. *Int. J. Mod. Phys.*, D13:1–64, 2004. doi: 10.1142/S0218271804004426.

[24] Marta Volonteri, Piero Madau, Eliot Quataert, and Martin J. Rees. The Distribution and cosmic evolution of massive black hole spins. *Astrophys. J.*, 620:69–77, 2005. doi: 10.1086/426858.

[25] J. Kormendy and D. Richstone. Inward Bound—The Search For Supermassive Black Holes In Galactic Nuclei. *Annual Review of Astronomy and Astrophysics*, 33:581, 1995. doi: 10.1146/annurev.aa.33.090195.003053.

[26] R. Schödel, T. Ott, R. Genzel, R. Hofmann, M. Lehnert, A. Eckart, N. Mouawad, T. Alexander, M. J. Reid, R. Lenzen, M. Hartung, F. Lacombe, D. Rouan, E. Gendron, G. Rousset, A.-M. Lagrange, W. Brandner, N. Ageorges, C. Lidman, A. F. M. Moorwood, J. Spyromilio, N. Hubin, and K. M. Menten. A star in a 15.2-year orbit around the supermassive black hole at the centre of the Milky Way. *Nature*, 419:694–696, October 2002. doi: 10.1038/nature01121.

[27] C. T. Bolton. Identification of Cygnus X-1 with HDE 226868. *Nature*, 235:271–273, February 1972. doi: 10.1038/235271b0.

[28] B. L. Webster and P. Murdin. Cygnus X-1-a Spectroscopic Binary with a Heavy Companion? *Nature*, 235:37–38, January 1972. doi: 10.1038/235037a0.

[29] S. A. Farrell, N. A. Webb, D. Barret, O. Godet, and J. M. Rodrigues. An intermediate-mass black hole of over 500 solar masses in the galaxy ESO 243-49. *Nature*, 460:73?75, 2009. doi: 10.1038/nature08083.

[30] N. I. Shakura and R. A. Sunyaev. Black holes in binary systems. Observational appearance. *Astronomy and Astrophysics*, 24:337–355, 1973.

[31] S. Gillessen, P. M. Plewa, F. Eisenhauer, R. Sari, I. Waisberg, M. Habibi, O. Pfuhl, E. George, J. Dexter, S. von Fellenberg, T. Ott, and R. Genzel. An update on monitoring stellar orbits in the galactic center. *Astrophys. J.*, 837(1):30, 2017. URL `http://stacks.iop.org/0004-637X/837/i=1/a=30`.

[32] Laura W. Brenneman and Christopher S. Reynolds. Constraining Black Hole Spin Via X-ray Spectroscopy. *Astrophys. J.*, 652:1028–1043, 2006. doi: 10.1086/508146.

[33] G. Reber. Cosmic Static. *Astrophys. J.*, 100:279, November 1944. doi: 10.1086/144668.

[34] P. J. Hargrave and M. Ryle. Observations of Cygnus A with the 5-km radio telescope. *Mon. Not. Roy. Astron. Soc.*, 166:305–327, February 1974. doi: 10.1093/mnras/166.2.305.

[35] I. S. Shklovsky. On the Nature of the Source of X-Ray Emission of Sco XR-1. *Astrophys. J.*, 148:L1, April 1967. doi: 10.1086/180001.

[36] K. Gebhardt, R. Bender, G. Bower, A. Dressler, S. M. Faber, A. V. Filippenko, R. Green, C. Grillmair, L. C. Ho, J. Kormendy, T. R. Lauer, J. Magorrian, J. Pinkney, D. Richstone, and S. Tremaine. A Relationship between Nuclear Black Hole Mass and Galaxy Velocity Dispersion. *Astrophys. J.*, 539:L13–L16, August 2000. doi: 10.1086/312840.

[37] L. Ferrarese and D. Merritt. A Fundamental Relation between Supermassive Black Holes and Their Host Galaxies. *Astrophys. J.*, 539:L9–L12, August 2000. doi: 10.1086/312838.

[38] F. K. Baganoff, M. W. Bautz, W. N. Brandt, G. Chartas, E. D. Feigelson, G. P. Garmire, Y. Maeda, M. Morris, G. R. Ricker, L. K. Townsley, and F. Walter. Rapid X-ray flaring from the direction of the supermassive black hole at the Galactic Centre. *Nature*, 413:45–48, September 2001. doi: 10.1038/35092510.

[39] S. Doeleman, E. Agol, D. Backer, F. Baganoff, G. C. Bower, A. Broderick, A. Fabian, V. Fish, C. Gammie, P. Ho, M. Honman, T. Krichbaum, A. Loeb, D. Marrone, M. Reid, A. Rogers, I. Shapiro, P. Strittmatter, R. Tilanus, J. Weintroub, A. Whitney, M. Wright, and L. Ziurys. Imaging an Event Horizon: submm-VLBI of a Super Massive Black Hole. In *astro2010: The Astronomy and Astrophysics Decadal Survey*, volume 2010 of *ArXiv Astrophysics e-prints*, 2009.

[40] Laura Brenneman. Measuring Supermassive Black Hole Spins in Active Galactic Nuclei. 2013. doi: 10.1007/978-1-4614-7771-6.

[41] E. Noether. Invariante variationsprobleme. *Nachrichten von der Gesellschaft der Wissenschaften zu G□ttingen, Mathematisch-Physikalische Klasse*, 1918:235–257, 1918. URL `http://eudml.org/doc/59024`.

[42] Brandon Carter. Global structure of the Kerr family of gravitational fields. *Phys. Rev.*, 174: 1559–1571, 1968. doi: 10.1103/PhysRev.174.1559.

[43] James M. Bardeen and Gary T. Horowitz. The Extreme Kerr throat geometry: A Vacuum analog of AdS(2) x S**2. *Phys. Rev.*, D60:104030, 1999. doi: 10.1103/PhysRevD.60.104030.

[44] Samuel E. Gralla, Alexandru Lupsasca, and Andrew Strominger. Observational Signature of High Spin at the Event Horizon Telescope. *Mon. Not. Roy. Astron. Soc.*, 475(3):3829–3853, 2018. doi: 10.1093/mnras/sty039.

[45] Albert Einstein. Lens-like action of a star by the deviation of light in the gravitational field. *Science*, 84(2188):506–507, 1936. ISSN 0036-8075. doi: 10.1126/science.84.2188.506. URL `http://science.sciencemag.org/content/84/2188/506`.

[46] B. P. Abbott, R. Abbott, T. D. Abbott, M. R. Abernathy, F. Acernese, K. Ackley, C. Adams, T. Adams, P. Addesso, R. X. Adhikari, et al. GW151226: Observation of Gravitational Waves from a 22-Solar-Mass Binary Black Hole Coalescence. *Phys. Rev. Lett.*, 116(24):241103, June 2016. doi: 10.1103/PhysRevLett.116.241103.

[47] B. P. Abbott, R. Abbott, T. D. Abbott, F. Acernese, K. Ackley, C. Adams, T. Adams, P. Addesso, R. X. Adhikari, V. B. Adya, et al. GW170104: Observation of a 50-Solar-Mass Binary Black Hole Coalescence at Redshift 0.2. *Phys. Rev. Lett.*, 118(22):221101, June 2017. doi: 10.1103/PhysRevLett.118.221101.

[48] B. P. Abbott, R. Abbott, T. D. Abbott, F. Acernese, K. Ackley, C. Adams, T. Adams, P. Addesso, R. X. Adhikari, V. B. Adya, et al. GW170814: A Three-Detector Observation of Gravitational Waves from a Binary Black Hole Coalescence. *Phys. Rev. Lett.*, 119(14):141101, October 2017. doi: 10.1103/PhysRevLett.119.141101.

[49] B. P. Abbott, R. Abbott, T. D. Abbott, F. Acernese, K. Ackley, C. Adams, T. Adams, P. Addesso, R. X. Adhikari, V. B. Adya, et al. GW170608: Observation of a 19 Solar-mass Binary Black Hole Coalescence. *Astrophys. J.l*, 851:L35, December 2017. doi: 10.3847/2041-8213/aa9f0c.

[50] Christopher S. Reynolds. Measuring Black Hole Spin using X-ray Reflection Spectroscopy. *Space Sci. Rev.*, 183(1-4):277–294, 2014. doi: 10.1007/s11214-013-0006-6.

[51] A. E. Broderick and A. Loeb. Imaging optically-thin hotspots near the black hole horizon of Sgr A* at radio and near-infrared wavelengths. *Mon. Not. Roy. Astron. Soc.*, 367:905–916, April 2006. doi: 10.1111/j.1365-2966.2006.10152.x.

[52] S. S. Doeleman, J. Weintroub, A. E. E. Rogers, R. Plambeck, R. Freund, R. P. J. Tilanus, P. Friberg, L. M. Ziurys, J. M. Moran, B. Corey, K. H. Young, D. L. Smythe, M. Titus, D. P. Marrone, R. J. Cappallo, D. C.-J. Bock, G. C. Bower, R. Chamberlin, G. R. Davis, T. P. Krichbaum, J. Lamb, H. Maness, A. E. Niell, A. Roy, P. Strittmatter, D. Werthimer, A. R. Whitney, and D. Woody. Event-horizon-scale structure in the supermassive black hole candidate at the Galactic Centre. *Nature*, 455:78–80, September 2008. doi: 10.1038/nature07245.

[53] S. S. Doeleman, V. L. Fish, A. E. Broderick, A. Loeb, and A. E. E. Rogers. Detecting Flaring Structures in Sagittarius A* with High-Frequency VLBI. *Astrophys. J.*, 695:59–74, April 2009. doi: 10.1088/0004-637X/695/1/59.

[54] S. S. Doeleman, V. L. Fish, D. E. Schenck, C. Beaudoin, R. Blundell, G. C. Bower, A. E. Broderick, R. Chamberlin, R. Freund, P. Friberg, M. A. Gurwell, P. T. P. Ho, M. Honma, M. Inoue, T. P. Krichbaum, J. Lamb, A. Loeb, C. Lonsdale, D. P. Marrone, J. M. Moran, T. Oyama, R. Plambeck, R. A. Primiani, A. E. E. Rogers, D. L. Smythe, J. SooHoo, P. Strittmatter, R. P. J. Tilanus, M. Titus, J. Weintroub, M. Wright, K. H. Young, and L. M. Ziurys. Jet-Launching Structure Resolved Near the Supermassive Black Hole in M87. *Science*, 338:355, October 2012. doi: 10.1126/science.1224768.

[55] M. D. Johnson, V. L. Fish, S. S. Doeleman, D. P. Marrone, R. L. Plambeck, J. F. C. Wardle, K. Akiyama, K. Asada, C. Beaudoin, L. Blackburn, R. Blundell, G. C. Bower, C. Brinkerink, A. E. Broderick, R. Cappallo, A. A. Chael, G. B. Crew, J. Dexter, M. Dexter, R. Freund, P. Friberg, R. Gold, M. A. Gurwell, P. T. P. Ho, M. Honma, M. Inoue, M. Kosowsky, T. P. Krichbaum, J. Lamb, A. Loeb, R.-S. Lu, D. MacMahon, J. C. McKinney, J. M. Moran, R. Narayan, R. A. Primiani, D. Psaltis, A. E. E. Rogers, K. Rosenfeld, J. SooHoo, R. P. J. Tilanus, M. Titus, L. Vertatschitsch, J. Weintroub, M. Wright, K. H. Young, J. A. Zensus, and L. M. Ziurys. Resolved magnetic-field structure and variability near the event horizon of Sagittarius A*. *Science*, 350:1242–1245, December 2015. doi: 10.1126/science.aac7087.

[56] S. S. Doeleman. Seeing the unseeable. *Nature Astronomy*, 1:646–646, October 2017. doi: 10.1038/s41550-017-0278-y.

[57] J. Feng and Q. Wu. Constraint on the black hole spin of M87 from the accretion-jet model. *Mon. Not. Roy. Astron. Soc.*, 470:612–616, September 2017. doi: 10.1093/mnras/stx1283.

[58] Achilleas P. Porfyriadis and Andrew Strominger. Gravity waves from the Kerr/CFT correspondence. *Phys. Rev.*, D90(4):044038, 2014. doi: 10.1103/PhysRevD.90.044038.

[59] Shahar Hadar, Achilleas P. Porfyriadis, and Andrew Strominger. Gravity Waves from Extreme-Mass-Ratio Plunges into Kerr Black Holes. *Phys. Rev.*, D90(6):064045, 2014. doi: 10.1103/PhysRevD.90.064045.

[60] H. Li, C. Yu, J. Wang, and Z. Xu. Force-free magnetosphere on near-horizon geometry of near-extreme Kerr black holes. *Phys. Rev. D*, 92(2):023009, July 2015. doi: 10.1103/PhysRevD.92.023009.

[61] Alexandru Lupsasca, Maria J. Rodriguez, and Andrew Strominger. Force-Free Electrodynamics around Extreme Kerr Black Holes. *JHEP*, 12:185, 2014. doi: 10.1007/JHEP12(2014)185.

[62] N. Bai, Y.-H. Gao, and X.-b. Xu. On neutral scalar radiation by a massive orbiting star in extremal Kerr-Newman black hole. *ArXiv e-prints*, June 2014.

[63] Alexandru Lupsasca and Maria J. Rodriguez. Exact Solutions for Extreme Black Hole Magnetospheres. *JHEP*, 07:090, 2015. doi: 10.1007/JHEP07(2015)090.

[64] Shahar Hadar, Achilleas P. Porfyriadis, and Andrew Strominger. Fast plunges into Kerr black holes. *JHEP*, 07:078, 2015. doi: 10.1007/JHEP07(2015)078.

[65] Samuel E. Gralla, Achilleas P. Porfyriadis, and Niels Warburton. Particle on the Innermost Stable Circular Orbit of a Rapidly Spinning Black Hole. *Phys. Rev.*, D92(6):064029, 2015. doi: 10.1103/PhysRevD.92.064029.

[66] G. Comp□re and R. Oliveri. Near-horizon Extreme Kerr Magnetospheres. *Phys. Rev.*, D93 (2):024035, 2016. doi: 10.1103/PhysRevD.93.069906,10.1103/PhysRevD.93.024035. [Erratum: Phys. Rev.D93,no.6,069906(2016)].

[67] Samuel E. Gralla, Alexandru Lupsasca, and Andrew Strominger. Near-horizon Kerr Magnetosphere. *Phys. Rev.*, D93(10):104041, 2016. doi: 10.1103/PhysRevD.93.104041.

[68] Samuel E. Gralla, Scott A. Hughes, and Niels Warburton. Inspiral into Gargantua. *Class. Quant. Grav.*, 33(15):155002, 2016. doi: 10.1088/0264-9381/33/15/155002.

[69] Marc Casals, Samuel E. Gralla, and Peter Zimmerman. Horizon Instability of Extremal Kerr Black Holes: Nonaxisymmetric Modes and Enhanced Growth Rate. *Phys. Rev.*, D94(6): 064003, 2016. doi: 10.1103/PhysRevD.94.064003.

[70] L. M. Burko and G. Khanna. Gravitational waves from a plunge into a nearly extremal Kerr black hole. *Phys. Rev. D*, 94(8):084049, October 2016. doi: 10.1103/PhysRevD.94.084049.

[71] S.-W. Wei, B.-M. Gu, Y.-Q. Wang, and Y.-X. Liu. Photon emission of extremal Kerr-Newman black holes. *Eur. Phys. J. C*, 77:128, February 2017. doi: 10.1140/epjc/s10052-017-4699-7.

[72] S. Hadar and A. P. Porfyriadis. Whirling orbits around twirling black holes from conformal symmetry. *J. High Energy Phys.*, 3:14, March 2017. doi: 10.1007/JHEP03(2017)014.

[73] G. Compère and R. Oliveri. Self-similar accretion in thin discs around near-extremal black holes. *Mon. Not. Roy. Astron. Soc.*, 468:4351–4361, July 2017. doi: 10.1093/mnras/stx748.

[74] S. E. Gralla and P. Zimmerman. Critical Exponents of Extremal Kerr Perturbations. *ArXiv e-prints*, November 2017.

[75] G. Compère, K. Fransen, T. Hertog, and J. Long. Gravitational waves from plunges into Gargantua. *ArXiv e-prints*, December 2017.

[76] C. T. Cunningham and J. M. Bardeen. The Optical Appearance of a Star Orbiting an Extreme Kerr Black Hole. *The Astrophys. J. Letters*, 173:L137, May 1972. doi: 10.1086/180933.

[77] Ari Laor. Line profiles from a disk around a rotating black hole. *Astrophys. J.*, 376:90, 1991. doi: 10.1086/170257.

[78] Kris Beckwith and Chris Done. Iron line profiles in strong gravity. *Mon. Not. Roy. Astron. Soc.*, 352:353, 2004. doi: 10.1111/j.1365-2966.2004.07955.x.

[79] M. Dovciak, Vladimir Karas, and T. Yaqoob. An Extended scheme for fitting x-ray data with accretion disk spectra in the strong gravity regime. *Astrophys. J. Suppl.*, 153:205–221, 2003. doi: 10.1086/421115.

[80] T. Dauser, J. Wilms, C. S. Reynolds, and L. W. Brenneman. Broad emission lines for negatively spinning black holes. *Mon. Not. Roy. Astron. Soc.*, 409:1534, 2010. doi: 10.1111/j.1365-2966.2010.17393.x.

[81] B. C. Bromley, F. Melia, and S. Liu. Polarimetric Imaging of the Massive Black Hole at the Galactic Center. *Astrophys. J.l*, 555:L83–L86, July 2001. doi: 10.1086/322862.

[82] R. V. Shcherbakov, R. F. Penna, and J. C. McKinney. Sagittarius A* Accretion Flow and Black Hole Parameters from General Relativistic Dynamical and Polarized Radiative Modeling. *Astrophys. J.*, 755:133, August 2012. doi: 10.1088/0004-637X/755/2/133.

[83] R. V. Shcherbakov, R. F. Penna, and J. C. McKinney. Constraining the Accretion Flow in Sgr A* by General Relativistic Dynamical and Polarized Radiative Modeling. In C. M. Zhang, T. Belloni, M. Méndez, and S. N. Zhang, editors, *Feeding Compact Objects: Accretion on All Scales*, volume 290 of *IAU Symposium*, pages 309–310, February 2013. doi: 10.1017/S1743921312020157.

[84] A. A. Chael, M. D. Johnson, R. Narayan, S. S. Doeleman, J. F. C. Wardle, and K. L. Bouman. High-resolution Linear Polarimetric Imaging for the Event Horizon Telescope. *Astrophys. J.*, 829:11, September 2016. doi: 10.3847/0004-637X/829/1/11.

[85] R. Gold, J. C. McKinney, M. D. Johnson, and S. S. Doeleman. Probing the Magnetic Field Structure in Sgr A* on Black Hole Horizon Scales with Polarized Radiative Transfer Simulations. *Astrophys. J.*, 837:180, March 2017. doi: 10.3847/1538-4357/aa6193.

[86] K. Akiyama, S. Ikeda, M. Pleau, V. L. Fish, F. Tazaki, K. Kuramochi, A. E. Broderick, J. Dexter, M. Mościbrodzka, M. Gowanlock, M. Honma, and S. S. Doeleman. Superresolution Full-polarimetric Imaging for Radio Interferometry with Sparse Modeling. *Astronomical Journal*, 153:159, April 2017. doi: 10.3847/1538-3881/aa6302.

[87] M. Mościbrodzka. Modeling Polarized Emission from Black Hole Jets: Application to M87 Core Jet. *Galaxies*, 5:54, September 2017. doi: 10.3390/galaxies5030054.

[88] J. Birdi, A. Repetti, and Y. Wiaux. Sparse interferometric Stokes imaging under the polarization constraint (Polarized SARA). *Mon. Not. Roy. Astron. Soc.*, 478:4442–4463, August 2018. doi: 10.1093/mnras/sty1182.

[89] P. Pihajoki, M. Mannerkoski, J. Nättilä, and P. H. Johansson. General Purpose Ray Tracing and Polarized Radiative Transfer in General Relativity. *Astrophys. J.*, 863:8, August 2018. doi: 10.3847/1538-4357/aacea0.

[90] A. Jiménez-Rosales and J. Dexter. The impact of Faraday effects on polarized black hole images of Sagittarius A*. *Mon. Not. Roy. Astron. Soc.*, 478:1875–1883, August 2018. doi: 10.1093/mnras/sty1210.

[91] S. Chandrasekhar. *The mathematical theory of black holes*. Oxford University Press, 1983.

[92] Eva Hackmann. *Geodesic equations in black hole space-times with cosmological constant*. PhD thesis, Bremen U., 2010. URL `http://elib.suub.uni-bremen.de/diss/docs/00011880.pdf`.

[93] G. V. Kraniotis. Precise analytic treatment of Kerr and Kerr-(anti) de Sitter black holes as gravitational lenses. *Class. Quant. Grav.*, 28:085021, 2011. doi: 10.1088/0264-9381/28/8/085021.

[94] Claus L□mmerzahl and Eva Hackmann. Analytical Solutions for Geodesic Equation in Black Hole Spacetimes. *Springer Proc. Phys.*, 170:43–51, 2016. doi: 10.1007/978-3-319-20046-0_5.

[95] K. P. Rauch and R. D. Blandford. Optical caustics in a kerr spacetime and the origin of rapid X-ray variability in active galactic nuclei. *Astrophys. J.*, 421:46–68, January 1994. doi: 10.1086/173625.

[96] C. Fanton, M. Calvani, F. de Felice, and A. Cadez. Detecting Accretion Disks in Active Galactic Nuclei. *Publications of the Astronomical Society of Japan*, 49:159–169, April 1997. doi: 10.1093/pasj/49.2.159.

[97] Jason Dexter and Eric Agol. A Fast New Public Code for Computing Photon Orbits in a Kerr Spacetime. *Astrophys. J.*, 696:1616–1629, 2009. doi: 10.1088/0004-637X/696/2/1616.

[98] J. M. Bardeen. Timelike and null geodesics in the Kerr metric. In *Proceedings, Ecole d'Et□ de Physique Th□orique: Les Astres Occlus: Les Houches, France, August, 1972*, pages 215–240, 1973.

[99] Monica Guica, Thomas Hartman, Wei Song, and Andrew Strominger. The Kerr/CFT Correspondence. *Phys. Rev.*, D80:124008, 2009. doi: 10.1103/PhysRevD.80.124008.

[100] A. M. Al Zahrani, Valeri P. Frolov, and Andrey A. Shoom. Particle Dynamics in Weakly Charged Extreme Kerr Throat. *Int. J. Mod. Phys.*, D20:649–660, 2011. doi: 10.1142/S0218271811018986.

[101] C. T. Cunningham. The effects of redshifts and focusing on the spectrum of an accretion disk around a Kerr black hole. *Astrophys. J.*, 202:788–802, December 1975. doi: 10.1086/154033.

[102] A. C. Fabian, K. Iwasawa, C. S. Reynolds, and A. J. Young. Broad Iron Lines in Active Galactic Nuclei. *Publications of the Astronomical Society of the Pacific*, 112:1145–1161, September 2000. doi: 10.1086/316610.

[103] C. S. Reynolds and M. A. Nowak. Fluorescent iron lines as a probe of astrophysical black hole systems. *Physics Reports*, 377:389–466, April 2003. doi: 10.1016/S0370-1573(02)00584-7.

[104] L. Brenneman. *Measuring the Angular Momentum of Supermassive Black Holes*. 2013. doi: 10.1007/978-1-4614-7771-6.

[105] I. D. Novikov and K. S. Thorne. Astrophysics of black holes. In C. Dewitt and B. S. Dewitt, editors, *Black Holes (Les Astres Occlus)*, pages 343–450. Gordon and Breach Science Publishers, New York, 1973.

[106] D. N. Page and K. S. Thorne. Disk-Accretion onto a Black Hole. Time-Averaged Structure of Accretion Disk. *Astrophys. J.*, 191:499–506, July 1974. doi: 10.1086/152990.

[107] R. F. Penna, A. Sąowski, and J. C. McKinney. Thin-disc theory with a non-zero-torque boundary condition and comparisons with simulations. *Mon. Not. Roy. Astron. Soc.*, 420:684–698, February 2012. doi: 10.1111/j.1365-2966.2011.20084.x.

[108] Y. Tanaka, K. Nandra, A. C. Fabian, H. Inoue, C. Otani, T. Dotani, K. Hayashida, K. Iwasawa, T. Kii, H. Kunieda, F. Makino, and M. Matsuoka. Gravitationally redshifted emission implying an accretion disk and massive black hole in the active galaxy MCG-6-30-15. *Nature*, 375: 659–661, June 1995. doi: 10.1038/375659a0.

[109] K. A. Pounds, J. N. Reeves, A. R. King, and K. L. Page. Exploring the complex X-ray spectrum of NGC 4051. *Mon. Not. Roy. Astron. Soc.*, 350:10–20, May 2004. doi: 10.1111/j.1365-2966.2004.07639.x.

[110] G. Risaliti, F. A. Harrison, K. K. Madsen, D. J. Walton, S. E. Boggs, F. E. Christensen, W. W. Craig, B. W. Grefenstette, C. J. Hailey, E. Nardini, D. Stern, and W. W. Zhang. A rapidly spinning supermassive black hole at the centre of NGC 1365. *Nature*, 494:449–451, February 2013. doi: 10.1038/nature11938.

[111] A. C. Fabian. The innermost extremes of black hole accretion. *Astron. Nachr.*, 337:375, May 2016. doi: 10.1002/asna.201612316.

[112] N. Andersson and K. Glampedakis. Superradiance Resonance Cavity Outside Rapidly Rotating Black Holes. *Phys. Rev. Lett.*, 84:4537–4540, May 2000. doi: 10.1103/PhysRevLett.84.4537.

[113] K. Glampedakis and N. Andersson. Late-time dynamics of rapidly rotating black holes. *Phys. Rev. D*, 64(10):104021, November 2001. doi: 10.1103/PhysRevD.64.104021.

[114] H. Yang, A. Zimmerman, A. Zenginoğlu, F. Zhang, E. Berti, and Y. Chen. Quasinormal modes of nearly extremal Kerr spacetimes: Spectrum bifurcation and power-law ringdown. *Phys. Rev. D*, 88(4):044047, August 2013. doi: 10.1103/PhysRevD.88.044047.

[115] L.-X. Li, R. Narayan, and J. E. McClintock. Inferring the Inclination of a Black Hole Accretion Disk from Observations of its Polarized Continuum Radiation. *Astrophys. J.*, 691:847–865, January 2009. doi: 10.1088/0004-637X/691/1/847.

[116] M. Bañados, J. Silk, and S. M. West. Kerr Black Holes as Particle Accelerators to Arbitrarily High Energy. *Phys. Rev. Lett.*, 103(11):111102, September 2009. doi: 10.1103/PhysRevLett.103.111102.